

WJ

THE SCHWERTFEGER LIBRARY
1225 W. Dayton Street
Madison, WI 53706

Report 77-1

January 1977

**NUMERICAL SIMULATION OF THE CONDITIONS
WITHIN A SETTLING CLOUD CHAMBER**

By: Klaus M. Weickmann

Prepared for:
National Science Foundation

Grant No. AEN-03258

C. E. Anderson, Principal Investigator

Department of Meteorology
University of Wisconsin
Madison, Wisconsin 53706

Report 77-1

January 1977

NUMERICAL SIMULATION OF THE CONDITIONS
WITHIN A SETTLING CLOUD CHAMBER

By: Klaus M. Weickmann

Prepared for:

National Science Foundation

Grant No. AEN-03258

C. E. Anderson, Principal Investigator

Department of Meteorology
University of Wisconsin
Madison, Wisconsin 53706

Dr. Richard Barchet
Co-principal Investigator
December 1976

Preface

This report is based on a thesis submitted in partial fulfillment of the requirements for a master of science degree in meteorology by Klaus M. Weickmann.

A very serious defect in studies of cloud microphysics is the lack of a technique to measure the concentration of ice nuclei that is representative of the cloud environment. Much of the difficulty in making such measurements stems from incomplete information on the conditions under which ice nuclei are activated within the various devices currently used to measure ice nuclei. Mr. Weickmann's report concerns the settling cloud chamber. A similar device received high marks at recent ice nucleus counter intercomparison workshops. The results of a numerical model of this chamber represent a significant step toward understanding the environmental conditions under which ice nucleation take place in the chamber. However, only diffusion, drop condensation and evaporation, and sedimentation processes are presently incorporated into the model. The results are, however, so encouraging that we intend to include the ice phase and ice nucleation mechanisms as the next level of model sophistication.

Wm. Richard Barchet
Co-principal Investigator
December 1976

ACKNOWLEDGEMENTS

Many thanks are due Professor W. Richard Barchet for always making time to discuss any aspect of this work and for his numerous pragmatic and valuable suggestions. I greatly enjoyed the opportunity to work with him. I would also like to thank Professor Charles E. Anderson for his comments on the thesis and Dr. Kenneth C. Young for graciously making his numerical model available to me.

Dr. Richard Barchet
Co-Principal Investigator
December 1976

TABLE OF CONTENTS

	Page
Abstract	v
List of Symbols	vii
I. Introduction	1
A. Literature Survey	2
B. Settling Cloud Chamber Description	7
II. Cloud Chamber Model	11
A. Numerical Model	12
1. Model Description	12
2. Nucleus Distribution	13
3. Hydrometeor Treatment	15
B. Model Processes and Equations	18
1. Nucleus Transformation or Haze Par- ticle Activation	18
a. Full version	18
b. Parameterized version	19
2. Hydrometeor Growth	21
3. Continuity Equations for Vapor, Heat, and Liquid Water	27
III. Numerical Procedure	33
A. Time Step and Finite Difference Approx- imations	34
B. Solution of Continuity Equations for Water Vapor and Heat	34
1. Iterative Scheme	34
2. Nucleation Adjustment	38
3. Full Model versus Parameterized Version	39
C. Heat and Vapor Sink	41

	Page
D. Continuous Bin Technique	43
E. Stability Considerations for Condensa- tional Growth	52
IV. Results and Discussion	54
A. Effect of Condensation Nucleus Distribu- tion	56
B. Effect of Radial Fluxes	62
C. Effect of Condensation Coefficient	73
D. Effect of Bin Resolution	82
E. Effect of Parameterized Nucleation	85
F. Summary of Model Results	90
V. Implications for Use of SCC as Ice Nucleus Counter	99
VI. Suggestions for Future Work	107
Bibliography	110

ABSTRACT

The influence of chamber relative humidity and liquid water content on ice nucleation prompted a time-dependent, one-dimensional numerical simulation of the conditions within a settling cloud chamber. In such a chamber vapor is made available for droplet and crystal growth by evaporation and diffusion from a warm, moist top plate to the chamber. The lower two-thirds of the chamber is kept essentially isothermal and provides a nearly steady-state environment for ice nucleation and crystal growth.

The model incorporates diffusion of water vapor and heat, sorption of water by hygroscopic nuclei, growth of haze particles at subcritical saturation, activation of haze into growing drops, condensational growth of the drops, sedimentation of drops and haze particles through the depth of the chamber, and evaporation of drops and haze in the drier portion of the chamber. Saturation ratio, liquid water content, droplet concentration, droplet size spectra and temperature and vapor density profile evolution are outputs from the model. Inputs consist of initial temperature and moisture distributions as well as a nucleus size distribution. Boundary conditions are specified by actual measurements on such a chamber.

The results indicate that, with an input of nuclei having critical supersaturations of $>1\%$, high supersaturations should be expected in the upper 8 cm of the SCC. Conditions in the lower portion of the chamber rapidly become more uniform with time and remain so while droplets are being nucleated in the upper layers. The implications of these results for ice nucleus measurements with the SCC are discussed.

LIST OF SYMBOLS

c_d	droplet specific heat	L	latent heat of vaporization
c_p	specific heat of air at constant pressure	LWC	liquid water content
CCN	cloud condensation nuclei	m	molality
CN	condensation nuclei	m_d	droplet mass
D	mass diffusivity	m_s	solute mass
DC	droplet concentration	m_w	mass of water
f	accommodation coefficient	M	total hydrometeor mass in a bin
$f\langle\log r\rangle$	number density function - $dN/d\log r$	M_s	molecular weight of solute
$f\langle r\rangle$	number density function - $\frac{dN}{dr}$	M_w	molecular weight of water
$f\langle m\rangle$	number density function - $\frac{dN}{dm}$	n_r	number density within a bin
F	mass flux of vapor	n_{r_0}	number density at r_0
FM	full version of the model	n_t	total molar density
IN	ice nuclei	N	total hydrometeor number in a bin
k	thermal diffusivity	NH	total hydrometeor gravitational potential
k_r	slope of distribution in a bin	PV	parameterized version of the model
K	thermal diffusivity	Q	heat flux

		<u>Greek Symbols</u>
r	hydrometeor radius	
r_{ACT}	activation radius	α condensation coefficient
r_o	droplet bin midpoint	
r_s	solute radius	α' thermal diffusion factor
R	gas constant	Δ_T temperature jump distance
R_v	gas constant for water vapor	λ mean free path of water vapor molecules in air
S, SR	environmental saturation ratio	
S_d	hydrometeor equilibrium saturation ratio	$v\phi$ van'T Hoff factor
S^*	critical saturation ratio	ρ' hydrometeor solution density
S_e^*	bin endpoint S^*	ρ_a density of air
S_{MAX}	level of maximum SR	ρ_d equilibrium vapor density
SCC	settling cloud chamber	ρ_s solute density
S_{ACT}	activation saturation ratio	$\rho_s(T)$ saturation vapor density at T
T	environmental temperature	ρ_v environmental vapor density
T_d	hydrometeor temperature	ρ_w equilibrium vapor density at chamber wall
TGDC	thermal gradient diffusion chamber	
TM	mass transferred between bins	σ' hydrometeor solution surface tension
TN	number transferred between bins	
TNH	NH transferred between bins	
x	mole fraction of water	

I. Introduction

One of the most important variables to be considered when studying the initial evolution of droplet and ice crystal distributions within natural clouds is the spatial and temporal variation of supersaturation. The maximum supersaturation reached within a cloud to a large extent determines the number of condensation nuclei that are activated into growing drops. The influence of supersaturation on ice nucleation has been recently addressed by several authors, e.g., Gagin (1974) and Huffman (1973), and may be of great importance in determining the ice crystal concentration within a cloud.

The measurement of atmospheric aerosols important for the nucleation of drops and ice crystals within clouds is generally carried out in the laboratory utilizing various types of cloud chambers. Understanding these measurements and applying the results to infer droplet and ice crystal distributions within natural clouds requires detailed knowledge of cloud chamber conditions, as well as ambient atmospheric conditions.

A. Literature Survey

The main effort in past studies to determine conditions within cloud chambers has focused on the thermal gradient diffusion chamber (TGDC) which is used to measure the cloud condensation nucleus (CCN) spectra of sampled cloud air as a function of supersaturation. Since direct measurement of supersaturation is not feasible with an accuracy required for use in cloud physics, conditions within these chambers have generally been determined numerically. Supersaturation within the chamber is produced by diffusion of heat and water vapor between two moist surfaces at slightly different temperatures.

Wieland (1956), ignoring second order effects which result in slightly non-linear gradients of temperature (T) and vapor density (ρ_v), determined the steady state distribution of supersaturation within the TGDC and using a series of cells with different top temperatures obtained nucleus activity spectra.

Twoomey (1959) suggested use of a chemical gradient diffusion chamber to minimize transient supersaturations caused by temperature differences between contained air and the walls, and used an optical technique to count nucleated drops. He assumed linear vapor pressure and temperature gradients for his supersaturation determination, but emphasized the limitations of ignoring the vapor sink and

heat source of growing droplets. Twoomey (1963) and Elliot (1971) discussed the effect on the supersaturation of the radial diffusion of heat from the walls with the latter suggesting an aspect ratio (diameter/height) of ≈ 6 or 7 in order to mitigate wall effects. Saxena et al (1970) and Fitzgerald (1970) analyzed the problem of transient supersaturations associated with introducing an air sample at a temperature less than the top plate temperature and obtained analytical solutions to the time dependent heat and moisture diffusion equations. The former also present an extensive historical summary of the TGDC and its various applications in studying homogeneous and heterogeneous nucleation. Fitzgerald (1972) researched the effect of ignoring mass diffusion due to a temperature gradient (see Katz and Mirabel, 1975) and the temperature dependence of the mass and heat diffusivities in calculating the steady state supersaturation profile. The most complete theoretical analysis of steady-state supersaturation profiles in TGDC was done by Katz and Mirabel (1975). They concluded that the assumption of linear temperature and vapor pressure gradients for calculating the maximum supersaturation give results accurate to within 1% of the more complete solution. Their more rigorous solution takes into account: 1) the mass flux due to a temperature gradient (Soret effect), 2) the heat flux carried by the flux of vapor molecules, and 3) the

heat flux due to a concentration gradient (Dufour effect). Squires (1972) experimentally confirmed an earlier computation by Twoomey (the details of which are not published) which suggested that the vapor sink does not become important until a droplet concentration of $1000/\text{cm}^3$ at a supersaturation of 1% is reached. Squires' paper also gives an excellent summary of the various factors that influence the actual maximum supersaturation achieved in the TGDC and those that limit its operation at very low supersaturations (see also Fitzgerald, 1972).

Recently Alofs and Carstens (1976) performed a numerical study of a TGDC by calculating the condensational growth and subsequent sedimentation of an initial prescribed nucleus distribution at various discrete levels within the chamber. Transient supersaturation profiles used in the study were based on the analytic solutions of Saxena et al (1970) and Fitzgerald (1970) to the diffusion equations. Vapor depletion and latent heat release were not considered. Results showing instrument droplet count versus actual count were presented for various supersaturations, nucleus distributions and drop size detector limits. Potentially large errors in counting CCN were found, although the authors suggest that basic conclusions drawn from these measurements in the past will not be seriously affected.

Despite the limitations of TGDC, in general good correspondence between measured CCN spectra and the droplet distributions within sampled clouds have been reported (Fitzgerald, 1972; Squires and Twoomey, 1961 and others). Ruskin and Kocmond (1971) also report excellent agreement between CCN measurements made by different types of TGDC.

Much less success has been achieved in attempts to make the more difficult ice nucleus (IN) measurements. A wide variety of instruments have been used to measure ice nucleus concentrations yet actual conditions relevant for the activation of ice nuclei within these instruments, e.g., supersaturation, liquid water content and droplet spectrum and concentration, are usually only described qualitatively; how these differ from device to device is not known. Conclusions from two recent ice nucleus workshops (Bigg, 1971; Vali, 1975; Juisto and Lavoie, 1975) suggest that the discrepancies between different devices may, in particular, be a result of differences in supersaturation achieved - yet few quantitative estimates of the supersaturation within the instruments are available.

Lala and Juisto (1972) developed a 1-D, time dependent numerical model to study the humidity fields within a TGDC used for measuring ice nucleus concentrations on membrane filters. The humidity distribution was determined by the combined effects of vapor diffusion to the filter surface

and activation and growth of condensation nuclei (CN) and IN on the filter surface (vapor sink). The results suggested that water saturation is generally not reached above the filter surface and that the maximum humidities reached decrease with an increasing number of particles on the filter. Huffman and Vali (1973) emphasized the three dimensionality of the vapor field above the filter surface and derived an average "area of effect" for a vapor sink on the surface (CN or IN). They then obtained a correction factor for the IN measurement based on (1) their "area of effect" model, (2) the number of ice crystals observed on the filter, and (3) an independent measurement of the hygroscopic particles on the filter.

Beyond the extensive work done with TGDC used for CCN measurements and the studies of vapor depletion above membrane filter surfaces, little else has been done to determine the time and space development of supersaturation within cloud chambers, especially those used for ice nucleus measurements. This thesis addresses the problem of the variation of humidities and particle distributions within a settling cloud chamber (SCC) through application of a 1-D, time dependent numerical model. The SCC is one of a variety of instruments being used to measure ice nucleus concentrations. First developed by Ohtake and Isaha (1961), the SCC has been tested extensively during several international workshops convened to evaluate ice

nucleus measurements. One advantage often cited for the SCC is the close simulation of natural cloud conditions provided in the lower portions of the chamber (Bigg, 1971). For a discussion of other advantages and disadvantages as well as recent suggestions for improved operation see Ohtake (1976, 1971).

B. Settling Cloud Chamber

In principle, the SCC is a combination of a thermal gradient diffusion chamber in which cloud droplets are formed and a subfreezing, isothermal chamber in which ice nucleation by nearly all mechanisms can occur. The bottom two-thirds of the chamber is kept isothermal by a circulating coolant. A strong stable gradient of temperature and moisture is produced above the isothermal layer by a heated, moist top. Prior to the formation of the cloud, the chamber is relatively dry; however, after the heated moist top is in place downward diffusion of vapor and heat rapidly supersaturates the upper portion of the chamber. Condensation nuclei in this region sorb water, become haze drops, grow beyond their critical size, and continue growth as cloud droplets. The drops settle at their terminal velocity into the lower cold portion of the chamber. Evaporation of these droplets brings the humidity quickly to saturation in this region of the SCC. Eventually the cloud penetrates to the chamber floor and a nearly

steady-state, approximately water saturated, growth environment exists in the isothermal portion of the chamber.

The specific SCC to be modelled in this thesis was constructed at the University of Wisconsin for use in an ice nucleus inhibition study (Barchet, 1976). In this study the effect of exposing AgI aerosol to small concentrations of various amine gases was investigated. Alternately treated and untreated AgI particles were injected into the SCC approximately 5 minutes after cloud initiation. Any differences in subsequent ice crystal counts within a sugar tray at chamber bottom were recorded. In order to minimize the possibility of spurious ice crystal formation the air giving rise to the chamber cloud was filtered such that particles of sizes $> 0.3 \mu\text{m}$ were mostly excluded. As a consequence the numerical results presented concentrate on the chamber conditions for initial CN distributions with critical supersaturations of $> 1\%$. Under normal operating conditions i.e., when used strictly as an ice nucleus counter, no filtration of the air occurs and the entire ambient nuclei distribution gives rise to the chamber cloud.

Figure 1 shows the vertical temperature gradient actually measured in the Wisconsin SCC before and after cloud formation. The temperature distribution with the cloud is representative of a quasi steady-state attained

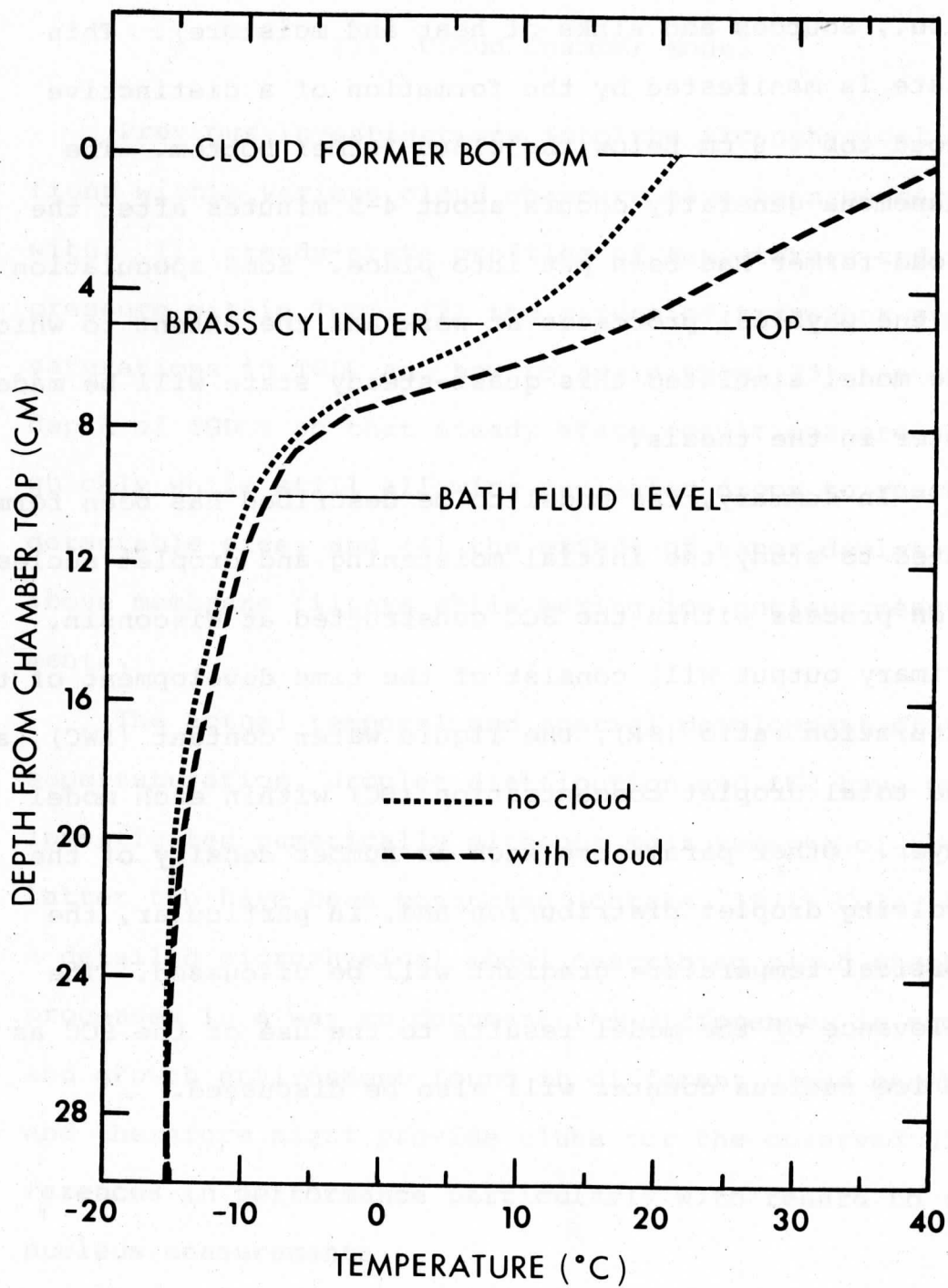


Figure 1. The measured temperature distributions within the SCC prior to and after cloud formation.

in the chamber between the vertical and radial diffusion of heat and moisture, and the initial nucleus distribution (i.e., sources and sinks of heat and moisture). This state is manifested by the formation of a distinctive cloud top 6-8 cm below the cloud former bottom. The phenomena generally occurs about 4-5 minutes after the cloud former has been put into place. Some speculation as to the physical processes at work and the extent to which the model simulated this quasi-steady state will be made later in the thesis.

In summary, the model to be described has been formulated to study the initial moistening and droplet nucleation process within the SCC constructed at Wisconsin. Primary output will consist of the time development of the saturation ratio (SR), the liquid water content (LWC), and the total droplet concentration (DC) within each model layer. Other parameters such as number density of the evolving droplet distribution and, in particular, the vertical temperature gradient will be discussed. The relevance of the model results to the use of the SCC as an ice nucleus counter will also be discussed.

II. Cloud Chamber Model

Previous investigations into the microphysical conditions within various cloud chambers have been concerned with: (1) steady-state profiles of temperature and vapor pressure within TGDC, (2) the extent of transient supersaturations in TGDC and how to avoid them, (3) the optimum depth of TGDCs so that steady state conditions are reached quickly while still allowing nucleated drops to reach a detectable size, and (4) the effect of vapor depletion above membrane filters while making ice nucleus measurements.

The actual temporal and spatial development of the supersaturation, droplet distribution and LWC have not been investigated numerically although measurements of the latter two have been conducted (Ohtake, 1971; Cole, 1970). A detailed microphysical model describing cloud chamber processes is a way to document the differences in nucleation and growth environment found in different cloud chambers; and therefore might provide clues for the observed differences in performance particularly with regard to ice nucleus measurements.

Since the cloud chambers being studied (SCC and TGDC) are stably stratified, to a first approximation motion of the air can be neglected. The main emphasis can thus be placed on formulating the microphysics as accurately as possible, although in the present model some simplifications are still made in treating droplet development from a dry nucleus distribution.

A. Numerical Model

1. Model Description. The physical processes occurring in the SCC are simulated with a 1-D, time dependent numerical model with detailed microphysics of the condensation process; ice nucleation is not modelled. Vertical diffusion of heat and moisture are treated explicitly in the model while radial diffusion forced by colder and drier walls is parameterized. The initial (precloud) temperature distribution is based on actual measurement in the SCC, while the initial vapor density distribution is assumed to be vertically uniform. Top and bottom boundary conditions for T and ρ_v are 42°C and 56.6 gm m^{-3} , respectively at chamber top and -15.5°C and 1.3 gm m^{-3} at chamber bottom, 30 cm below the top. The boundary conditions at the walls will be given in conjunction with the discussion of the parameterized radial fluxes.

2. Nucleus Distribution. The CN available to the chamber are assumed to be pure spherical NaCl particles distributed in a spectrum as shown in Figure 2. For the basic model runs the distribution is discretized into 45 bins which vary logarithmically from 1.67×10^{-20} gm (0.001 μ m) to 2.4×10^{-10} gm (3.0 μ m) corresponding to critical saturation ratios (S^*) from 1.30 to 1.00001. The number density function (following notation used by Berry, 1967) for the Aitken nuclei ($r_s < 0.03 \mu$ m) is given by

$$f\langle \log r_s \rangle = 3.0 \times 10^8 r_s^{0.7}$$

$$f\langle m_s \rangle = 4.13 \times 10^7 m_s^{-0.767}$$

for particle radius (r_s) in centimeters and particle mass (m_s) in grams, while nuclei with $r_s \geq .03 \mu$ m are assumed to follow a Junge distribution

$$f\langle \log r_s \rangle = 5.57 \times 10^{-12} r_s^{-2.85}$$

$$f\langle m_s \rangle = 6.55 \times 10^{-12} m_s^{-1.95}$$

Initial nuclei number (N) and mass (M) within a bin are obtained by integration over the appropriate bin limits:

$$N = \int f\langle m_s \rangle dm, \quad M = \int m_s f\langle m_s \rangle dm.$$

DRY NaCl NUCLEUS SIZE DIST

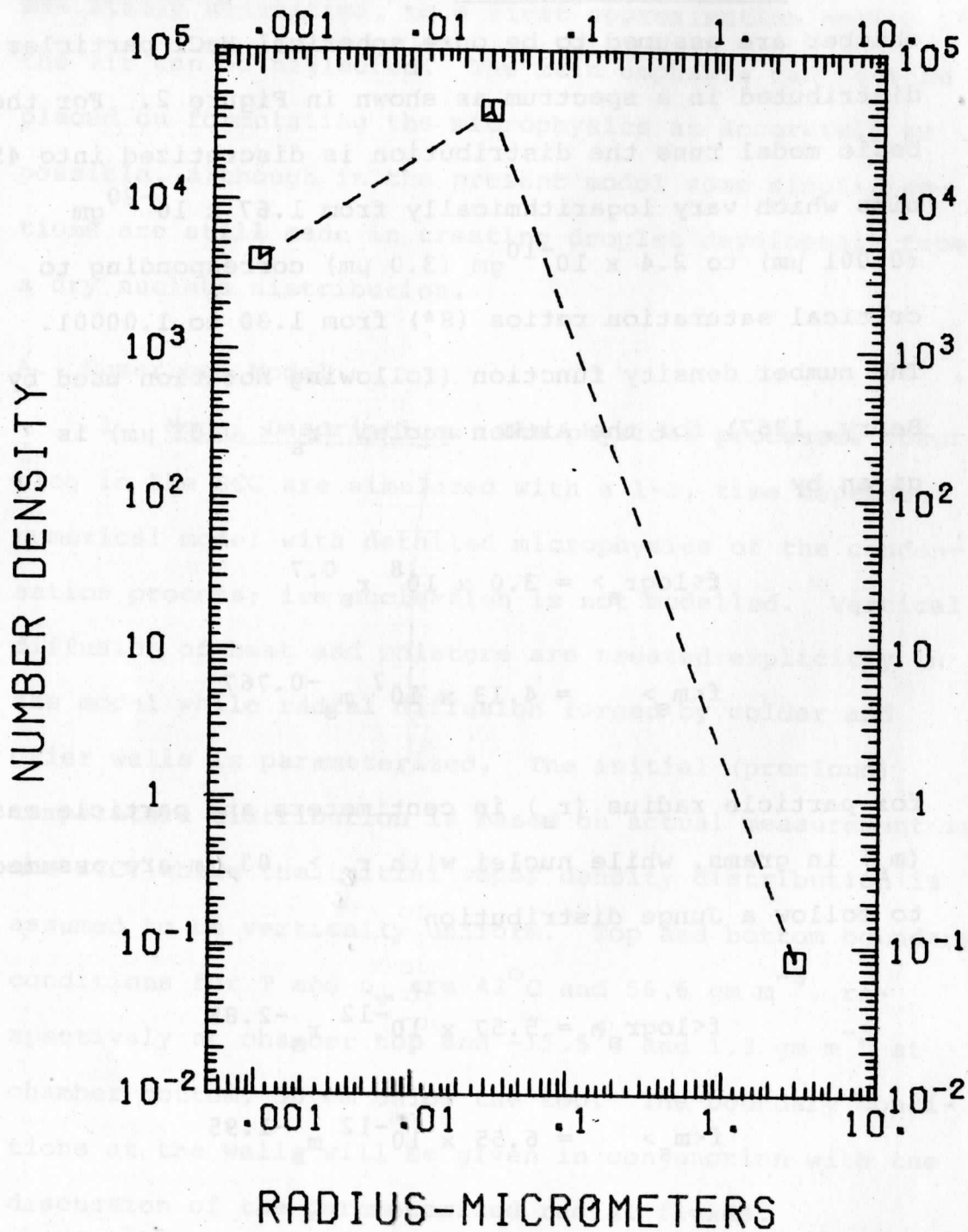


Figure 2. The dry NaCl nucleus distribution used as input to the cloud chamber numerical model.

3. Hydrometeor Treatment. Droplets and haze particles are the hydrometeors resolved in the model. The change of their respective distributions by condensational growth is treated differently for the two hydrometeor classes. Howell (1949), Mordy (1959), and Nieburger and Chien (1960) performed a Lagrangian calculation of condensation on an initially discretized CN distribution. In this approach, the hydrometeors are allowed to exist at the actual radius calculated after each time step; the number in a given initial CN interval remains constant. Figure 3, from Mordy (1959), illustrates the result of a strictly Lagrangian based condensation calculation.

In the model, haze growth is Lagrangian since the dissolved solute mass (i.e., the center mass in the initial nucleus bin) remains fixed, whereas the haze particle itself can take on any radius value. For each haze bin a mean mass radius, based on the amount of solute mass, water mass and the initial number of nuclei, is computed after each time step. This variable radius is then used to determine mass growth and sedimentation for hydrometeors which occupy the bin.

Alternatively the basis for the condensation calculation can be Eulerian, in which case the distribution size intervals are fixed for all time. This often becomes a necessity as more physical processes, such as nucleation, sedimentation, and collision-coalescence, are considered.

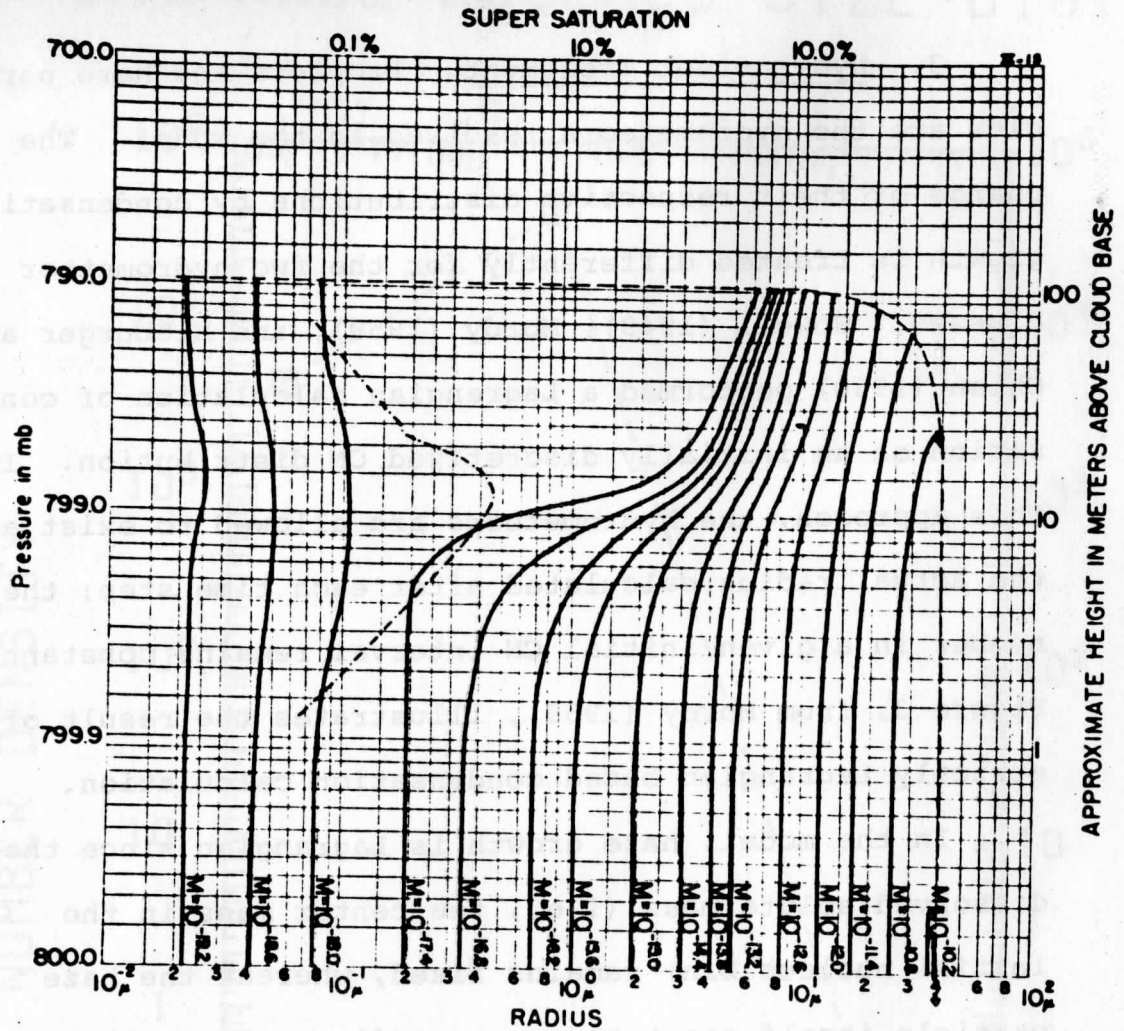


Figure 3. The results of a strictly Lagrangian condensation calculation in which an initial nucleus distribution is discretized into 16 solute mass intervals. The evolution of supersaturation within the rising air parcel is shown by the dashed line. (from Mordy, 1959)

The problem now becomes one of transforming the results of an inherently Lagrangian condensation calculation to an Eulerian form after each time step. Various schemes including interpolation (Arnason and Greenfield, 1972 and Kovetz and Olund, 1969), moment conservation (Eagan and Mahoney, 1972), and finite differentiation (Clark, 1973), have been used to achieve this transformation. Berry and Rheinhardt (1973) performed a detailed study to determine the most accurate conversion scheme and concluded that the moment conserving scheme of Eagan and Mahoney, modified so that droplets can move in either direction within the distribution, gave the best results. In the model a scheme proposed by Young (1974) which has some similarities to the moment conserving one is used. Droplet growth, therefore, is treated in an Eulerian framework with 45 logarithmically spaced radius bins ranging from .004 μm to 18 μm .

The vertical transfer of hydrometeors by sedimentation is an important part of the model. The vertical resolution is 1 cm and hydrometeors can fall into any of the lower model layers. Haze particles which evaporate in drier layers are returned to the proper CN bin, however the salt mass within drops that evaporate is lost since drops are assumed to be dilute. Stokes' law is used for computing terminal velocities.

B. Model Processes and Equations

1. Nuclei Transformation or Haze Particle Activation

a. Full model version. The initial CN are assumed to be uniformly distributed throughout the chamber. Nuclei begin their transformation into saturated solution droplets (haze) when the ambient relative humidity (RH) in a layer exceeds 74%. All water vapor in excess of 74% is uniformly distributed over the entire nucleus distribution. Except for very small nuclei when the water mass added to a nuclei bin surpasses 2.78 times the total solute mass in the bin the nuclei become activated i.e., sufficient water has been "taken up" to transform the dry nuclei into saturated solution droplets. The 74% figure for transition from dry NaCl, nuclei to haze is obtained from measurements made by Winkler and Junge (1972) with bulk NaCl, i.e., without consideration of the effect of surface tension. The actual relative humidity at which transformation occurs is a function of nucleus mass. For the very small nuclei the radius corresponding to a saturated solution droplet, $r_{ACT} = (3.78 \times m_s / (4.18879 \times \rho'))^{1/3}$, is associated with an equilibrium saturation ratio considerably greater than 0.74. Thus the small nuclei are transformed into growing haze particles when this 'activation' saturation ratio is exceeded. The activation values were obtained from Köhler's Equation such that

$$S_{\text{ACT}} = 0.74 * \exp \left[\frac{2\sigma'}{K_v T \rho' v_{\text{ACT}}} \right]. \text{ Curve A in Figure 4}$$

shows S_{ACT} as a function of nucleus mass for a portion of the nucleus spectrum. The departure from the 74% transition value is not significant for the larger nuclei, however it increases rapidly as nuclei become smaller than 10^{-15} gm. For convenience, Curve B in Figure 4 also shows the variation of S^* as a function of nucleus mass with the first seven data points defining the bin limits used for nuclei with $m_s < 1.0 \times 10^{-7}$ gm. In obtaining S^* and the critical radius needed for calculating curve C, the dilute version of Köhler's Equation was used with a temperature of 290°K . More will be said about this figure later. Activated nuclei exist as stable haze particles until the supersaturation in the layer exceeds the critical supersaturation associated with the bin. If condensational growth causes the mean mass radius of the haze particles within the bin to exceed the critical radius, the haze particles are transferred to the proper droplet bin.

b. Parameterized version. The above treatment of nucleation in the full version of the model (henceforth called the FM or full model) uses a disproportionate amount of CPU time in comparison to other processes. A less rigorous treatment in which the haze particle phase is by-passed is called the parameterized version (PV) of

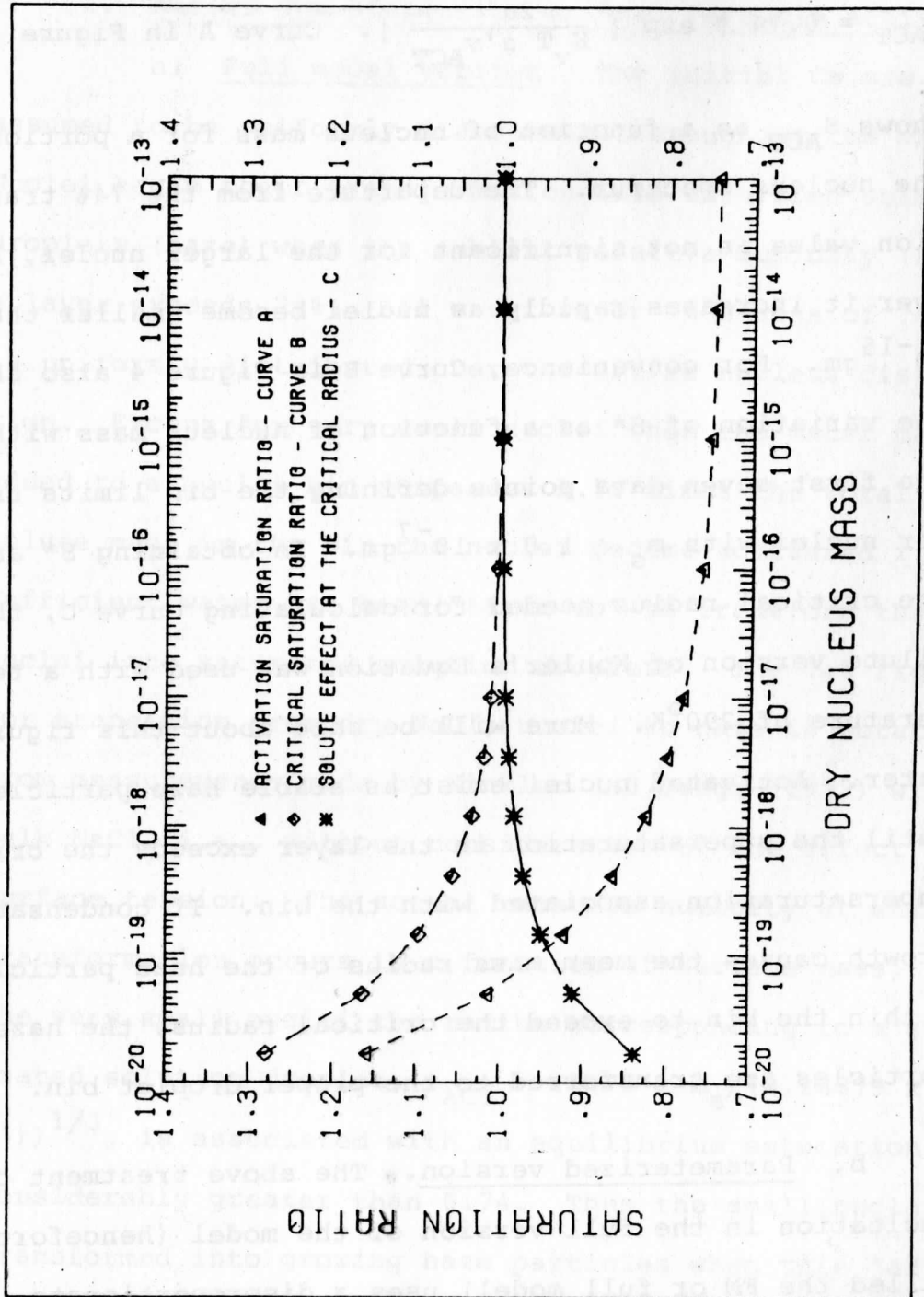


Figure 4. The critical saturation ratio (S^*), activation saturation ratio (SACT), and solute effect at the critical radius for a portion of the nucleus distribution used in the model.

the model. Dry CN are transferred to the appropriate cloud drop bin when the $SR > S^*$. These nucleated drops are assumed to be at their critical radius if the nuclei have a mass $< 3.0 \times 10^{-15}$ gm. A lag in reaching the critical size is assumed for nuclei with a larger mass. The basis for determining the lag is obtained from a FM run and is the mean mass radius of the individual haze bins at the time their S^* was exceeded in layer 1. This basic value is then adjusted for each layer by the amount of time the layer is between relative humidities of 74% and the bin S^* . If the nucleated drop has a radius of $> 7 \mu\text{m}$ it is assumed to have fallen out of the layer and evaporated in the next lower layer. The total amount of nucleated water mass in a layer (number activated x mass of activated drop) is incorporated into the vapor density and temperature continuity equations to simulate moisture uptake by the bypassed haze particles.

2. "Hydrometeor Growth". The procedure for determining hydrometeor growth is similar to that used by Young (1974) in his numerical treatment of orographic precipitation and by Fitzgerald (1972) in his study comparing computed and observed droplet distributions. With a steady-state, spherically symmetric vapor field, the flux of vapor to a drop via diffusion is given by Maxwell's equation

$$\frac{dm}{dt} = 4 \pi r D (\rho_v - \rho_d) \quad (1)$$

where D is the mass diffusivity, r is the drop radius, ρ_v is the environmental vapor density and ρ_d is the equilibrium vapor density over the drop. In a similar manner the flux of sensible heat away from the drop is given by

$$\frac{dh}{dt} = 4 \pi r k (T - T_d) \quad (2)$$

where k is the thermal conductivity, T is the environmental temperature and T_d is the temperature of the drop. Combining (1) and (2), the energy balance at the surface of a growing drop is given by

$$m_d c_d \frac{dT_d}{dt} = L \frac{dm}{dt} + \frac{dh}{dt} \quad (3)$$

with m_d the droplet mass, c_d the droplet specific heat capacity and L the latent heat of vaporization. Equation (3) states that the heat stored within the drop equals the imbalance between the latent heat gained by condensation and the sensible heat lost by diffusion. Generally the heat storage is insignificant except for very large drops and is therefore ignored. This assumption implies that the

drop always instantaneously adjusts to its wet bulb temperature during growth and evaporation.

As seen from (1), in order to determine the amount of droplet growth, the vapor density at the droplet surface; which is a function of droplet temperature, radius, surface tension and amount of dissolved solute, must be known. Several different approaches, as described by Koenig (1970), can now be taken to calculate droplet growth, with the more rigorous also being the more time consuming. The approach taken here is to calculate the droplet surface temperature explicitly. Integrating the Clausius-Clapeyron equation from T to T_d yields

$$\frac{\rho_s(T_d)}{\rho_s(T)} = e^{-\frac{L}{R_v T^2} (T - T_d)} \quad (4)$$

where R_v is the gas constant for water vapor, $\rho_s(T_d$ or $T)$ is the saturation vapor density at these temperatures, and TT_d has been approximated by T^2 . Expanding the exponential in a series and discarding all terms beyond the quadratic reduces (4) to

$$\frac{\rho_s(T_d)}{\rho_s(T)} \sim 1 - \frac{L}{R_v T^2} (T - T_d) + \frac{\left[\frac{L}{R_v T^2} (T - T_d) \right]^2}{2} \quad (5)$$

The equilibrium vapor density over the drop and that in the environment may be written as

$$\rho_d = S_d \rho_s (T_d) \quad (6a)$$

$$\rho_v = S \rho_s (T) \quad (6b)$$

where S is the saturation ratio in the environment. The equilibrium saturation ratio over the drop, S_d , as modified by the curvature and solute effects is defined as

$$S_d = \exp \left[\frac{2\sigma'}{r\rho'T_dR_V} - \frac{\nu\phi M_w m_s}{M_s m_w} \right] \quad (7)$$

where σ' and ρ' are the solution droplet surface tension and density, $\nu\phi$ is the van 'T Hoff factor, M_w and m_w are the molecular weight and mass of water and M_s and m_s are the molecular weight and mass of the dissolved salt, respectively. The first term in the exponential gives the modification of S_d due to the curvature effect while the second includes the solute effect.

Substituting (6) and (5) into (3), dropping the storage term and rearranging gives a quadratic equation in the unknown $(T-T_d)$ which is then solved to give the droplet temperature

$$\frac{T-T_d}{B^2} = \left(B + \frac{A}{S_d} \right) - \left(\left(B + \frac{A}{S_d} \right)^2 - 2 \frac{(S_d - S)}{S_d} B^2 \right)^{1/2} \quad (8)$$

where $B = R_v L / T^2$ and $A = k / DL \rho_s (T)$. Droplet growth is then calculated from (1) after the equilibrium droplet vapor density has been determined from (6a). The saturation vapor densities in the model are calculated using formulas taken from Barchet (1972).

This procedure is used for both water droplets and haze particles. However, nucleated drops are considered to be dilute and therefore the effect of the dissolved NaCl is not considered. Curve C in Figure 4 shows the magnitude of the solute effect when the droplet has reached its critical radius. As is evident from the figure, the assumption of dilute water droplets is very good for droplets formed on nuclei with mass $> 10^{-17}$ gm. In both the FM and PV, droplet growth for the first time step after the critical radius has been reached (or assigned as is the case with the PV) includes the solute effect. As a result, the strong solute effect is diminished considerably thereafter and the dilute droplet approximation also becomes valid for the smaller drops. For the haze particles the molality given by

$$m = \frac{1000}{M_s} \left[\frac{r^3 \rho'}{r_s^3 \rho_s} - 1 \right]^{-1} = \frac{m_s}{.05845 * m_w} \quad (9)$$

is calculated at each time step to determine the contribution to the haze saturation ratio from the solute effect and to obtain ρ' , σ' and $v\phi$.

An additional correction involved a modified diffusion coefficient for heat and mass to account for the purely kinetic control of growth as the droplet radius approaches a size close to λ , the mean free path of water vapor molecules in air. The correction used was derived by Fuchs (1959) who assumed Maxwell's equation to be valid only at distances greater than $\Delta \approx \lambda$ from the surface of the drop. In the small layer adjacent to the drop interchange of vapor molecules was assumed to occur without diffusive interaction with air resulting in a kinetic mass growth equation. Fuchs essentially equated the two transport equations at their common boundary $r = \Delta$ and then extended the Maxwell solution to the surface of the drop. He obtained a correction factor which is generally incorporated into the diffusion coefficient, i.e.,

$$D' = \left[\frac{1}{\frac{r}{r+\Delta} + \frac{D}{r\alpha} \left(\frac{2\pi R_V}{T} \right)^{1/2}} \right] D \quad (10)$$

where D' is the modified mass diffusivity and α is the condensation coefficient.

Fitzgerald (1972) recently reviewed Fuchs' derivation and also applied it to the heat conduction equation to

obtain a modified thermal conductivity given by

$$k' = k \left[\frac{1}{\frac{r}{r+\Delta_T} + \frac{k}{r\rho_a f c_p} \left(\frac{2\pi}{R T_d}\right)^{1/2}} \right] \quad (11)$$

where Δ_T is the "temperature jump distance" ($\sim \lambda$), f is the thermal accommodation coefficient, k' is the modified thermal conductivity, and R is the specific gas constant of dry air. In the model $\alpha = 0.03$ and $f = 1$ are used following the suggestions of Sinnarwalla et al (1975) who measured these quantities.

3. Continuity equations for vapor, heat and liquid water. The complete heat and mass flux equations for a two component system in which only one component (i.e., water vapor) is diffusing have been thoroughly investigated by Katz and Mirabel (1975). Using notation consistent with the remainder of this thesis, these equations are

$$F = - \frac{n_t D}{1-x} \left[\frac{dx}{dz} + \alpha x (1-x) \frac{d}{dz} \ln T \right] \quad (12)$$

$$Q = -k \frac{dT}{dz} + F \int c_p dT + \alpha' F (1-x) RT \quad (13)$$

where F is the mass flux of water, x is its mole fraction, n_t the total molar density ($n_t = P_t/RT$), P_t the total

pressure and α' the thermal diffusion factor. In (12) the first term represents the mass flux due to a concentration gradient and the second term is the mass flux due to a temperature gradient. In (13) the first term is the heat flux due to a temperature gradient, the second term the heat flux carried by the flux of molecules and the third term the heat flux due to a gradient in concentration.

Katz and Mirabel used these equations to determine the errors made by: (1) neglecting certain specific terms and, (2) merely assuming linear vapor pressure or linear vapor density gradients when calculating the supersaturation profiles in TGDC. Figure 5, taken from their paper shows "the relative difference (in percent) of the maximum supersaturation in the cloud chamber obtained under the various conditions described below (i.e., in the figure) and the maximum supersaturation obtained by assuming linear temperature and partial pressure profiles for a cloud chamber with a top (warm) surface of 20°C as a function of the temperature difference ΔT between the two surfaces." The largest difference apparent in the figure is that between the use of linear vapor density and linear vapor pressure gradients and even here the percent relative error is only approximately 12%.

For the purposes of this study, all terms other than the flux of mass and heat due to vapor density and temperature gradients respectively are neglected. The use of

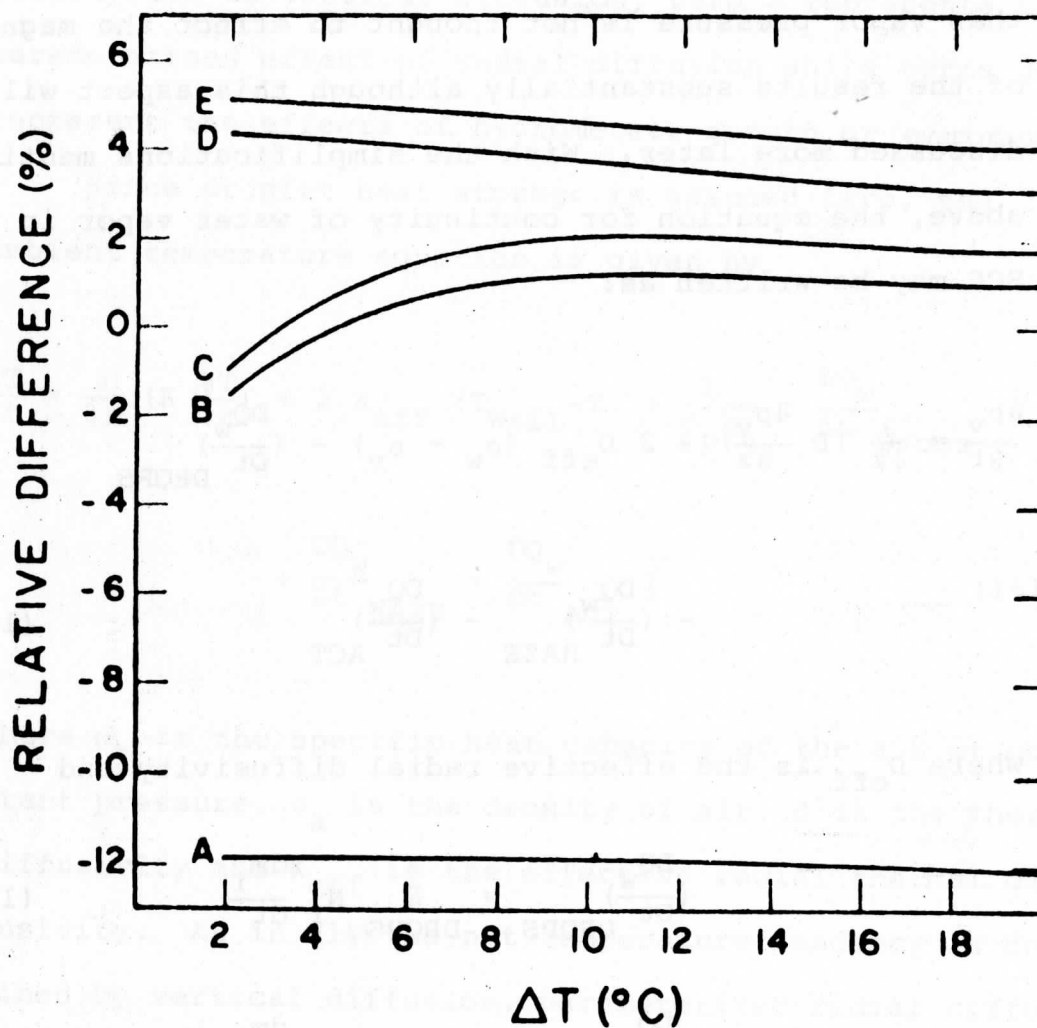


Figure 5. Plot of the percent relative difference between the maximum supersaturation calculated assuming linear temperature and vapor pressure gradients and:

- A, linear temperature and vapor density gradients
- B, exact solution of Eqs. (12 and 13) with $\alpha' = 0$ and $c_p = 8.0$
- C, exact^p solution of Eqs. (12 and 13) with $\alpha' = 0.15$ and $c_p = 8.0$
- D, exact^p solution of Eqs. (12 and 13) with α' and $c_p = 0$
- E, exact^p solution of Eqs. (12 and 13) with $\alpha' = 0.15$ and $c_p = 0$

as a function of the temperature difference between the two plates, using 20°C as the temperature of the top plate. (from Katz & Mirabel, 1975)

vapor density in the continuity equation for vapor rather than vapor pressure is not thought to effect the magnitude of the results substantially although this aspect will be discussed more later. With the simplifications mentioned above, the equation for continuity of water vapor in the SCC may be written as:

$$\begin{aligned} \frac{\partial \rho_v}{\partial t} = \frac{\partial}{\partial z} \left(D \frac{\partial \rho_v}{\partial z} \right) + 2 D_{\text{eff}} (\rho_w - \rho_v) - \left(\frac{DQ_w}{Dt} \right)_{\text{DROPS}} \\ - \left(\frac{DQ_w}{Dt} \right)_{\text{HAZE}} - \left(\frac{DQ_w}{Dt} \right)_{\text{ACT}} \end{aligned} \quad (14)$$

where D_{eff} is the effective radial diffusivity and

$$\left(\frac{DQ_w}{Dt} \right)_{\text{DROPS}} = \sum_{\text{DROPS}} N_i \frac{dm_i}{dt} \quad (15a)$$

$$\left(\frac{DQ_w}{Dt} \right)_{\text{HAZE}} = \sum_{\text{HAZE}} N_j \frac{dm_j}{dt} \quad (15b)$$

with N_i and N_j the number of hydrometeors present in the i^{th} drop and j^{th} haze bin. $(DQ_w/Dt)_{\text{ACT}}$ is the water mass used to activate dry nuclei to haze particles. In the PV the terms for HAZE and ACT are combined into a single term for the nucleation of new drops. Term 1 on the r.h.s. of (14) gives the contribution to the local change of vapor

density due to vertical diffusion, term 2 represents the parameterized effect of radial diffusion while terms 3-5 represent the effects of hydrometeor growth or evaporation.

Since droplet heat storage is assumed zero, the ambient temperature equation is given by

$$\frac{\partial T}{\partial t} = \frac{\partial}{\partial z} \left(K \frac{\partial T}{\partial z} \right) + 2 K_{\text{eff}} (T_{\text{WALL}} - T) + \frac{L}{c_p \rho_a} \left[\frac{DQ_w}{Dt} \text{ Drops} + \frac{DQ_w}{Dt} \text{ HAZE} + \frac{DQ_w}{Dt} \text{ ACT} \right] \quad (16)$$

where c_p is the specific heat capacity of the air at constant pressure, ρ_a is the density of air, K is the thermal diffusivity and K_{eff} is the effective radial thermal diffusivity. As in (14) the net temperature tendency is determined by vertical diffusion, parameterized radial diffusion and the heat gain or loss associated with hydrometeor growth or evaporation. The details of the radial heat and vapor sink parameterization will be discussed later.

Finally the local variation of drop number density can be expressed as

$$\frac{\partial f\langle r \rangle}{\partial t} = - \frac{\partial}{\partial z} (v_T f\langle r \rangle) - \frac{\partial}{\partial r} \left(\frac{dr}{dt} f\langle r \rangle \right) + \left(\frac{\delta f\langle r \rangle}{\delta t} \right)_{\text{NUC}} \quad (17)$$

where v_T is the terminal velocity and $f\langle r \rangle$ is the number density function ($\text{cm}^{-3} \Delta r^{-1}$) such that $N_i = \int_{r_1}^{r_2} f\langle r \rangle dr$.

The terms on the r.h.s. represent the change in number density function due to sedimentation, condensation and nucleation, respectively. As discussed previously the Lagrangian condensation calculation for haze particles allows only sedimentation or nucleation to change N_j , i.e., (17) is solved completely only for water droplets. This approach was used in order to preserve the dissolved salt mass in each haze droplet. If the Eulerian approach is used for the haze particles, (17) would have to be solved completely, which would involve determination (through an additional continuity equation) of the new salt mass associated with the haze particles in the bin (Berry and Rheinhardt, 1973). This is especially true at relative humidities $< 100\%$ where the molality of the solution droplet is high. On the other hand above the critical supersaturation the dilute droplet approximation used for water droplets is reasonable.

III. Numerical Procedure

The system of equations described in the previous section is essentially a subset of the more extensive set that describes the micro- and macro-physics of the warm rain process. Although no completely rigorous solution to these equations has been attempted, various authors have chosen to investigate special subsets of these equations. The degree of complexity of these attempts has ranged from those describing initial droplet development in closed air parcels (Howell, 1949; Mordy, 1959; Nieburger and Chien, 1960), to 1-D Eulerian, numerical simulations of warm rain with very detailed microphysics (Takahashi, 1976), to 2-D simulations with some parameterization of the microphysics (Arnason and Greenfield, 1972; Ogura and Takahashi, 1973; Clark, 1973). The solution to these different models has been approached in slightly different ways by their respective authors. In the present model, techniques developed by Young (1974) are used to solve (3), (4) and (6). Young's continuous bin approach is used to solve (6) because the results are considered to be more accurate than interpolation schemes or finite difference approaches used by other authors. Additionally Dr. Young

made his model available to the author and with some modification it was adaptable to the present investigation.

A flow chart showing the sequence of operations during a single time step is shown in Figure 6. Some specific points regarding the numerical techniques are discussed in the remainder of this chapter.

A. Time Step and Finite Difference Approximations

The time derivatives in (1), (3) and (4) are approximated by a simple forward in time finite difference scheme while the spatial derivatives in (3) and (4) are approximated by centered differences. The stability criteria for the diffusional component is $\Delta t < (\Delta z)^2 / 2D$. Using $z = 1$ cm this restricts the time step to $\Delta t < 1.8$ sec. For most model runs a $\Delta t = 1$ sec was used, although each run starts with ten 1/4 sec time steps in order to obtain enough points for proper extrapolation (i.e., first guesses) of ρ_v and T (see Iterative Scheme subsection).

B. Solution of Continuity Equation for Water Vapor and Heat

1. Iterative Scheme. Whenever sources or sinks are not present in a layer, new values of ρ_v and T are given by the diffusional contribution only, which is determined by finite difference approximation in the case of vertical

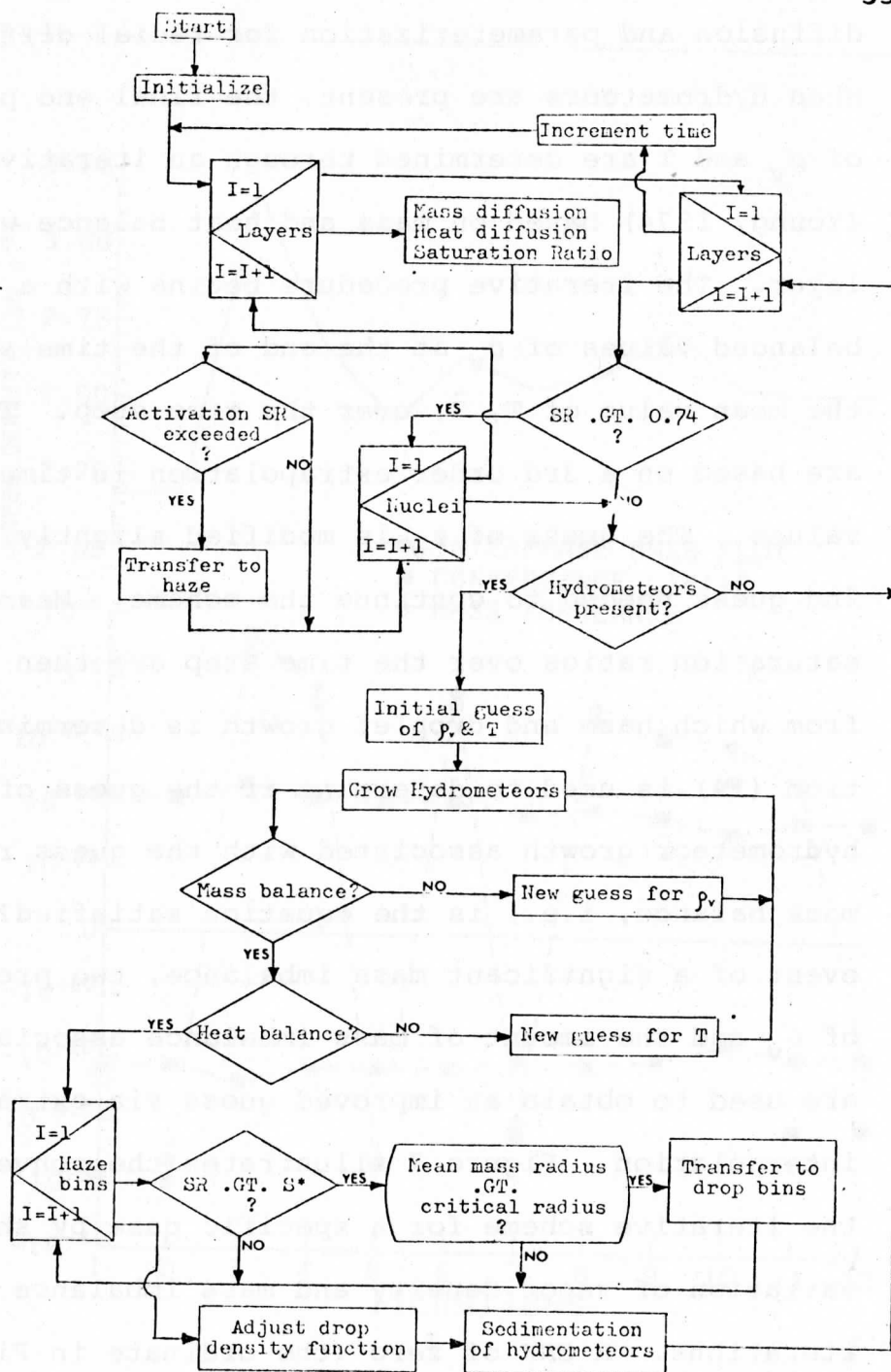


Figure 6. A flow chart of the numerical model illustrating sequence of operations during a single time step and relevant action taken to obtain a solution.

diffusion and parameterization for radial diffusion. When hydrometeors are present, the final end point values of ρ_v and T are determined through an iterative scheme (Young, 1974) based on mass and heat balance within a layer. The iterative procedure begins with a guess of the balanced values of ρ_v at the end of the time step and of the mean value of T , \bar{T} , over the time step. The guesses are based on a 3rd order extrapolation in time of previous values. The guess of ρ_v is modified slightly to give a 2nd guess needed to continue the scheme. Mean ambient saturation ratios over the time step are then obtained from which haze and droplet growth is determined. Equation (14) is used to determine if the guess of ρ_v and the hydrometeor growth associated with the guess results in mass balance, i.e., is the equation satisfied? In the event of a significant mass imbalance, two previous guesses of ρ_v and the amount of mass imbalance associated with each are used to obtain an improved guess via extrapolation or interpolation. Figure 7 illustrates the convergence of the iterative scheme for a specific case by showing the variation of vapor density and mass imbalance (CHK) versus iterations. A CHK of zero (the ordinate in Figure 7) indicates mass balance between the diffusional component and sources and sinks within the layer. In the model, iteration continues until mass balance falls within an imbalance tolerance threshold that is given by 10^{-4} times the total

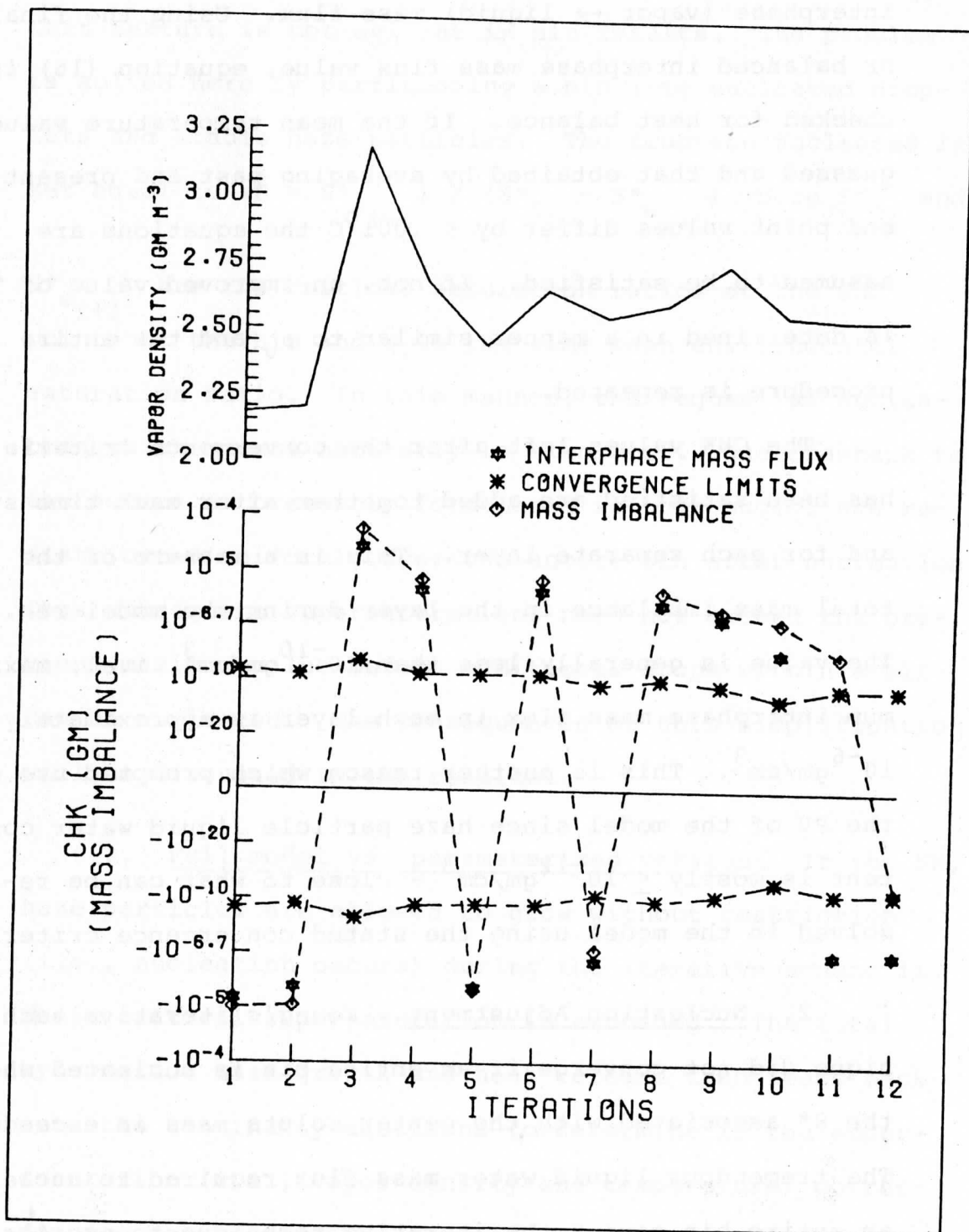


Figure 7. Specific example of iterative scheme converging to obtain mass balance between water vapor and liquid water within a layer during one time step. Top graph gives initial guesses of ρ_v and subsequent values obtained from the iterative scheme. Bottom graph illustrates mass imbalance convergence limits and total interphase mass flux associated with each ρ_v value.

interphase (vapor ↔ liquid) mass flux. Using the final or balanced interphase mass flux value, equation (16) is checked for heat balance. If the mean temperature value guessed and that obtained by averaging past and present end point values differ by $< .001^{\circ}\text{C}$ the equations are assumed to be satisfied. If not, an improved value of \bar{T} is determined in a manner similar to ρ_v and the entire procedure is repeated.

The CHK values left after the convergence criteria has been satisfied are added together after each time step and for each separate layer. This is a measure of the total mass imbalance in the layer during the model run. The value is generally less than 10^{-10} gm/cm^3 , i.e., maximum interphase mass flux in each layer is approximately 10^{-6} gm/cm^3 . This is another reason which prompted use of the PV of the model since haze particle liquid water content is mostly $\leq 10^{-12} \text{ gm/cm}^3$ - close to what can be resolved in the model using the stated convergence criteria.

2. Nucleation Adjustment. Young's iterative technique did not converge if an entire bin is nucleated when the S^* associated with the center solute mass is exceeded. The tremendous liquid water mass flux required to nucleate an entire bin causes the iterative technique to oscillate around the S^* of the bin and therefore never to attain mass balance. With Young's parameterization of nucleation

this feature is not evident in his results. The problem is solved here by partitioning a bin into nucleated droplets and stable haze particles. The fraction nucleated is set equal to $(\bar{S} - S^*_{e_{i+1}}) / (S^*_{e_i} - S^*_{e_{i+1}})$ where $S^*_{e_i}$ and $S^*_{e_{i+1}}$ are the critical saturation ratios at the end points of the bin and \bar{S} is the time mean environmental saturation ratio. In this manner, the sequential nucleation which occurs naturally is simulated. One drawback to the scheme as presently formulated is that nuclei are redistributed uniformly over the entire bin after nucleation. Thus subsequent supersaturations need not exceed the previous maximum value before additional drops within a bin can be nucleated. The consequences of this simplification will be discussed in the results.

3. Full model vs. parameterized version. In the FM, haze particles are allowed to grow without restriction (i.e., nucleation occurs) during the iterative scheme if their critical supersaturation is exceeded. The total hydrometeor mass growth and heat release then feeds back into the continuity equations to determine if the supersaturation (i.e., vapor density and temperature) corresponding to the present iteration satisfies the equations. If not, the values are adjusted and a different haze particle class may be the boundary between stable and unstable growth. In this way the scheme converges on the

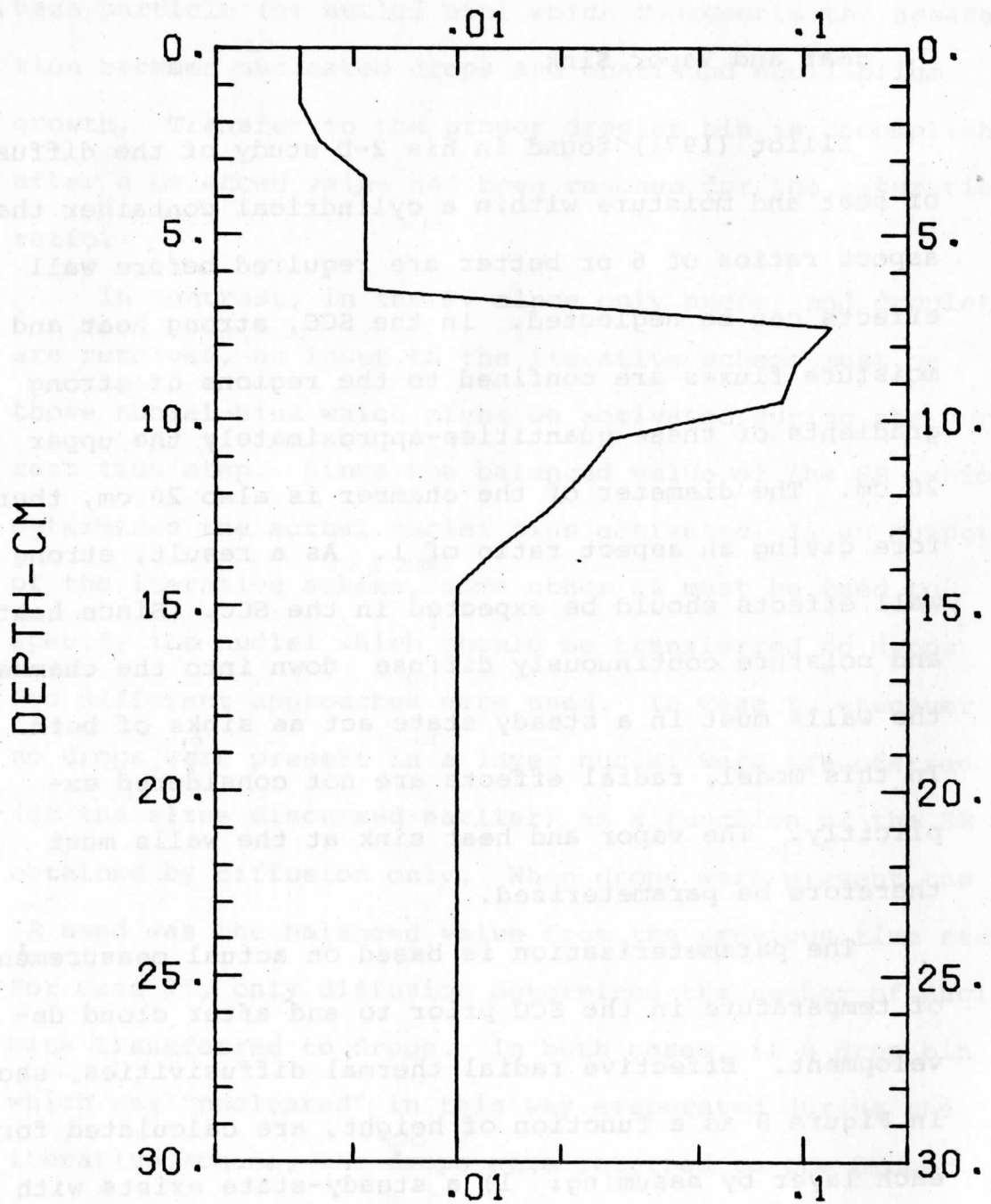
haze particle (or nuclei bin) which represents the separation between nucleated drops and continued equilibrium growth. Transfer to the proper droplet bin is accomplished after a balanced value has been reached for the saturation ratio.

In contrast, in the PV since only nuclei and droplets are resolved, an input to the iterative scheme must be those nuclei bins which might be activated during the current time step. Since the balanced value of the SR (which determines the actual nuclei bins activated) is an output of the iterative scheme, some other SR must be used to specify the nuclei which should be transferred to drops. Two different approaches were used. In Case I, whenever no drops were present in a layer nuclei were transferred (at the sizes discussed earlier) as a function of the SR obtained by diffusion only. When drops were present the SR used was the balanced value from the previous time step. For Case II, only diffusion determined the number of nuclei bins transferred to drops. In both cases, if a drop bin which was "nucleated" in this way evaporated during the iterative scheme, the drops were returned to the proper nucleus bin.

C. Heat and Vapor Sink

Elliot (1971) found in his 2-D study of the diffusion of heat and moisture within a cylindrical container that aspect ratios of 6 or better are required before wall effects can be neglected. In the SCC, strong heat and moisture fluxes are confined to the regions of strong gradients of these quantities—approximately the upper 20 cm. The diameter of the chamber is also 20 cm, therefore giving an aspect ratio of 1. As a result, strong wall effects should be expected in the SCC. Since heat and moisture continuously diffuse down into the chamber, the walls must in a steady state act as sinks of both. In this model, radial effects are not considered explicitly. The vapor and heat sink at the walls must therefore be parameterized.

The parameterization is based on actual measurements of temperature in the SCC prior to and after cloud development. Effective radial thermal diffusivities, shown in Figure 8 as a function of height, are calculated for each layer by assuming: 1) a steady-state exists with no sources or sinks of heat, i.e., vertical flux divergence of heat equals radial flux divergence, 2) vertical flux divergence in a layer is given by the measured post-cloud temperature distribution and, 3) the wall temperatures are given by the measured pre-cloud temperature distribution.



EFFECTIVE RADIAL DIFFUSIVITIES

Figure 8. The effective radial thermal diffusivities used in the parameterization of radial diffusion.

The details of the actual vapor sink at the walls is highly complex due to the uncertainty of the time variation of the equilibrium vapor density, ρ_w , over the glycerine coated walls. In the model ρ_w was assumed to be a certain fraction of the saturation vapor density associated with the wall temperature. The effective mass diffusivities in the various layers were simply set equal to 1.2 x the thermal diffusivities. The effect of the parameterization on the model output temperatures will be discussed in the section on results.

D. Continuous Bin Technique

The changes in number density due to sedimentation and condensation (water droplets only) are found using Young's continuous bin method. As noted in the section on Model Processes, the method has some similarities with the moment conserving scheme introduced by Eagan and Mahoney (1972), and modified for cloud physics use by Berry and Rheinhardt (1973). The moment conserving scheme basically involves reconstructing the normalized 1st and 2nd moments of the droplet distribution within each discrete interval of radius after each time step. The new moments are evaluated through use of a "portioning parameter" which is determined from: 1) the amount of droplet growth, 2) the center of mass of the distribution (1st moment), and 3) the horizontal width of the distribu-

tion (2nd moment). The value of the "portioning parameter" determines the contribution to the new moments within an interval from droplets remaining in that interval and from those growing or evaporating into the interval. In all cases, the droplet distribution is assumed to have a rectangular shape within each bin, i.e., the number of drops is constant for those portions of the bin which are occupied. In this way, the number, mean mass radius and a measure of the horizontal width of the droplet distribution within each bin or interval are found following condensational growth. As noted by Eagan and Mahoney "reconstruction with the 1st and 2nd moments conserves the variance of the entire concentration distribution as it is advected".

Young's continuous bin method is based on: 1) the explicit conservation of droplet number (N) and mass (M) within a particular bin, and 2) the assumption of a number density function within the bin which is linear in radius, i.e., $n_r = n_{r_0} + k_r (r - r_0)$ where n_{r_0} is the number density at the bin midpoint (r_0) and k_r is the slope of the distribution in the bin.

Using the fact that $N = \int n_r dr$, $M = \int n_r m dr$ and substituting the assumed linear number density function into these expressions results in two equations which are solved simultaneously to give expressions for the two unknown variables, n_{r_0} and k_r . These can then be determined

for a particular bin by conserving or keeping track of the total number and mass within the bin. The basic difference between the two Lagrangian to Eulerian conversion methods is: 1) Eagan and Mahoney (1972) assume a rectangular distribution versus the linear distribution assumed by Young, and 2) the 2nd moment is explicitly conserved by Eagan and Mahoney (1972) while Young conserves only number and mass. However, as shown below the linear assumption by Young allows implicit inclusion of a sort of 2nd moment with one end point of the distribution always coinciding with an original bin limit.

The sequence of operations then performed to "advect" drops up or down the distribution is as follows:

1. n_{r_0} and k_r are determined from the droplet number and mass within the bin. When the mean mass radius (i.e., $(M/(N\rho' \times 4.18879))^{1/3}$) associated with the actual values of N and M lies significantly to the left or right of the bin center radius, the number density function calculated from $n_r = n_{r_0} + k_r (r - r_0)$ may give negative values within the bin limits. This implies that droplets may not be distributed over the entire bin but rather are concentrated within certain radius limits within the bin. Young (1974) states that: "In such cases, the bin is iteratively redefined until the largest interval (within the original limits of the bin) not containing negative values is found". This procedure, shown schematically in

Figure 9 gives a measure of the horizontal extent of the droplet distribution and thus can be considered somewhat similar to conservation of the 2nd moment by Eagan and Mahoney.

2. Once the proper bin limits have been determined, the total mass addition to the bin due to condensational growth is distributed equally among all hydrometeors in the bin (reasonable assumption as long as the bin interval is small; in effect are disregarding a portion of the condensation term in (17) given by $\frac{\partial}{\partial r} \left(\frac{dr}{dt} \right) f\langle r \rangle$). As a result, some droplets may exceed bin limits and be transferred while others may remain in the bin. Figure 10 illustrates this transfer for a specific case where drops in bin 34 grow into bins 35 and 36. Prior to transfer bin 34 contains $63.3 \text{ drops cm}^{-3}$ (N_{34}) having a total mass (M_{34}) of $2.14 \times 10^{-9} \text{ gm}$. In the example chosen droplet growth by condensation over a single time step results in a total mass addition (ΔM_{34}) to the bin of $3.33 \times 10^{-9} \text{ gm}$. The arrows (or Δr) in the figure signify the growth of drops at the limits of bin 34 when $1/63.3 \times \Delta M_{34}$ is added to their current mass. The number and mass transferred to

bin 35 are given by $TN_{35} = \int_{r_1}^{r_3 - \Delta r} n_r dr$ and

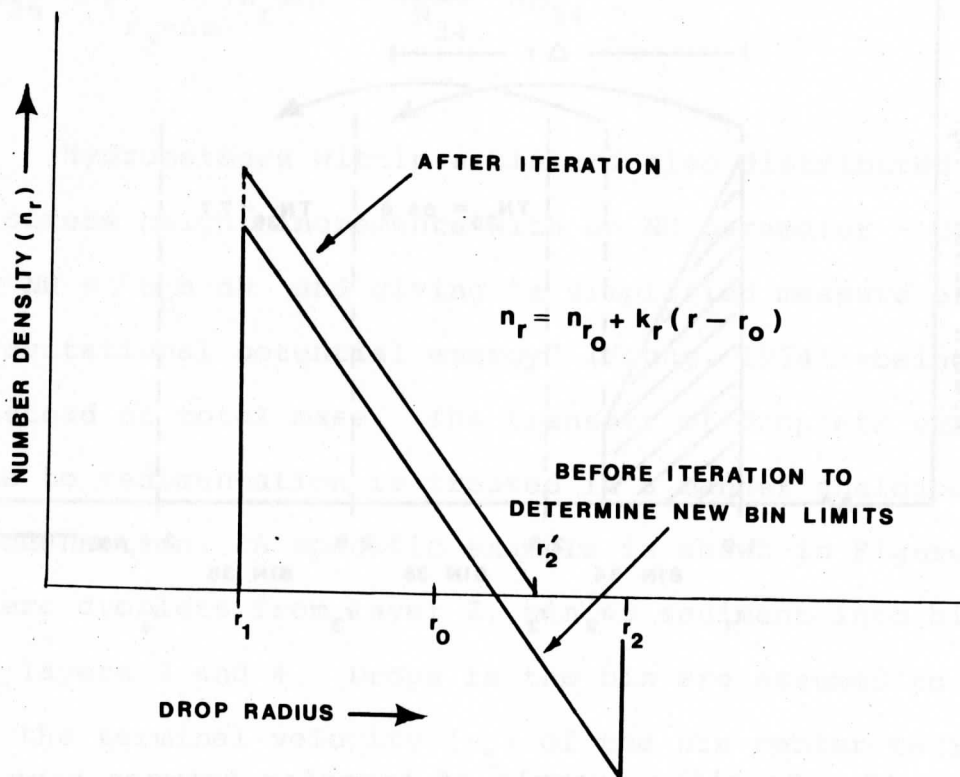


Figure 9. Schematic illustration showing the results of the iterative scheme which is used to determine new bin limits in the event $n_r < 0$ somewhere in the bin.

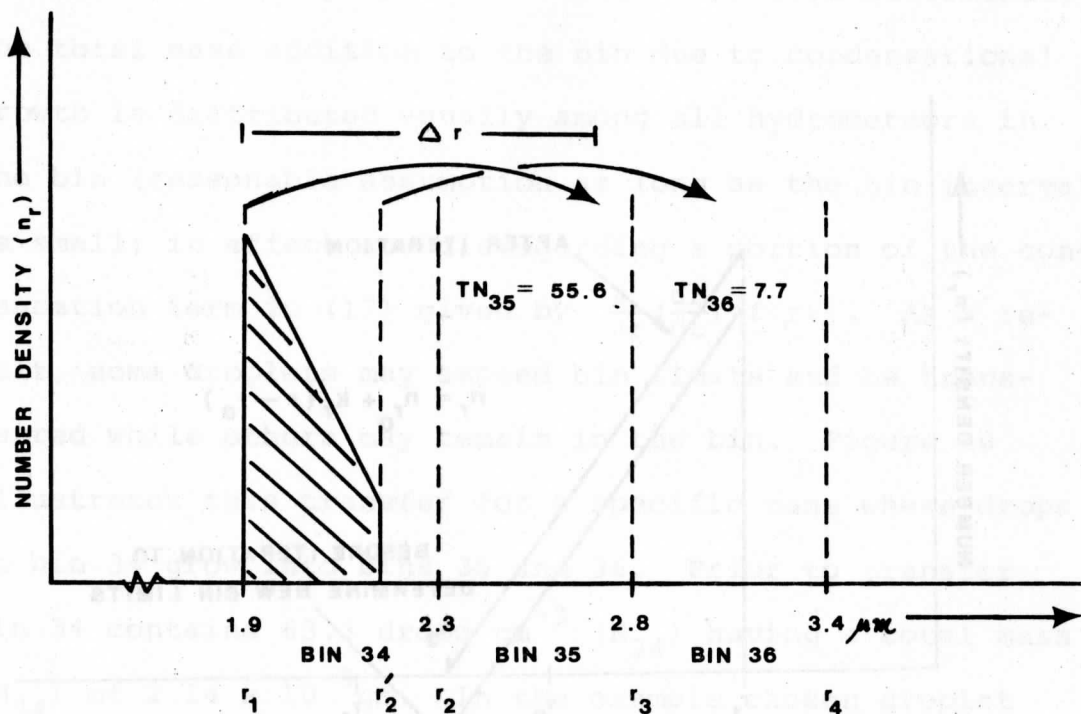


Figure 10. Specific example of transfer between bins due to condensational growth. Drops in BIN 34 grow into BINs 35 and 36. Number and mass transfer is accomplished by integration over the appropriate bin limits. See text.

$$TM_{35} = \int_{r_1}^{r_3 - \Delta r} n_r m dr + \frac{TH_{35}}{N_{34}} \Delta M_{34} \quad \text{while the transfer to}$$

$$\text{bin 36 is given by } TN_{36} = \int_{r_3 - \Delta r}^{r'_2} n_r dr \quad \text{and}$$

$$TM_{36} = \int_{r_3 - \Delta r}^{r'_2} n_r m dr + \frac{TN_{36}}{N_{34}} \Delta M_{34} .$$

Hydrometeors within a bin are also distributed over discrete height increments with an NH parameter - defined by $NH = \int n_h h dh$ and giving "a simplified measure of the gravitational potential energy" (Young, 1974)--being used instead of total mass. The transfer of droplets vertically due to sedimentation is treated in a manner analogous to condensation. A specific example is shown in Figure 11 where droplets from layer 2, bin 43 sediment into bin 43 of layers 3 and 4. Drops in the bin are assumed to fall at the terminal velocity (v_t) of the bin center radius while in the case of haze particles the terminal velocity is given by the mean mass radius. The distance of fall is given by $v_T \Delta t$. Originally layer 2, bin 43 contains 5 drops cm^{-3} (N_2) distributed over h as shown in the Figure and having an NH_2 of 140 cm^{-2} . The number and NH transferred to layer 3, bin 43 are given by

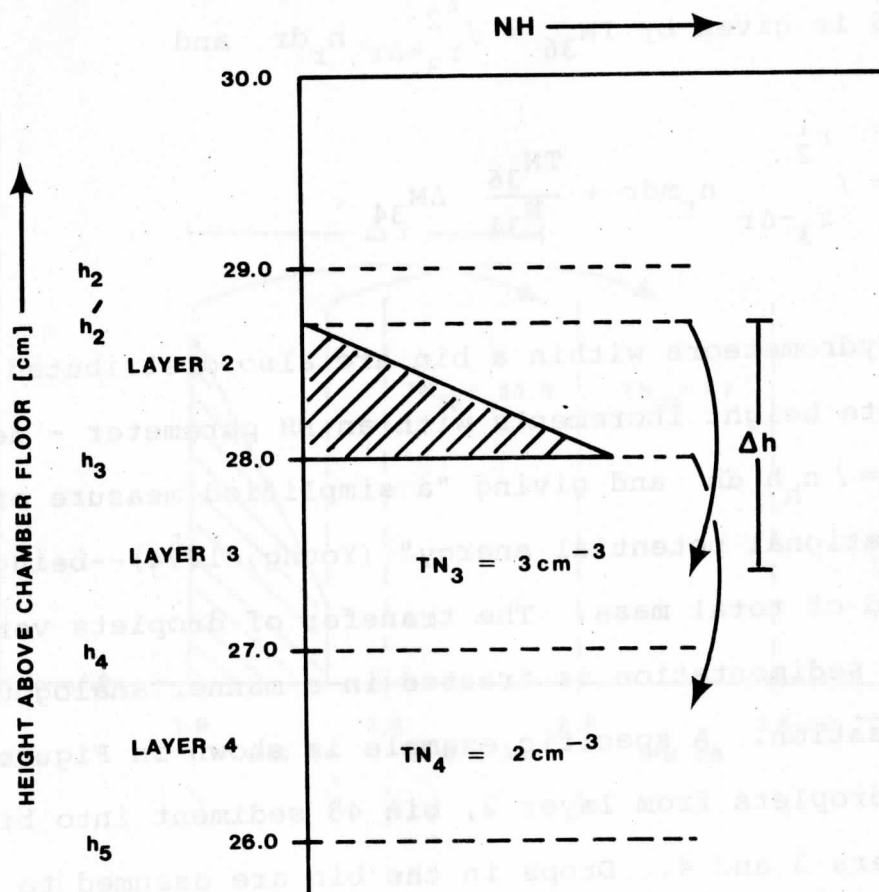


Figure 11. A specific example of the transfer between layers due to sedimentation. Drops in layer 2, bin 43 fall into bin 43 of layers 3 and 4. See text.

$$TN_3 = \int_{h_2'}^{h_4+\Delta h} n_h dh \quad \text{and} \quad TNH_3 = \int_{h_2'}^{h_4+\Delta h} n_h h dh - v_T \Delta t TN_3$$

while the transfer to bin 43, layer 4 from layer 2 is given

$$\text{by } TN_4 = \int_{h_4+\Delta h}^{h_3} n_h dh \quad (\text{or } TN_4 = N_2 - TN_3, \text{ where } N_2 \text{ is the}$$

original number of drops in bin 43, layer 2) and

$$TNH_4 = \int_{h_4+\Delta h}^{h_3} n_h h dh - v_T \Delta t TN_4. \quad \text{In the event no drops fall}$$

out of a particular layer, e.g., when only the top part of a layer is occupied by drops, the total NH in the layer is simply decreased by $N v_T \Delta t$ - the loss of gravitational potential energy or position due to sedimentation.

Obviously in order to be consistent and get the proper result, some NH must be transferred during condensational growth and some M must be transferred during sedimentation. In both cases the amount of M and NH transferred is proportional to the number transferred. Thus the transfer of NH associated with the condensational growth depicted in Figure 10 is given by $TNH_{35} = \frac{TN_{35}}{N_{34}} * NH_{34}$ and $TNH_{36} = \frac{TN_{36}}{N_{34}} * NH_{34}$, while the transfer of mass associated with the sedimentation shown in Figure 11 is $TM_3 = \frac{TN_3}{N_2} * M_2$ and

$TM_4 = TN_4 / N_2 * M_2$. In this manner, the time change in the number, mass, and NH parameter of the droplets within a particular radius or height interval can be determined following sedimentation and condensation.

E. Stability Considerations for Condensation Growth

One aspect of the condensation calculation which must always be considered is the problem of computational instability associated with the extremely fast response time of small haze droplets to condensational growth or evaporation prior to nucleation. Physically, this suggests an equilibrium condition may be approached between the droplet radius and the ambient saturation ratio. To treat the growth of small droplets explicitly, very small time steps must be used to ensure stability. Mordy (1959) first suggested placing the droplet back on its equilibrium curve (given by Köhler's Equation) as a way to avoid the problem. This approach has been picked up by subsequent workers and is now used almost exclusively. Takahashi (1976), however, uses a .001 sec time step for his wet salt calculations whereas Lala and Juisto (1972) derive a droplet growth equation valid for smaller particles, lower humidities and having less stringent stability requirements by assuming the ambient saturation ratio equals the saturation ratio over the drop.

When the condensation calculation is started at or near cloud base, i.e., 100% relative humidity, repositioning the small haze particles back on the equilibrium curve requires solution of the dilute version of Köhler's equation, which is a cubic. However, in the present model the dilute drop approximation cannot be made for the haze particles and therefore the complete Köhler equation must be solved. This is accomplished via an iterative technique with the initial guess of the equilibrium radius (r_e) dependent on the bin and the ambient saturation ratio (needed to insure convergence). Once the method converges to the proper radius, a check is made to determine if the normal growth equation predicted a radius $> r_e$, in which case growth only to a size r_e is allowed. With this procedure, larger haze particles which have a slow response time, i.e., they "lag" their equilibrium radius, are not repositioned.

Analogous to the problem of computational stability associated with haze particle growth is the fast response time of a relatively old (large mean radius) or dense droplet distribution to changes in humidity. Arnason and Brown (1971) analyzed this stability problem for an explicit finite difference scheme and found that the maximum time step allowable for stability decreases as the population ages. They found the time step to be inversely proportional to the product of total drop number and mean

radius, as had been derived previously by Rooth (1960) in his statistical study of condensational growth. In the present model no problems with instability of this type were encountered. This was probably due to the implicit nature of the solutions to the continuity equations for ρ_v and T.

IV. Results and Discussion

In order to evaluate the performance of the model and to gain some insight into the relative importance of certain processes to the simulation of cloud chamber conditions, the results are presented as intercomparisons of the model at different levels of sophistication. Specifically, the various parameters and processes which will be investigated are organized as follows:

- (1) RUN A and RUN B are compared to determine the effect of different initial nucleus distributions. These runs, as well as all subsequent runs, are made with the PV of the model unless otherwise noted. RUN A is initialized with nuclei having $S^* \leq 1.01$, while RUN B has condensation nuclei (CN) with $1.30 \geq S^* \geq 1.01$.
- (2) RUN B and RUN C are compared to determine the effect of the radial fluxes of heat and vapor. RUN C includes the radial fluxes in parameterized form and has, as all subsequent runs, the same CN distribution as RUN B.
- (3) RUN C and RUN D are compared to determine the influence of the condensation coefficient. RUN C and

previous runs have $\alpha = 1.0$ and no adjusted thermal conductivity, while RUN D and each subsequent run have $\alpha = 0.3$ and a modified k .

(4) RUN D and RUN E are compared to determine the effect of nucleus bin resolution. RUN E has CN with $1.30 \geq S^* \geq 1.01$ divided into 15 bins whereas RUN D has the same nucleus distribution discretized into 6 bins.

(5) RUN D and RUN F are compared to determine the effect of parameterizing nucleation as opposed to including haze particles explicitly. RUN F is made with the FM.

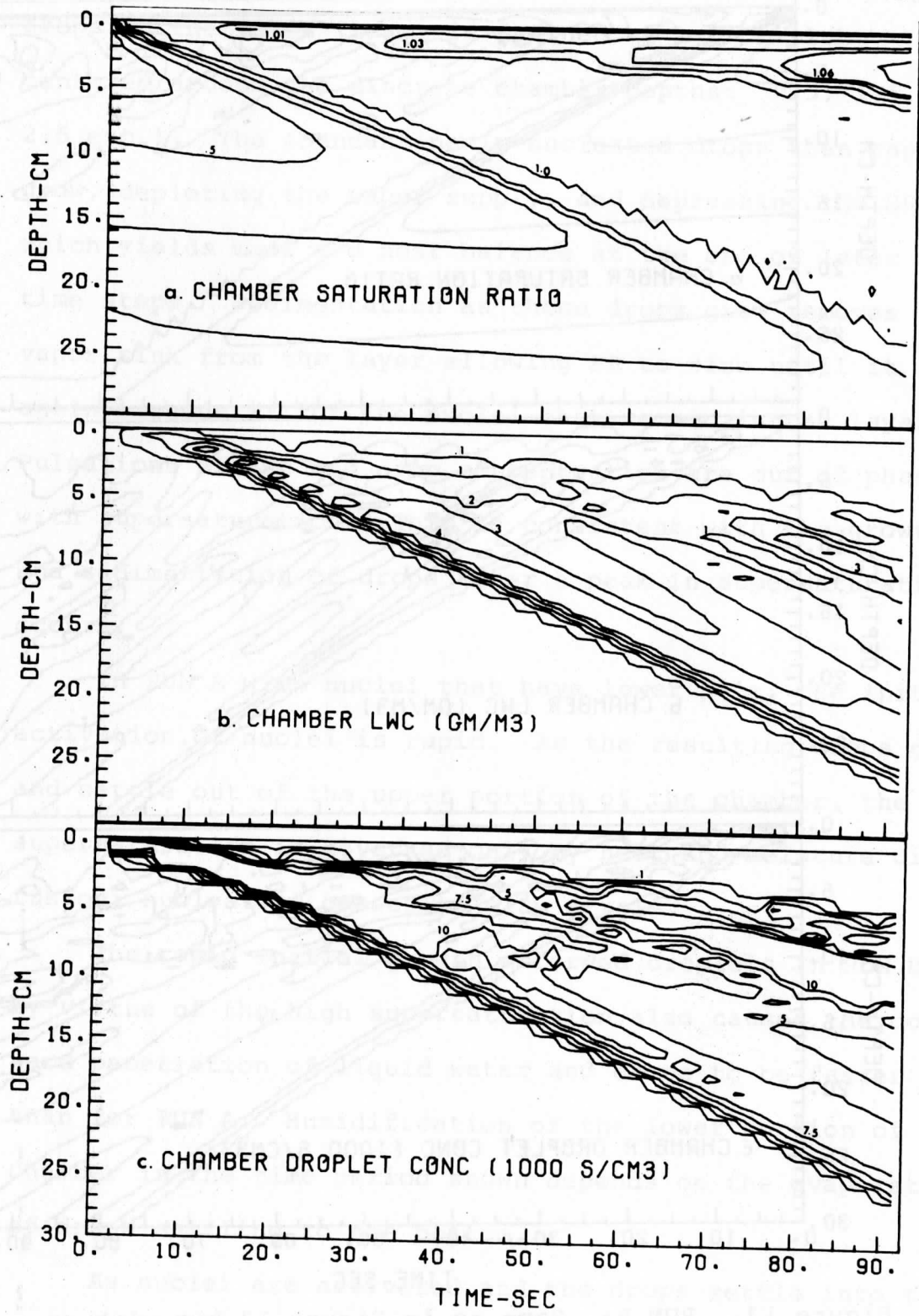
Computations for most of the above runs extend to 1 1/2 minutes although a run to four minutes will also be discussed. The primary microphysical data reported and compared include the saturation ratio (SR), liquid water content (LWC), and total droplet concentration (DC). These are presented as time-height cross sections for each parameter. Temperature profile evolution and hydrometeor number density are also determined and will be discussed where appropriate. The presentation of the results is arranged so as to culminate in the most complete model. Insights obtained from the various comparisons are then used to draw implications about the use of the SCC as an ice nucleus counter.

A. Effect of Condensation Nucleus Distribution

The first runs to be compared (Weickmann and Barchet, 1976) are those with different initial nucleus distributions using the PV of the model. RUN A (Fig. 12) has only nuclei with $S^* \leq 1.01$ in a Junge size distribution, while RUN B (Fig. 13) has mostly Aitken nuclei, i.e., $S^* > 1.01$. The two runs appear very similar; a supersaturated region quickly develops just beneath the warm moist chamber top while a deep region very near to 100% relative humidity quickly penetrates to the chamber floor. Similar temporal trends are seen in the liquid water and drop concentration. The general trends confirm Ohtake's (1971, 1976) observation that the chamber quickly fills with cloud and rapidly reaches water saturation in the isothermal lower portion of the chamber. However, it is in the details that the differences between the two runs become apparent.

Of special interest is the pulsating structure of all three parameters seen in both runs. This pulsation appears as sloping bands of alternating high and low saturation ratio, liquid water content, and droplet concentration in Figs. 12 and 13. The amplitude of the pulsation in all parameters is higher in RUN B where only Aitken nuclei are available. Pulsations arise as SR exceeds S^* within a nucleus bin. At the start of a time step the large SR causes a great increase in the number of actively growing

Figure 12. RUN A: The time-height cross-sections of model output saturation ratio (SR), liquid water content (LWC), and total droplet concentration (DC). Isopleth intervals are: SR - 0.2, 0.5, 0.7, 0.9, 1.0, 1.01, 1.03, 1.05, 1.06, 1.08, 1.1, 1.12, 1.14; LWC - 0.1, 1.0, 2.0, 3.0, 4.0; DC - 0.1, 1.0, 2.5, 5.0, 7.5, 10.0. Data points are at 1 cm intervals in space and 1 sec intervals in time except for $T < 2.5$ sec.



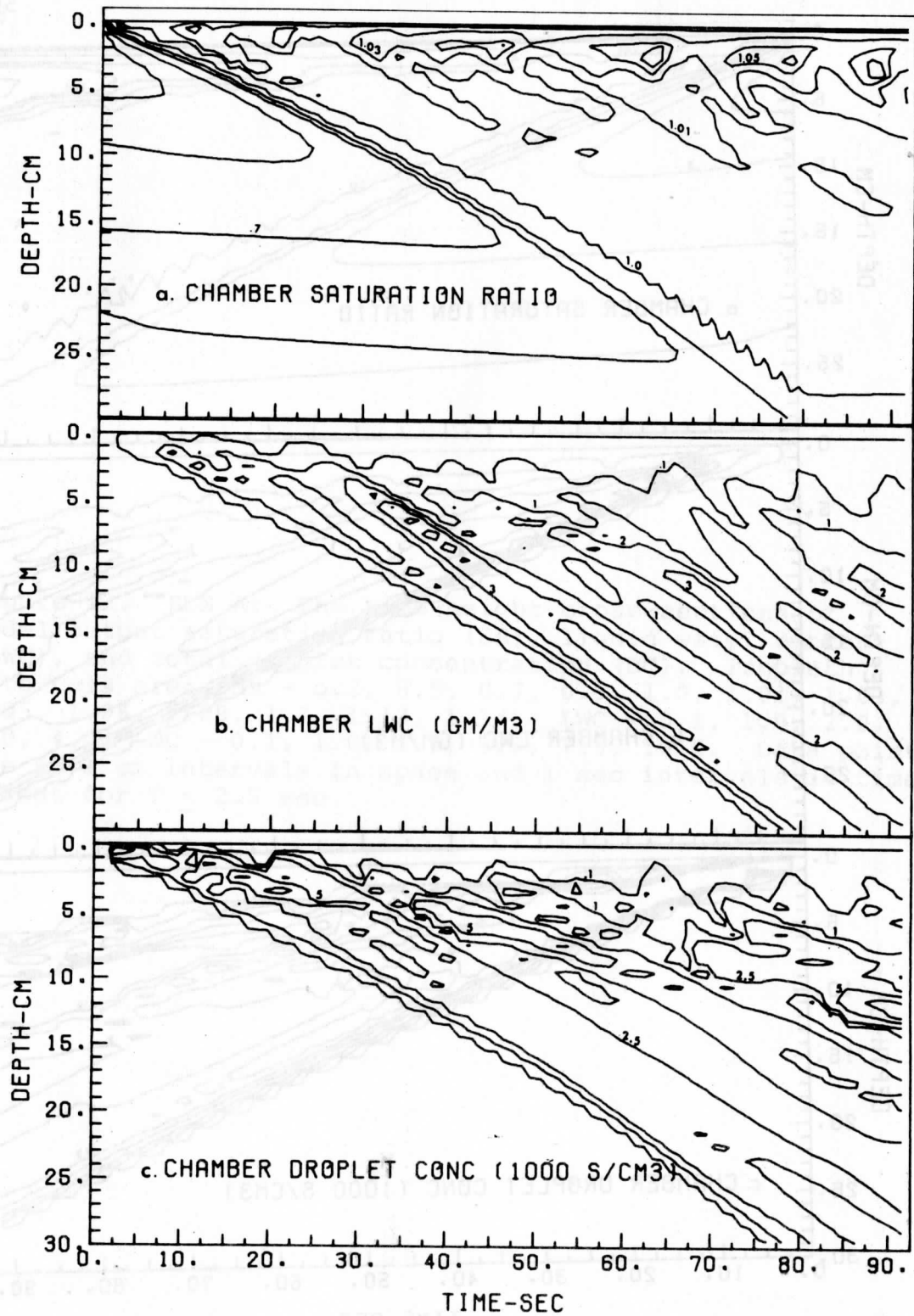


Figure 13. RUN B: Same as in Figure 12 but with an initial nucleus distribution having $S^* > 1\%$.

drops in the layer (layer is defined as a 1 cm slab centered around the discrete chamber depths: 0.5, 1.5, 2.5 etc.). The abundant newly-nucleated drops then rapidly grow, depleting the vapor supply, and depressing the SR which yields mass and heat balance at the end of later time steps. Sedimentation as those drops grow removes the vapor sink from the layer allowing SR to rise until it again exceeds S^* for the nuclei that remain in the layer. Pulsations of LWC and drop concentration are out of phase with supersaturation. This is consistent with the growth and sedimentation of drops after a peak in supersaturation occurs.

In RUN A with nuclei that have lower S^* 's, the initial activation of nuclei is rapid. As the resulting drops grow and settle out of the upper portion of the chamber, the supersaturation is governed only by heat and moisture diffusion; nucleation ceases to play a role.

The rapid initial growth afforded droplets in RUN B by virtue of the high supersaturation also causes the downward penetration of liquid water and drops to be faster than for RUN A. Humidification of the lower portion of the chamber in the time period shown depends on the evaporation of drops settling to the bottom.

As nuclei are activated and the drops settle into the chamber a gradual subsidence of the "cloud top" is evident in Figs. 12c and 13c. The rate of sinking of this top is

less with the Aitken nucleus run since nuclei with high S^* 's are available in the upper layers to later times.

The preceding results represent the only model runs made for different initial CN distributions. For reasons stated in the Introduction, subsequent results are all for nuclei with $S^* > 1.01$.

B. Effect of Radial Fluxes

As noted previously since the aspect ratio of the SCC is approximately 1.0 the walls should have a significant influence on the vertical distribution of heat and vapor. Figure 14 shows the deviation of model output temperatures from the observed temperature distribution for three different model runs. The curves with the largest temperature deviations correspond to RUN B, in which no heat and vapor sink were incorporated. The approach to a steady state in this case results in a nearly linear temperature gradient from the top of the chamber to the depth reached by the diffusion "front".

The other three curves represent cases in which vapor and heat sinks were included in the model. The curve corresponding to a relative humidity at the walls of 60% (RUN C*) gave fairly large negative deviations from the observed temperatures. Rapid evaporation of sedimenting drops (in the drier portion of the chamber) and cooling of the chamber air are responsible for these results. When

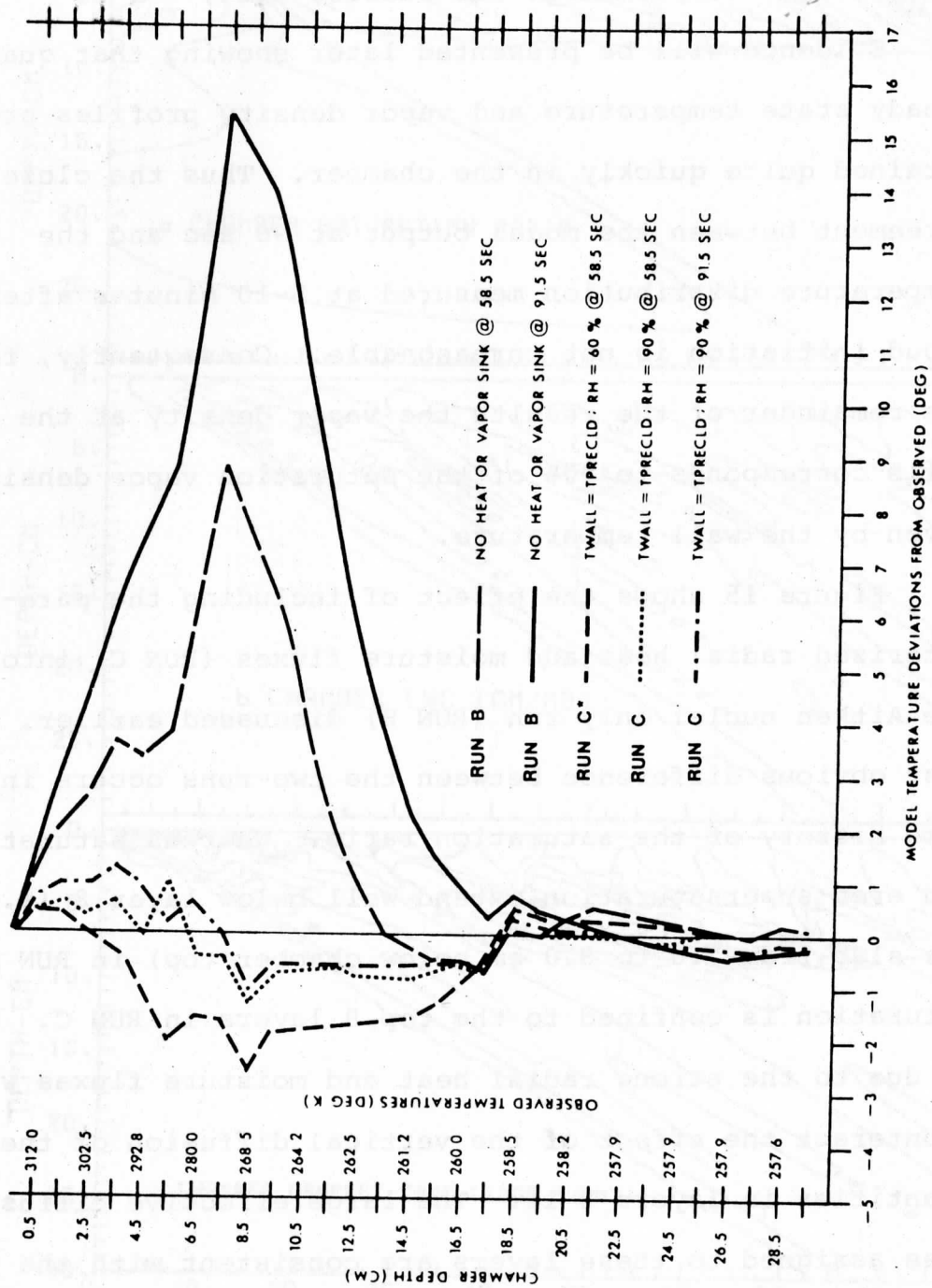


Figure 14. The deviations of model predicted temperatures from those measured in the chamber after cloud formation. The curves represent results at different times for two values of wall relative humidity.

using an RH of 90% for specifying the wall equilibrium vapor density (RUN C), the agreement between observed and model output temperatures are closer, i.e., $\leq 1^{\circ}\text{C}$.

Evidence will be presented later showing that quasi-steady state temperature and vapor density profiles are attained quite quickly in the chamber. Thus the close agreement between the model output at 90 sec and the temperature distribution measured at 5-10 minutes after cloud initiation is not unreasonable. Consequently, for the remainder of the results the vapor density at the walls corresponds to 90% of the saturation vapor density given by the wall temperature.

Figure 15 shows the effect of including the parameterized radial heat and moisture fluxes (RUN C) into the Aitken nuclei only run (RUN B) discussed earlier. The most obvious difference between the two runs occurs in the time history of the saturation ratio. Whereas saturation and even supersaturation extend well below layer 8 (i.e., the slab from 7.0 to 8.0 cm below chamber top) in RUN B, saturation is confined to the top 8 layers in RUN C. This is due to the strong radial heat and moisture fluxes which counteract the effect of the vertical diffusion of these quantities in layers 8-11. The large effective diffusivities assigned to these layers are consistent with the pronounced positive curvature of the measured temperature profile indicating a flux convergence of heat in this region.

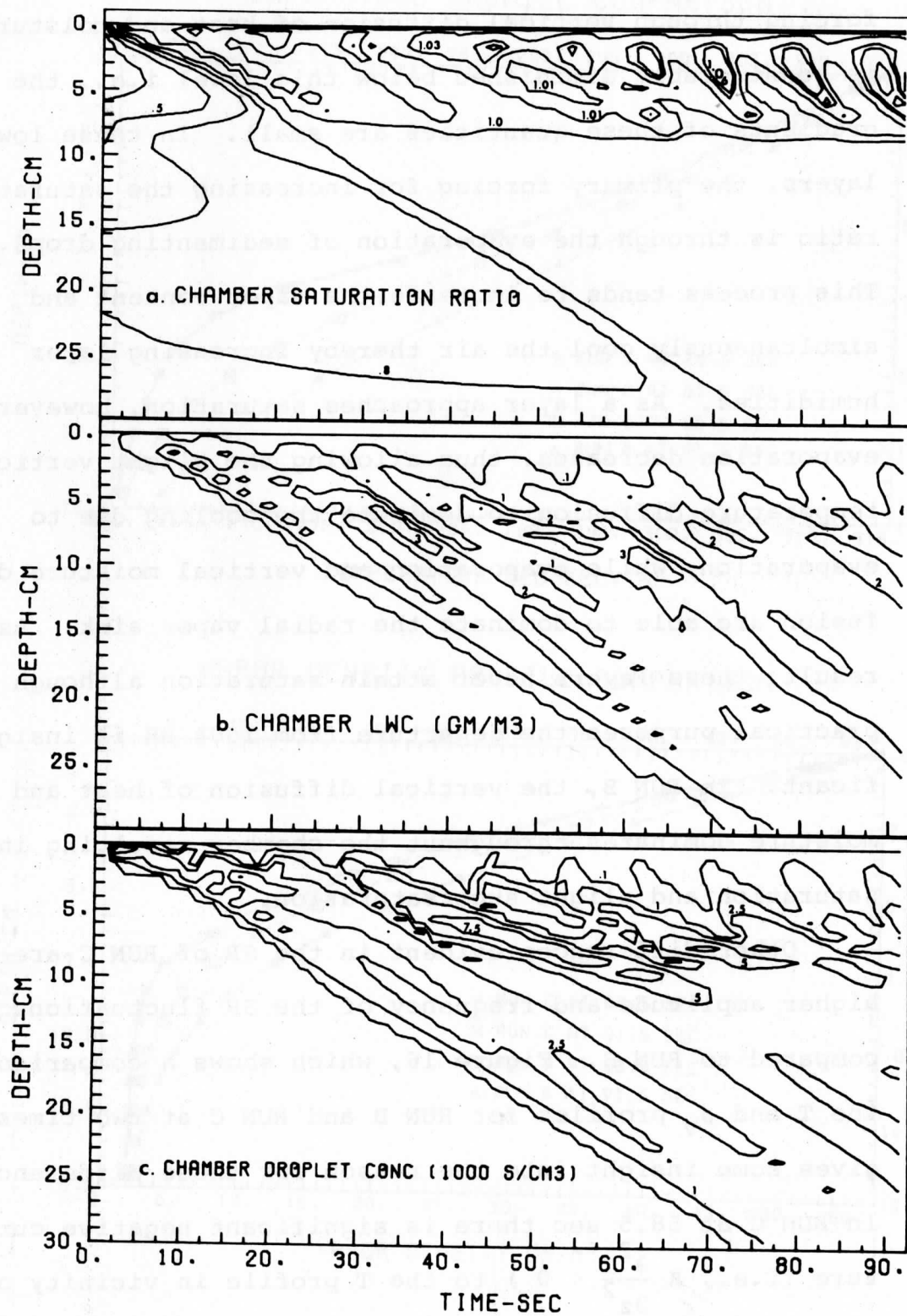
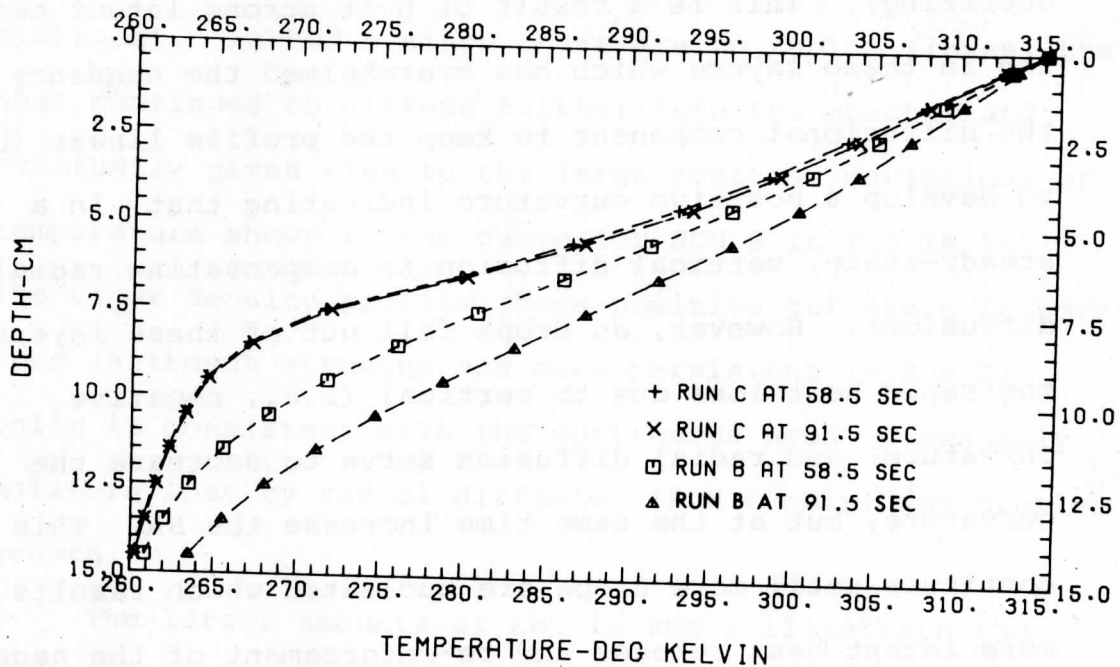


Figure 15. RUN C: Same as in Figure 13 but with radial heat and vapor sink included.

Saturation is not reached below layer 8 because the forcing through vertical diffusion of heat and moisture is considerably diminished below this level i.e., the gradients of these quantities are small. In these lower layers, the primary forcing for increasing the saturation ratio is through the evaporation of sedimenting drops. This process tends to increase the vapor content and simultaneously cool the air thereby increasing layer humidities. As a layer approaches saturation, however, evaporation decreases, thus allowing the slight vertical temperature diffusion to dominate the cooling due to evaporation, while evaporation and vertical moisture diffusion are able to dominate the radial vapor sink. As a result, these layers never attain saturation although for practical purposes the departure from 100% RH is insignificant. In RUN B, the vertical diffusion of heat and moisture dominates throughout the chamber resulting in saturation and slight supersaturation.

Other differences evident in the SR of RUN C are the higher amplitude and frequency of the SR fluctuations when compared to RUN B. Figure 16, which shows a comparison of the T and ρ_v profiles for RUN B and RUN C at two times, gives some insight into the reason for these differences. In RUN C at 58.5 sec there is significant negative curvature (i.e., $K \frac{\partial^2 T}{\partial z^2} < 0$) to the T profile in vicinity of the

TEMPERATURE PROFILE COMPARISON



VAPOR DENSITY PROFILE COMPARISON

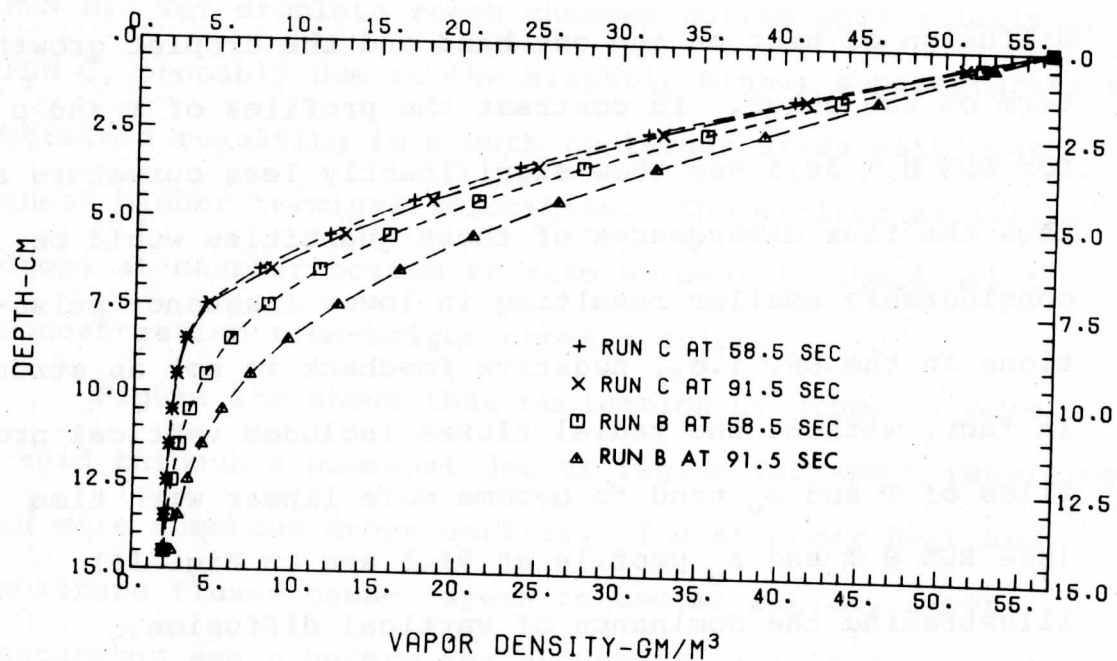


Figure 16. Comparison of the temperature and vapor density profile predicted by the model for RUN B and RUN C.

active layers 1-7 (i.e., where nucleation and growth is occurring). This is a result of past strong latent heating in these layers which has overwhelmed the tendency for the diffusional component to keep the profile linear (or to develop a positive curvature indicating that, in a steady-state, vertical diffusion is compensating radial diffusion). However, as drops fall out of these layers the rapid heat loss due to vertical (i.e., negative curvature) and radial diffusion serve to decrease the curvature, but at the same time increase the SR. This continues until more drops are nucleated which results in more latent heat release and re-enforcement of the negative curvature in the T profile. There is thus a strong negative feedback or coupling between vertical and radial diffusion of heat on the one hand and the droplet growth term on the other. In contrast the profiles of T and ρ_v for RUN B @ 58.5 sec show significantly less curvature and thus the flux divergences of these quantities would be considerably smaller resulting in lower frequency pulsations in the SR, i.e., negative feedback is not as strong. In fact, without the radial fluxes included vertical profiles of T and ρ_v tend to become more linear with time (see RUN B T and ρ_v profile at 91.5 sec in Fig. 16) illustrating the dominance of vertical diffusion.

In RUN C most of the heat realized through droplet growth in the active layers diffuses into layers 8-10

(positive curvature) where the wall heat sink is the strongest. In RUN B since there are no radial fluxes, the heat continues to diffuse further into the chamber and eventually gives rise to the large positive deviations of temperature shown in the curve for RUN B in Figure 14. The vapor density profile shows positive curvature in both runs (although stronger and more persistent in RUN C) which is consistent with the continuous need to resupply moisture lost by radial diffusion (RUN C only) and droplet growth.

The larger amounts of LWC in RUN B illustrate the effect of evaporation in the subsaturated layers of RUN C (caused by the wall vapor sink) versus continued growth in RUN B. Yet droplets reach chamber bottom more quickly in RUN C, probably due to the slightly higher supersaturations attained resulting in growth to larger sizes with consequent higher terminal velocities. The earlier arrival of drops at chamber bottom is also evident in the droplet concentration time-height cross section.

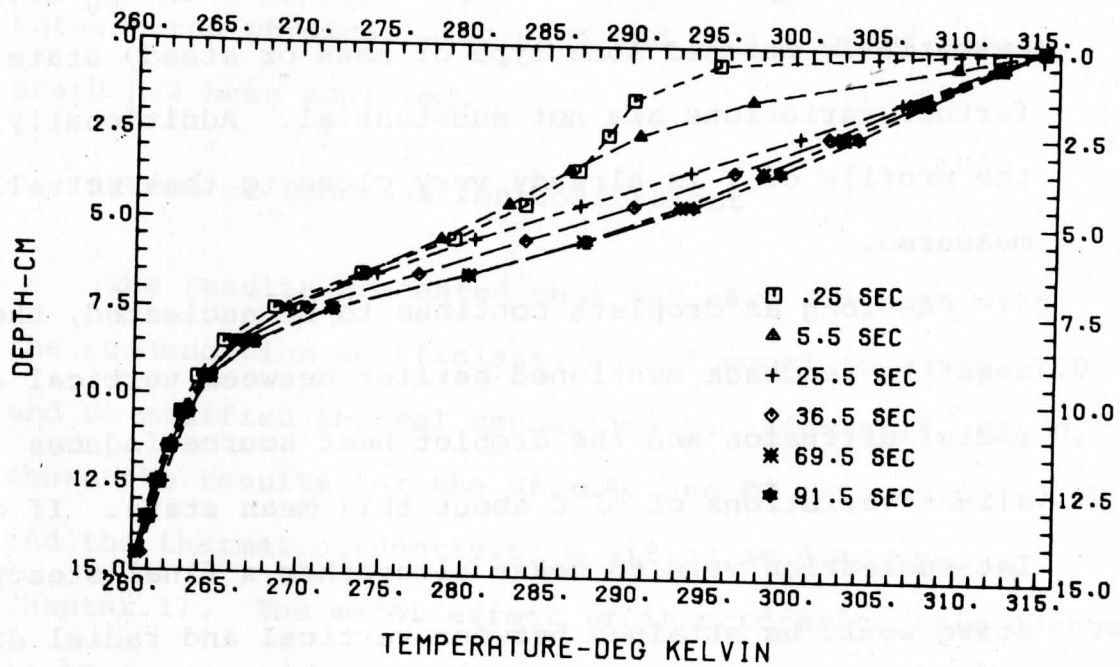
Figure 15c shows that nucleation of drops is more rapid through a somewhat deeper region for RUN C resulting in more numerous drops earlier. The stronger heat and moisture fluxes cause layers to become rapidly supersaturated again before the growth of nucleated drops depresses the SR. In RUN B significant supersaturation of the lower layers, e.g., below 2 or 3, is more gradual,

eventually penetrating there after 70 sec when the 1.03 line finally reaches layers 3-5. The large number of drops in RUN B after ~ 75 sec is due to this penetration and the supersaturated conditions in vicinity of layer 10.

At this point, since the major physical processes are now included in the model, it is instructive to study the time evolution of the T and ρ_v profiles for RUN C. Figure 17 shows these sequences starting with the conditions at $T = .25$ sec and going through 90 sec.

Initially the vertical temperature distribution has a curvature which indicates that the plexiglas walls are acting as a heat source in vicinity of layers 2-6 while an obvious heat sink is present (i.e., the brass cylinder walls) in layers 6-9. As the moist heated top is put into place vertical diffusion of heat and moisture rapidly increase the values of T , ρ_v and SR. Eventually drops are nucleated in layer 1 which release latent heat as they grow and give rise to a negative curvature in the T profile @ 5.5 sec. As more layers become saturated and nucleated drops sediment the area of maximum latent heating (and the attendant negative curvature in the T profile) migrates down into the chamber. This results in more linear profiles in uppermost layers (e.g., 1 and 2) thus keeping the SR nearly steady there. Droplets continue to be nucleated in lower layers and by 69.5 sec have

EVOLUTION OF TEMPERATURE PROFILE



EVOLUTION OF VAPOR DENSITY PROFILE

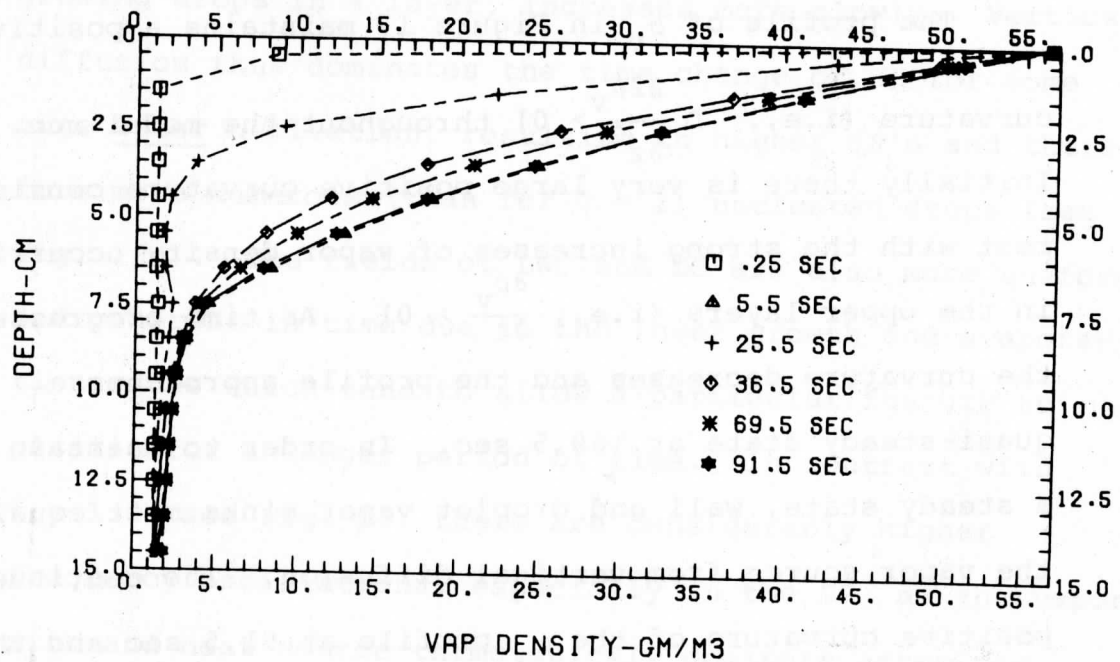


Figure 17. Time evolution of temperature and vapor density profiles for RUN C.

resulted in a very pronounced negative curvature in the T profile. By this time the profiles of T and ρ_v have essentially reached some type of mean or steady state as further variations are not substantial. Additionally, the profile of T is already very close to that actually measured.

As long as droplets continue to be nucleated, the negative feedback mentioned earlier between vertical and radial diffusion and the droplet heat source induces slight variations of $\sim 1^\circ\text{C}$ about this mean state. If droplet nucleation were to cease altogether a final steady state would be attained between vertical and radial diffusion highlighted by a slight positive curvature to the T profile.

The profile of ρ_v in Figure 17 maintains a positive curvature (i.e., $D \frac{\partial^2 \rho_v}{\partial z^2} > 0$) throughout the model run. Initially there is very large positive curvature consistent with the strong increases of vapor density occurring in the upper layers (i.e., $\frac{\partial \rho_v}{\partial t} > 0$). As time progresses the curvature decreases and the profile approaches a quasi-steady state at ~ 69.5 sec. In order to maintain a steady state, wall and droplet vapor sinks must equal the vapor source from vertical diffusion. The continued positive curvature of the ρ_v profile at 91.5 sec and the slight differences between the profile at 69.5 sec versus

91.5 sec indicates that a balance is being maintained between the physical processes and that a quasi-steady state has been achieved.

C. Effect of Condensation Coefficient

The results presented thus far have all been with the condensation coefficient, α , set equal to unity (1.0) and no modified thermal conductivity. Figure 18, RUN D, shows the results for the SR, LWC and DC with an $\alpha = 0.03$ and the thermal conductivity modified as discussed in Chapter II. The major effect of incorporating this change is to decrease the response time of the SR to newly nucleated drops, i.e., the vapor sink, represented by growing drops in a layer, increases more slowly. Vertical diffusion thus dominates the time change of SR for some time after nucleation, resulting in higher SR's and therefore more numerous (than for $\alpha = 1$) nucleated drops (see Fig. 18c). The fields of LWC and DC are also more uniform and coherent in time due to the lower growth and evaporation rates which tend to allow a particular feature to persist for a longer period of time. In contrast with $\alpha = 1.0$ (see Fig. 15) there are considerably higher frequency oscillations, especially in the SR, as the vapor sink and heat source terms quickly dominate after new drops are nucleated.

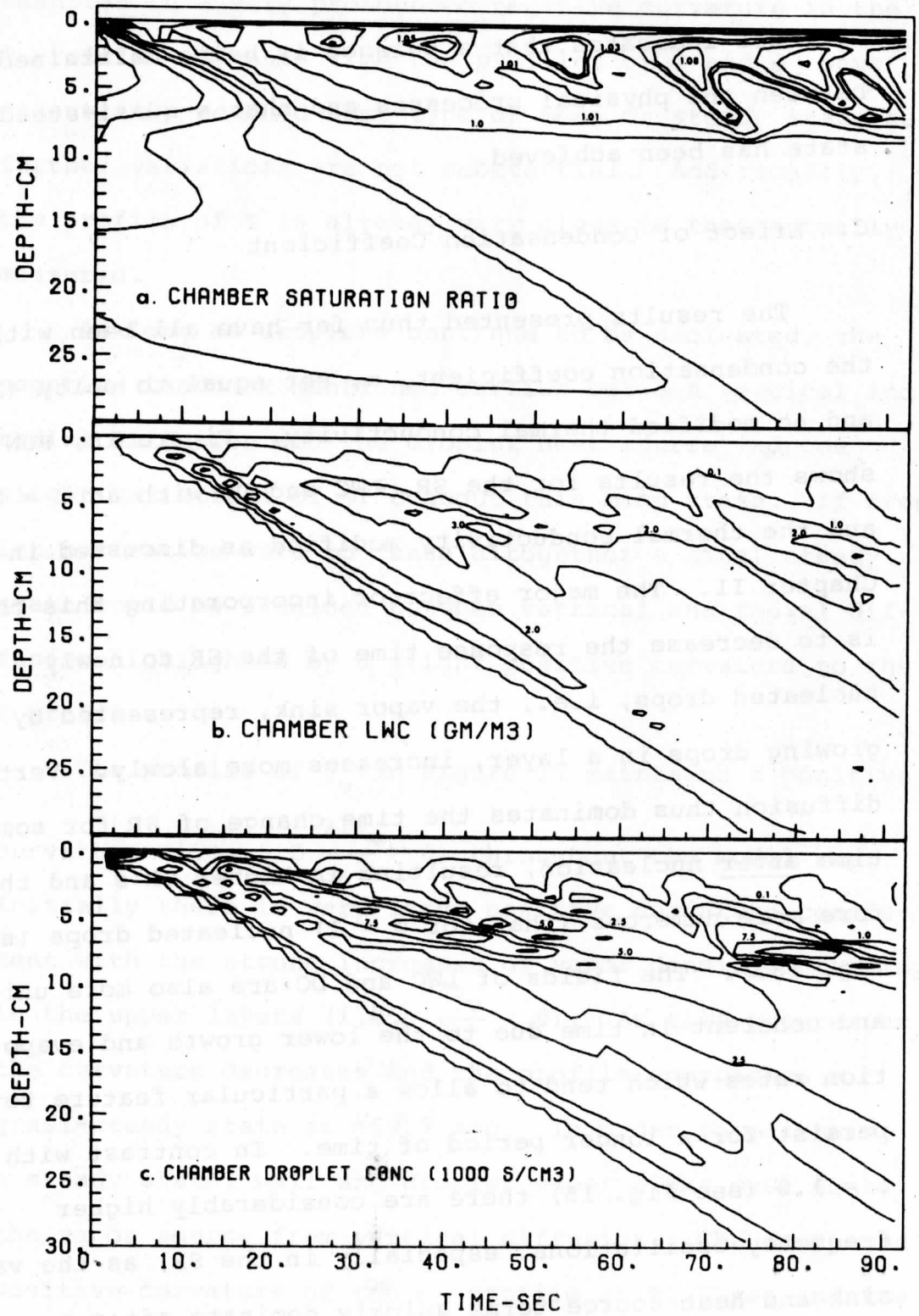


Figure 18. RUN D: Same as in Figure 15 but with $\alpha = 0.03$.

One aspect of the results with $\alpha = 1.0$ which should be noted is the tendency for the SR pulsations to repeatedly attain the same maximum value, in this case 1.06. This is a result of the assumption, noted in Chapter III, that nuclei are redistributed over the entire bin after nucleation of part of the bin. Thus the previous high value of the SR in a layer need not be exceeded before nucleating more drops. Therefore with $\alpha = 1.0$, where growth of nucleated drops is much more rapid, the SR tends to peak around a particular value. However, with $\alpha = 0.03$ even with the spurious nucleation of drops the SR continues to increase (over the past maximum value) since the slow growth of these drops does not depress the SR as rapidly.

Another interesting feature evident in both runs, but more obvious in RUN D is the sudden extension of high relative humidity into layers 5-8 after 60-70 seconds. The reason for this intrusion can be understood by examining the sequence of events in layers 1-4 and 5-8 separately. In the upper layers of both runs the successive pulsations and increases in magnitude of the SR cause discrete populations of drops to be nucleated by CN having larger and larger S^* 's. In RUN C these drops rapidly grow and fall out of the layers in which they were nucleated, whereas the growth is considerably retarded in RUN D (since $\alpha = 0.03$). This is evident in the time-height cross sections of RUN C's LWC and SR which display a somewhat

higher pulsation frequency compared to RUN D due to the more rapid growth and fallout of drops. Eventually as the SR continues to increase, nucleated drops grow more rapidly to large radii (in both RUN C and RUN D) since $dr/dt \propto \frac{1}{r} (SR-1)$. In RUN C, the rapid growth and fall out of drops in the upper layers leads to intermittent pulses in the LW flux of drops to lower layers. In RUN D, however, the slower growth rates (since $\alpha = 0.03$) keep the LW flux to lower layers more uniform - at least up to a particular point in time.

In the lower layers (5-8) of both runs the SR tends to be depressed by the drops falling into these layers from above, i.e., the droplet vapor sink nearly balances the vertical diffusion so that SR stays close to 1.0. The SR is considerably steadier in RUN D as would be expected since the flux of LW from upper layers is more uniform. In RUN C the SR is less steady as gaps in the LW flux occur which allow vertical diffusion to temporarily dominate and increase the SR. However, in both runs an obvious extension of high SR suddenly occurs, at 60 sec in RUN C and 68 sec in RUN D. Drops nucleated at the increasingly higher supersaturations in the upper layers grow so rapidly that they fall into and through the lower layers before more drops can be nucleated. This comes about when the time period required for drops to traverse layers 1-7 is less than the time needed for the SR to recover in 1-4

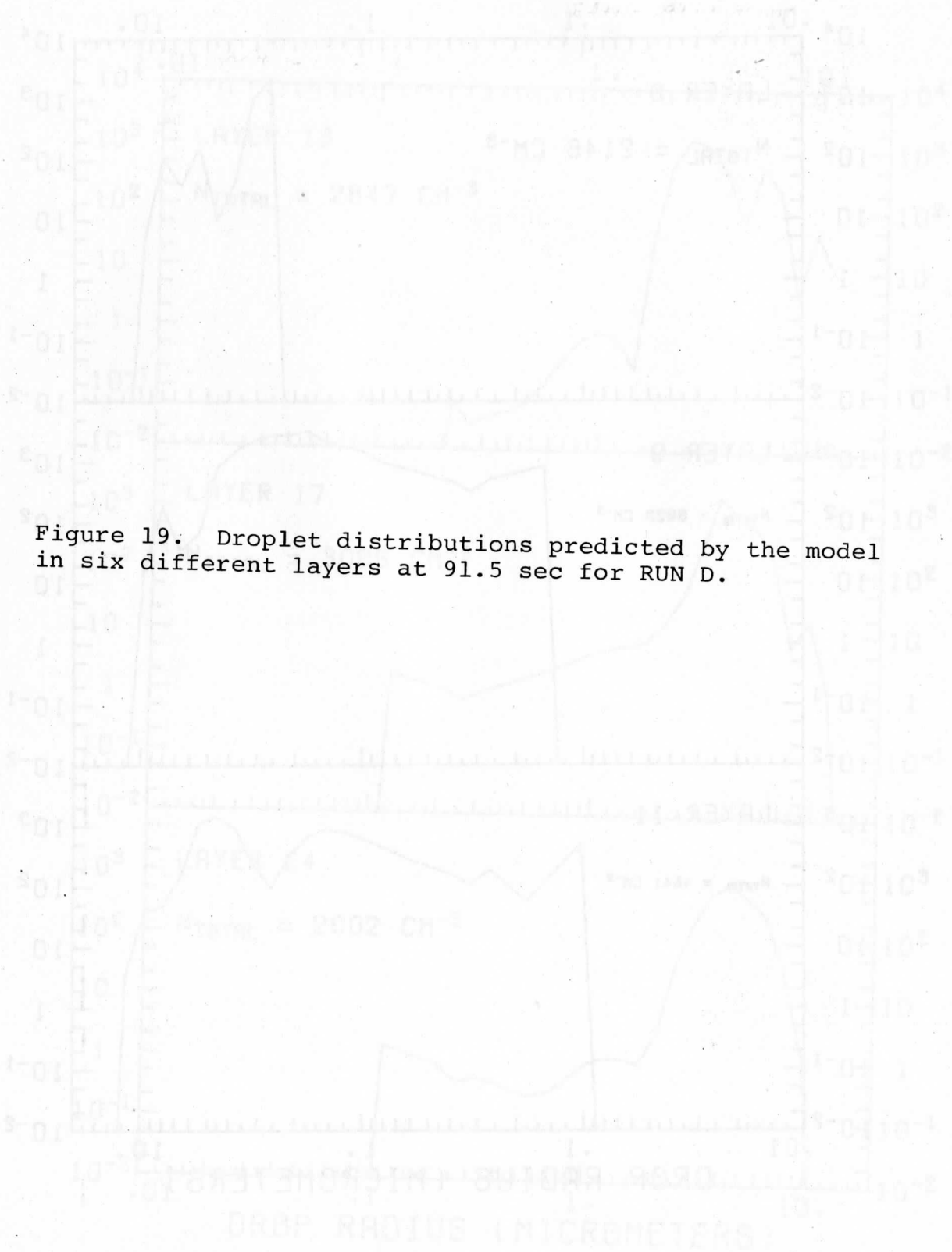
via vertical diffusion. The suddenness of the SR increase is a result of the strong *flux divergence* curvature of the vapor and *heat* temperature profiles set up by the previous condensational growth in these layers, i.e., have a continued gain of vapor and loss of heat without a latent heat source to reverse this trend. The extension of high supersaturation is more dramatic in RUN D since the SR in the lower layers has been kept fairly steady whereas in RUN C vertical diffusion has already occasionally dominated due to gaps in the LW flux from above.

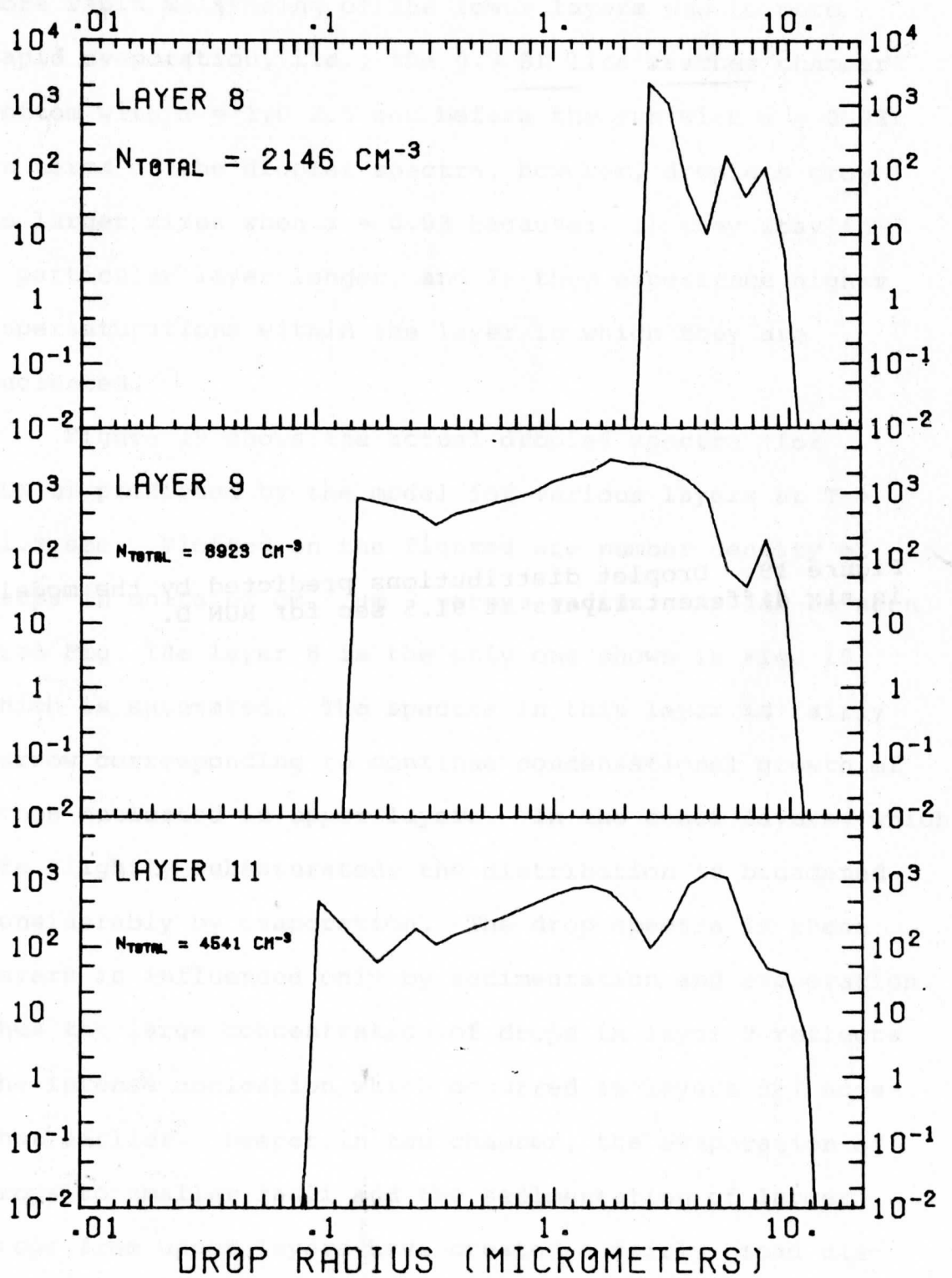
Figure 18b confirms this scenario as rapid decreases in LWC occur in several layers at ~ 70 sec due to the combination of more rapid fallout and lack of droplet replenishment in the layers. The sudden downward extension is also very evident in the DC cross-sections as droplet concentrations exceed $10,000 \text{ cm}^{-3}$ in layer 8 due to nucleation in this layer and sedimentation from above. The intense nucleation caused by this phenomena contributes partly to the development of a layer of maximum DC (or a cloud top) as the drops nucleated are so numerous and compete so strongly that further growth is inhibited. More will be said about the maintenance of this "cloud top" later.

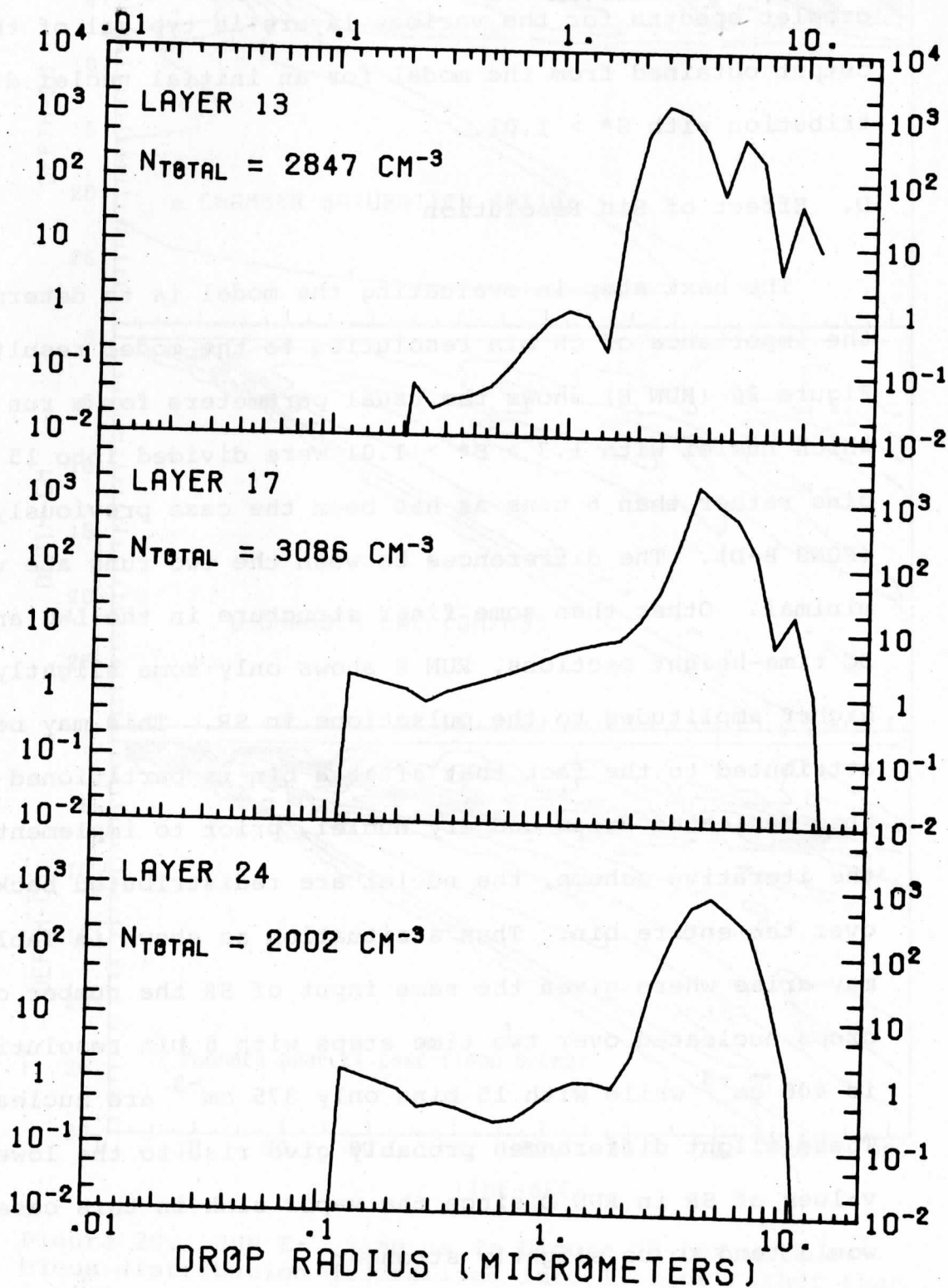
Another feature evident in the LWC and DC cross sections of Figure 15 is that droplets reach the bottom of the chamber sooner when $\alpha = 1.0$. This occurs due to

faster initial growth of nucleated drops and subsequent more rapid moistening of the lower layers due to more rapid evaporation, i.e., the 0.9 SR line reaches chamber bottom with $\alpha = 1.0$ 2.5 sec before the run with $\alpha = 0.03$. In terms of the droplet spectra, however, droplets grow to larger sizes when $\alpha = 0.03$ because: 1) they stay in a particular layer longer, and 2) they experience higher supersaturations within the layer in which they are nucleated.

Figure 19 shows the actual droplet spectra (for RUN D) predicted by the model for various layers at $T = 91.5$ sec. Plotted on the figures are number density of drops in units of $\text{cm}^{-3} \mu\text{m}^{-1}$ versus radius. As can be seen from Fig. 18a layer 8 is the only one shown in Fig. 19 which is saturated. The spectra in this layer is fairly narrow corresponding to continue^d condensational growth of drops nucleated in upper layers. In the other layers, which are slightly subsaturated, the distribution is broadened considerably by evaporation. The drop spectra in these layers is influenced only by sedimentation and evaporation. Thus the large concentration of drops in layer 9 reflects the intense nucleation which occurred in layers 5-7 somewhat earlier. Deeper in the chamber, the evaporation of drops to smaller radii and the sedimentation of larger drops from upper layers have created a fairly broad distribution, with drops less than $\sim 2\mu\text{m}$ being uniformly







distributed over $\log r$ while a pronounced peak in the distribution occurs near $5\mu\text{m}$ radius. This sequence of droplet spectra for the various layers is typical of the output obtained from the model for an initial nuclei distribution with $S^* > 1.01$.

D. Effect of Bin Resolution

The next step in evaluating the model is to determine the importance of CN bin resolution to the model results. Figure 20 (RUN E) shows the usual parameters for a run in which nuclei with $1.3 > S^* > 1.01$ were divided into 15 bins rather than 6 bins as has been the case previously (RUNS B-D). The differences between the two runs are very minimal. Other than some finer structure in the LWC and DC time-height sections, RUN E shows only some slightly higher amplitudes to the pulsations in SR. This may be attributed to the fact that after a bin is partitioned into nucleated drops and dry nuclei, prior to implementing the iterative scheme, the nuclei are redistributed back over the entire bin. Thus a situation as shown in Table 1 may arise where given the same input of SR the number of drops nucleated over two time steps with 6 bin resolution is 406 cm^{-3} while with 15 bins only 375 cm^{-3} are nucleated. These slight differences probably give rise to the lower values of SR in RUN D since the vapor sink in this case would tend to be slightly stronger.

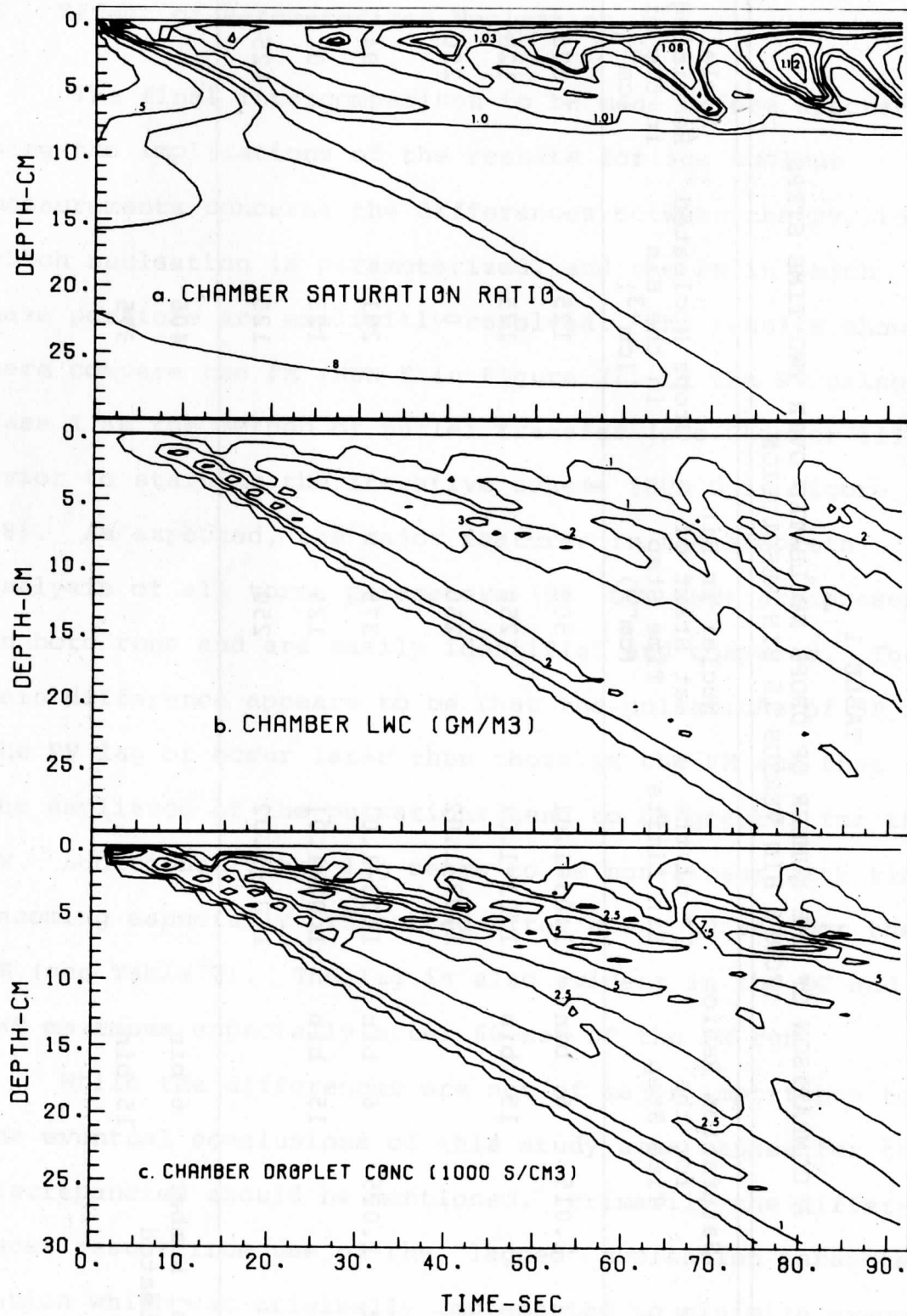


Figure 20. RUN E: Same as in Figure 18 but with nucleus distribution discretized into 15 bins rather than 6 bins.

TABLE 1
 A COMPARISON OF THE NUMBER OF DROPS NUCLEATED OVER TWO TIME STEPS
 FOR 6 BIN VERSUS 15 BIN RESOLUTION

Time Step	Saturation Ratio for the Time Step	S* of the Bin Limits	Nuclei in Bin at Start of Time Step (cm ⁻³)	Drops Nucleated in the Bin (cm ⁻³)	Nuclei Remaining in the Bin (cm ⁻³)
t	1.015	6 bin	500	125	375
		15 bin	250	125	125
			250	0	250
t+Δt	1.025	6 bin	375	281	94
		15 bin	125	125	0
			250	125	125
Total Number Nucleated		6 bin		406	
		15 bin		375	

E. Effect of Parameterized Nucleation

The final intercomparison to be made before discussing the implications of the results for ice nucleus measurements concerns the differences between the PV, in which nucleation is parameterized, and the FM in which haze particle are explicitly resolved. The results shown here compare the FM (RUN F in Figure 21) to the PV using Case I as the method of nuclei transfer (see Chapter III) prior to starting the iterative scheme (RUN D in Figure 18). As expected, the major features in the isopleth analysis of all three parameters (SR, DC, LWC) are present in both runs and are easily identified and compared. The main difference appears to be that the pulsations of SR in the PV lag or occur later than those in the FM and that the amplitude of the pulsations tend to be greater for the PV. Additionally the lag seems to be non-linear with time, becoming especially pronounced after about 50 sec for the SR (see Table 2). The lag is also evident in the DC and LWC maximums especially after 60 sec of the FM run.

While the differences are not of major importance to the eventual conclusions of this study some causes for the discrepancies should be mentioned. Primarily the differences result from use of the "lagged" nucleation parameterization which was originally implemented to minimize evaporation and subsequent loss of nucleated drops during the iterative scheme. When logic was added which allowed drops

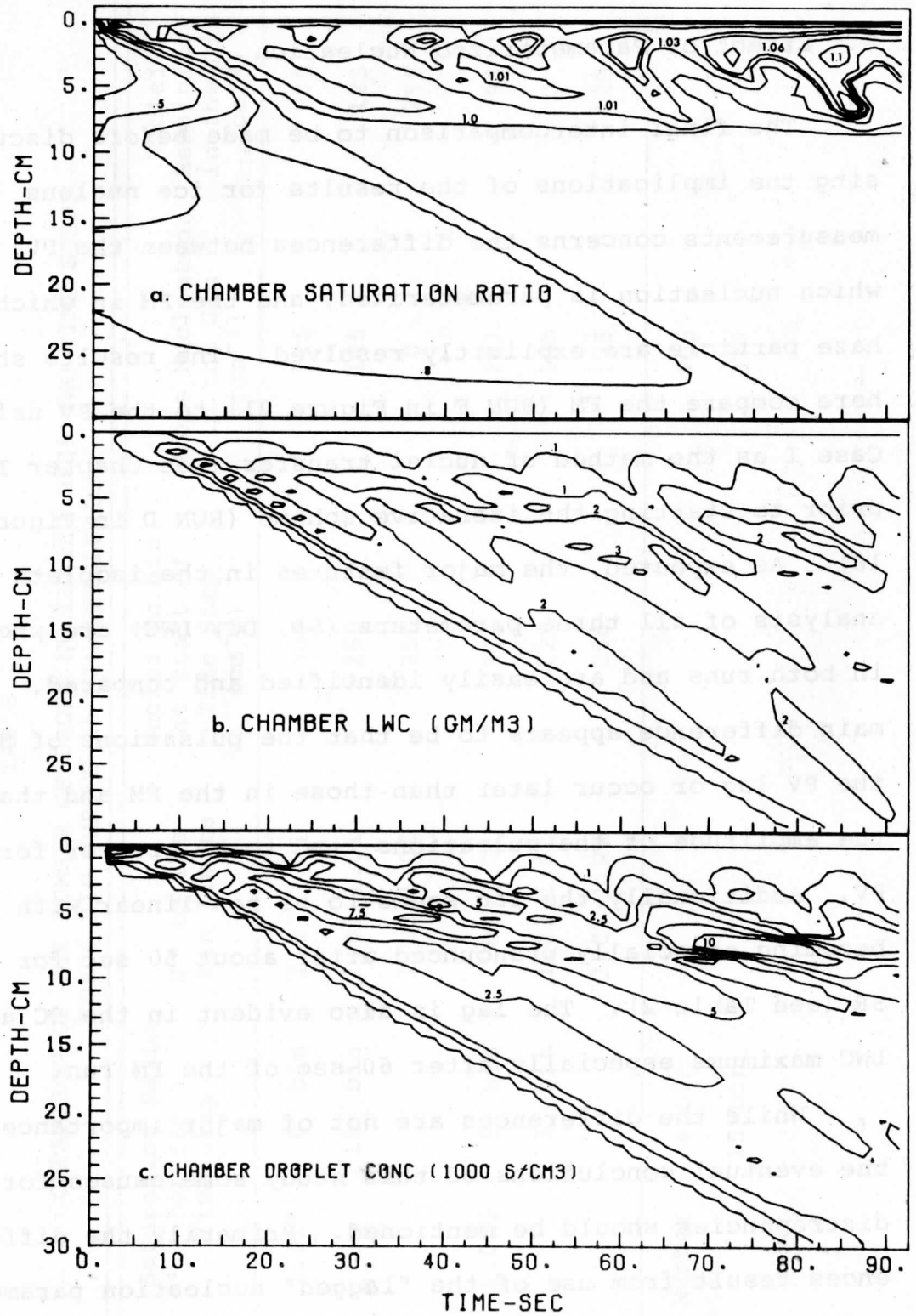


Figure 21. RUN F: Same as in Figure 18 but with the full version of the model.

TABLE 2
 THE DIFFERENCE IN TIME OF OCCURRENCE AND AMPLITUDE OF THE SR
 PULSATIONS FOR RUN D AND RUN F

Pulsation #	Time of Occurrence (sec)		Time Difference sec	Maximum Saturation Ratio Achieved	
	PV	FM		PV	FM
1	2.5	2.5	0	1.05	1.03
2	14.5	14.5	0	1.04	1.03
3	26.5	24.5	2	1.06	1.05
4	39.5	37.5	2	1.07	1.06
5	53.5	48.5	5	1.08	1.06
6	67.5	60.5	7	1.08	1.06
7	80.5	71.5	9	1.12	1.08
8	>91.5	84.5	>7	1.12	1.10

that had just been nucleated and subsequently evaporated to be returned to the proper nuclei bin, the lagged parameterization of nucleation was nevertheless, retained.

Several limitations of this approach appear to be responsible for the discrepancies shown between Figures 18 and 21. First, when the SR in a layer is increasing (i.e., vertical diffusion dominates) use of the past value of the SR to determine the nucleus bins which should be transferred to drops (prior to implementing the iterative scheme) results in the transfer of too few nuclei. For example, if the SR at $t-\Delta t$ equals 1.02, only nuclei with $S^* \leq 1.02$ would be transferred to drop bins. This may result in a balanced value of the SR at t of 1.05 which implies that more nuclei should have been transferred in order to obtain the proper balanced value of SR at t . Second, when the vapor sink eventually dominates diffusion, causing the SR to decrease substantially, newly nucleated drops that actually should have become actively growing in the previous time step may revert to CN. For example, if SR at $t-\Delta t$ equals 1.05, nuclei with $S^* \leq 1.05$ will be transferred; however, if SR at t is 1.02, many of these drops will "evaporate" when actually their S^* has already been equalled or surpassed.

These limitations result in: 1) a delay or lag in building up the SR for a particular pulsation as nuclei not activated in the previous pulsation become active,

2) an increase in the maximum value of SR for a particular pulsation as less nuclei are activated once the SR starts increasing again, and 3) an extension in time of a pulsation as drops erroneously evaporate when SR starts decreasing again. These factors are responsible for the phase and amplitude difference of the pulsations in SR between the PV and the FM. The fact that in the PV the LWC is lower, more uniform, and spread out over longer time (before the downward extension of low LWC @ 70 sec) implies that drops are still being nucleated in upper layers while in the FM this is no longer the case (i.e., more drops have been nucleated giving rise to higher LWC over a shorter time period).

Letting diffusion always determine the number of nuclei transferred to drops, i.e., Case II described in Chapter III, eliminates the problems with the PV discussed above. However, as programmed, this approach also has a flaw in that there is no partitioning of a nuclei bin into nucleated drops and "haze particles". Therefore, if the value of $SR > S_{cm}^*$ then the entire nucleus bin becomes activated although SR may be $< S_{e_i}^*$. Conversely, if $SR < S_{cm}^*$, then the entire bin is not activated although SR may be $> S_{e_{i+1}}^*$. Since this partitioning is used in the FM this difference leads to discrepancies similar to those shown in Fig. 22, in particular as the bin interval,

between Figs 18 & 21

i.e., $S_{e_i}^* - S_{e_{i+1}}^*$ gets larger. The discrepancy described could be easily eliminated and should lead to closer agreement between the FM and PV, however, since the differences are not large and in order to save computer time the model was not rerun with these corrections incorporated. In fact since general consistency of results has been demonstrated between the FM and the PV, all subsequent runs are made with the PV using "lagged" nucleation.

F. Summary of Model Results

The previous section emphasized the synthesis of the numerical model and demonstrated the relative importance of various parameters and processes in obtaining physically realistic results. Despite some minor departures of the PV from the FM, the results indicate that this version of the model gives a fairly reliable portrayal of the sequence of events occurring in the SCC. Additional verification of the model output in this section will also support the overall accuracy of the model.

Figure 22 shows the usual model output parameters using the PV but with an extended run out to 4 minutes. The sequence of events described in the Introduction is readily apparent in these time-height cross sections. Supersaturation quickly develops in the upper-most layers as moisture and heat diffusion dominate. Pulsations in SR are initiated as nucleation occurs and the vapor sink gets

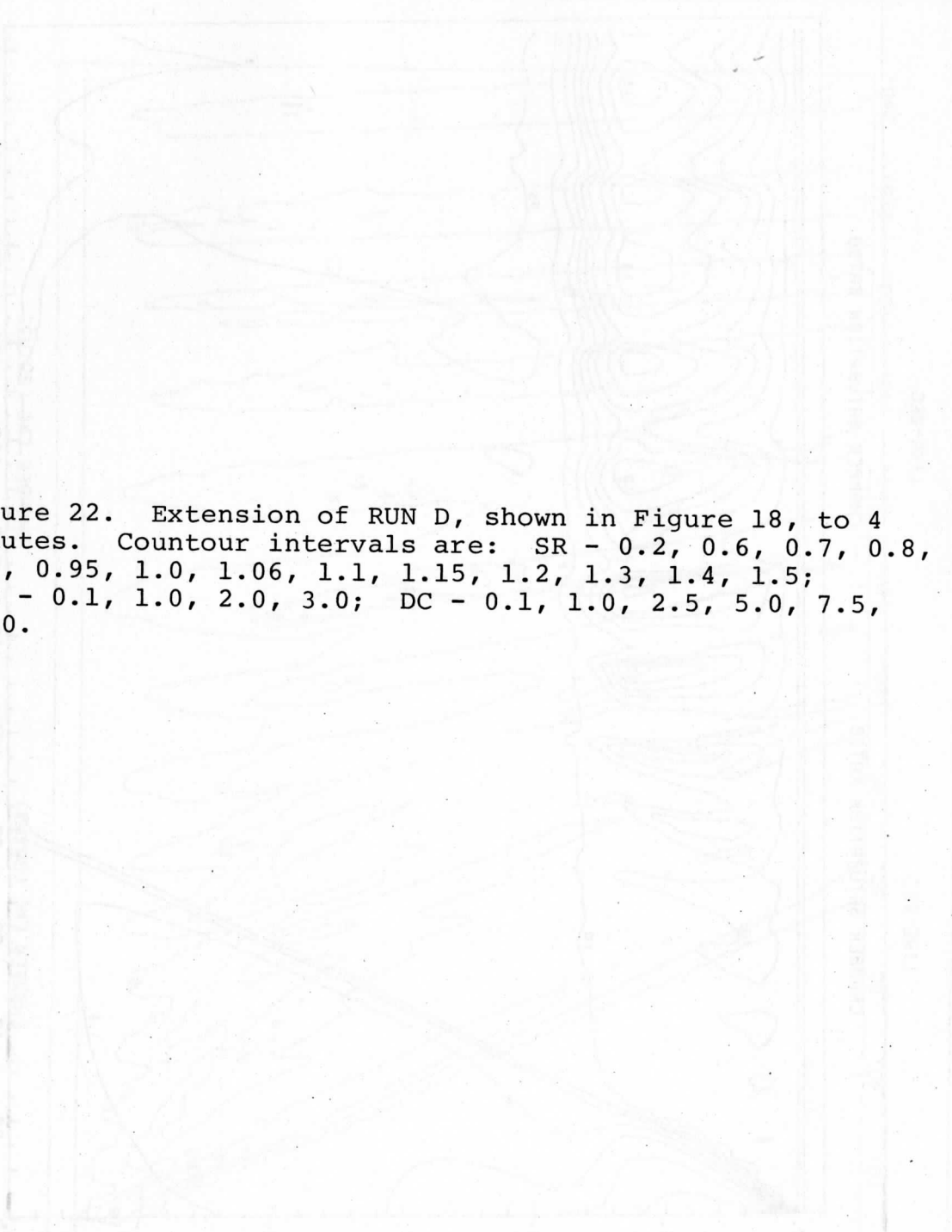
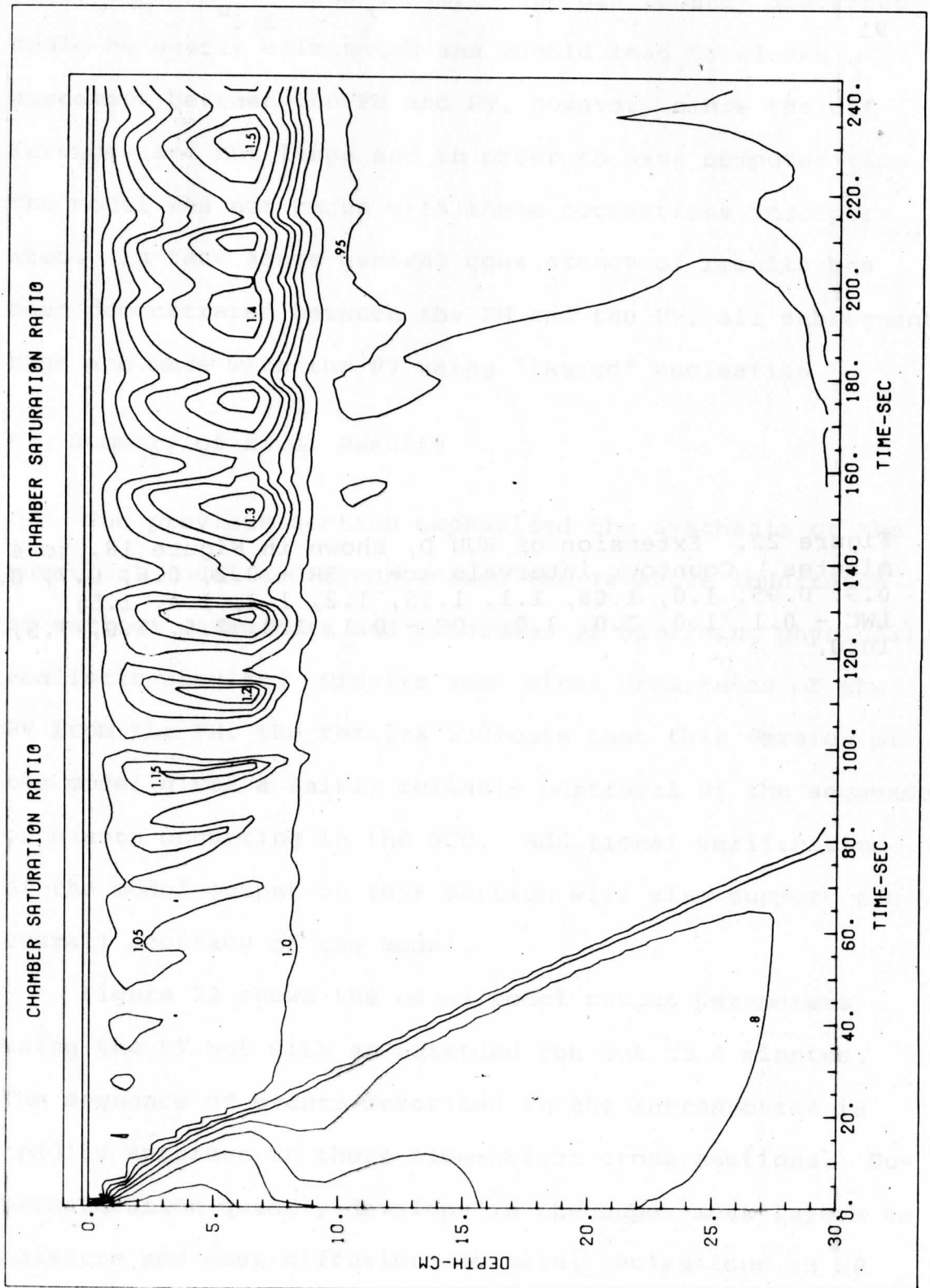
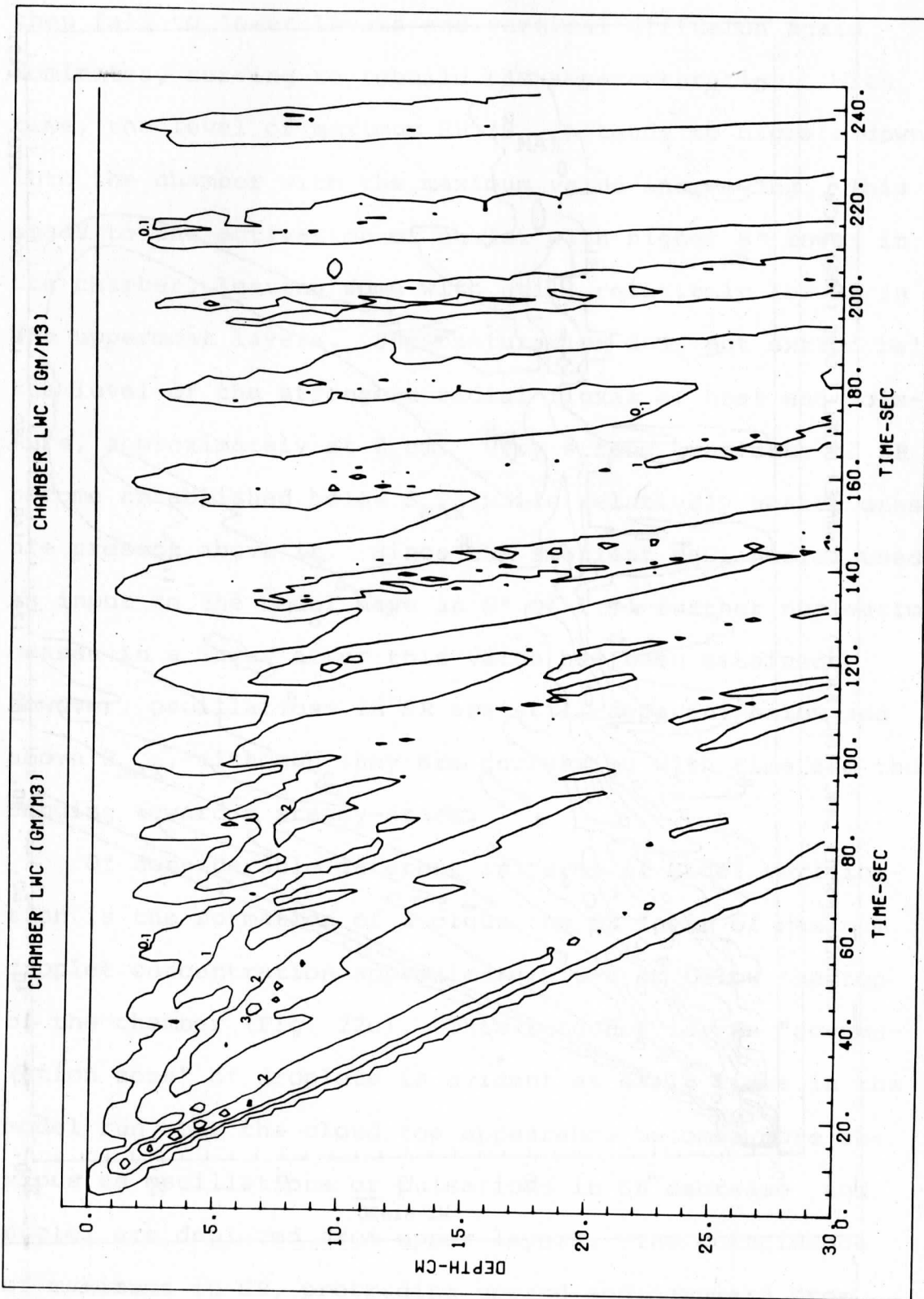
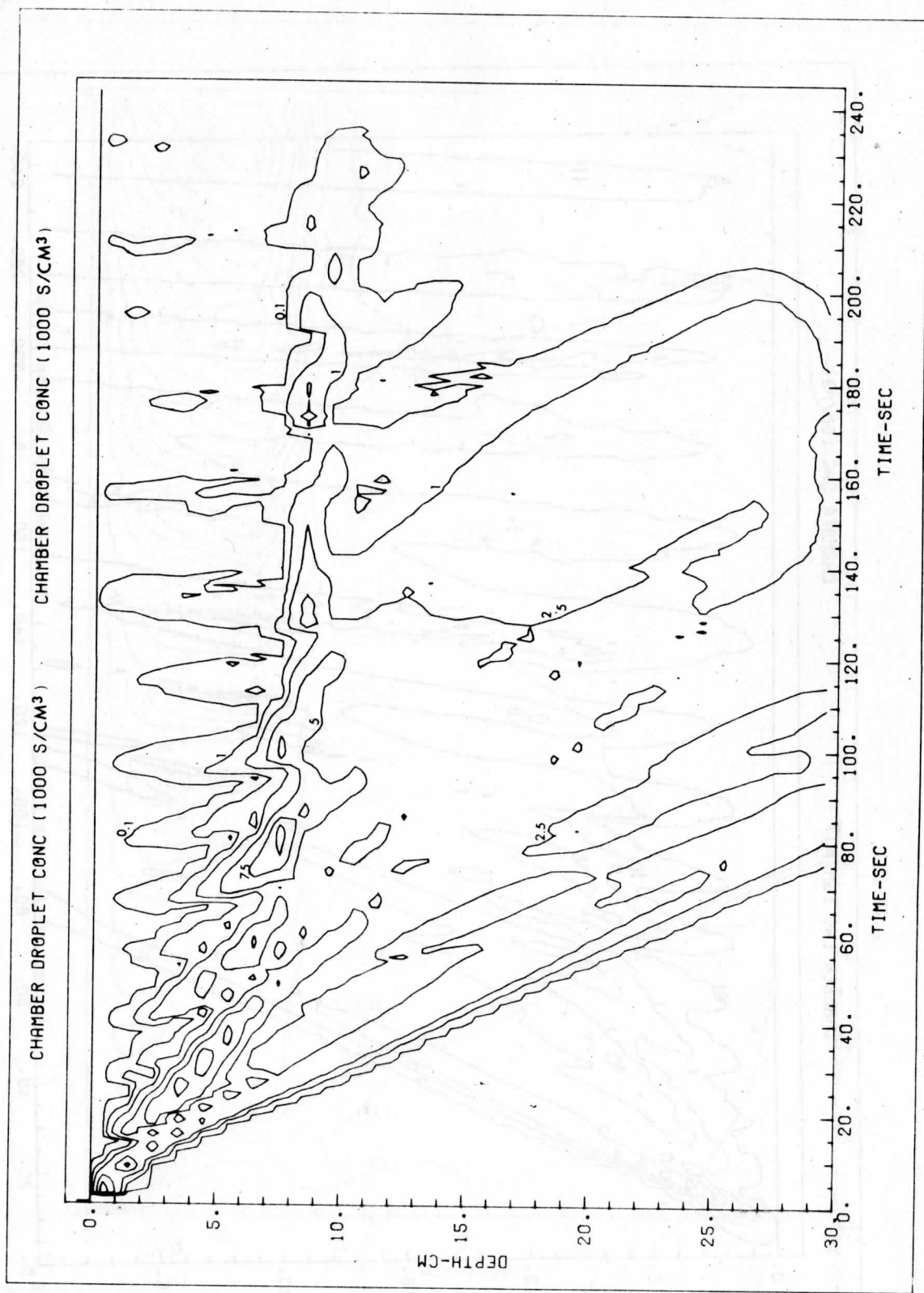


Figure 22. Extension of RUN D, shown in Figure 18, to 4 minutes. Contour intervals are: SR - 0.2, 0.6, 0.7, 0.8, 0.9, 0.95, 1.0, 1.06, 1.1, 1.15, 1.2, 1.3, 1.4, 1.5; LWC - 0.1, 1.0, 2.0, 3.0; DC - 0.1, 1.0, 2.5, 5.0, 7.5, 10.0.







large, driving down the supersaturation. Nucleated drops then fall to lower levels and vertical diffusion again dominates, serving to rebuild the supersaturation. With time, the level of maximum SR (S_{MAX}) tends to migrate down into the chamber with the maximum value increasing. This leads to the activation of nuclei with higher S^* lower in the chamber, leaving some with still relatively low S^* in the uppermost layers. Supersaturation does not extend below the level of the strongest radial fluxes of heat and moisture, approximately at 8 cm. Very strong gradients of SR become established below S_{MAX} while relatively weaker ones are present above it. Since the smallest NaCl nuclei used as input to the model have an S^* of 1.31 further nucleation ceases in a layer after this value has been attained. However, oscillations in SR are still apparent below and above S_{MAX} , although they are decreasing with time and thus tending toward a steady-state.

Of considerable interest in terms of model verification is the formation of a cloud top or layer of maximum droplet concentration approximately 6-8 cm below the top of the chamber (Fig. 22c). This tendency for an "accumulation zone" of droplets is evident at early times in the model run, but the cloud top appearance becomes more obvious as oscillations or pulsations in SR decrease and nuclei are depleted from upper layers. The coincidence of maximums in SR, protruding upward and downward from

S_{MAX} , with the appearance of maxima in droplet concentration indicate that nucleation is still occurring at ~ 3 min above and below S_{MAX} . Droplets nucleated in the upper layers rapidly grow to large sizes as they encounter higher supersaturation while sedimenting to lower layers. Streamers of large drops ($\sim 10 \mu\text{m}$) within otherwise clear air in the upper portions of the SCC have been observed in the Wisconsin and Ohtake (personal communication) chambers. These streamers can also be seen as maxima in LWC (Fig. 22b) emanating from upper layers which quickly penetrate to the chamber bottom.

In contrast drops nucleated below S_{MAX} encounter strongly decreasing SR as they sediment, with their water uptake being small compared to drops activated above S_{MAX} . Thus the apparent cloud top evident in the DC cross sections and observed in the chamber probably is maintained by drops which are nucleated in layers 7-9. These drops quickly grow to beyond visible size, but further growth is limited due to decreasing SR and eventual subsaturation immediately below the area of nucleation. The drops from above S_{MAX} are large enough so that they do not decrease significantly in radius as they fall into the subsaturated layers.

The fact that the model was able to simulate this quasi-steady cloud top condition adds further to the likelihood that, within its limitations, the model is capturing the essential processes occurring in the SCC. Further

corroboration for this is shown in Figure 23. This shows a plot of the saturation ratio as inferred from the temperatures measured within the SCC. Three assumptions were made to obtain these curves: 1) a linear profile of ρ_v was assumed in the clear air above cloud top, 2) the profile of T was that actually measured, and 3) end points of the profile were given by the top B.C. and the saturation vapor density corresponding to the temperature measured in vicinity of the cloud top level.

Since an exact measure of the cloud top in the chamber was not available, three different levels were chosen to represent the cloud top in these calculations. Visual observations in the chamber suggested a cloud top in vicinity of the 3 chosen levels. Interestingly enough, all three curves show substantial supersaturation in the clear air, particularly as cloud top is placed lower in the chamber, i.e., into the colder air (see curve C). Curve B shows the closest correspondence to the SR profile predicted by the model (Curve D), although the magnitude of the supersaturation is higher. Most likely the actual profile of ρ_v tends to have a positive curvature rather than no curvature at all (linear) since vapor is still being lost in layers 1-7 by droplet growth and wall sinks. In that case the magnitude of the SR would be reduced and Curve B would correspond even more closely to the profile obtained with the model.

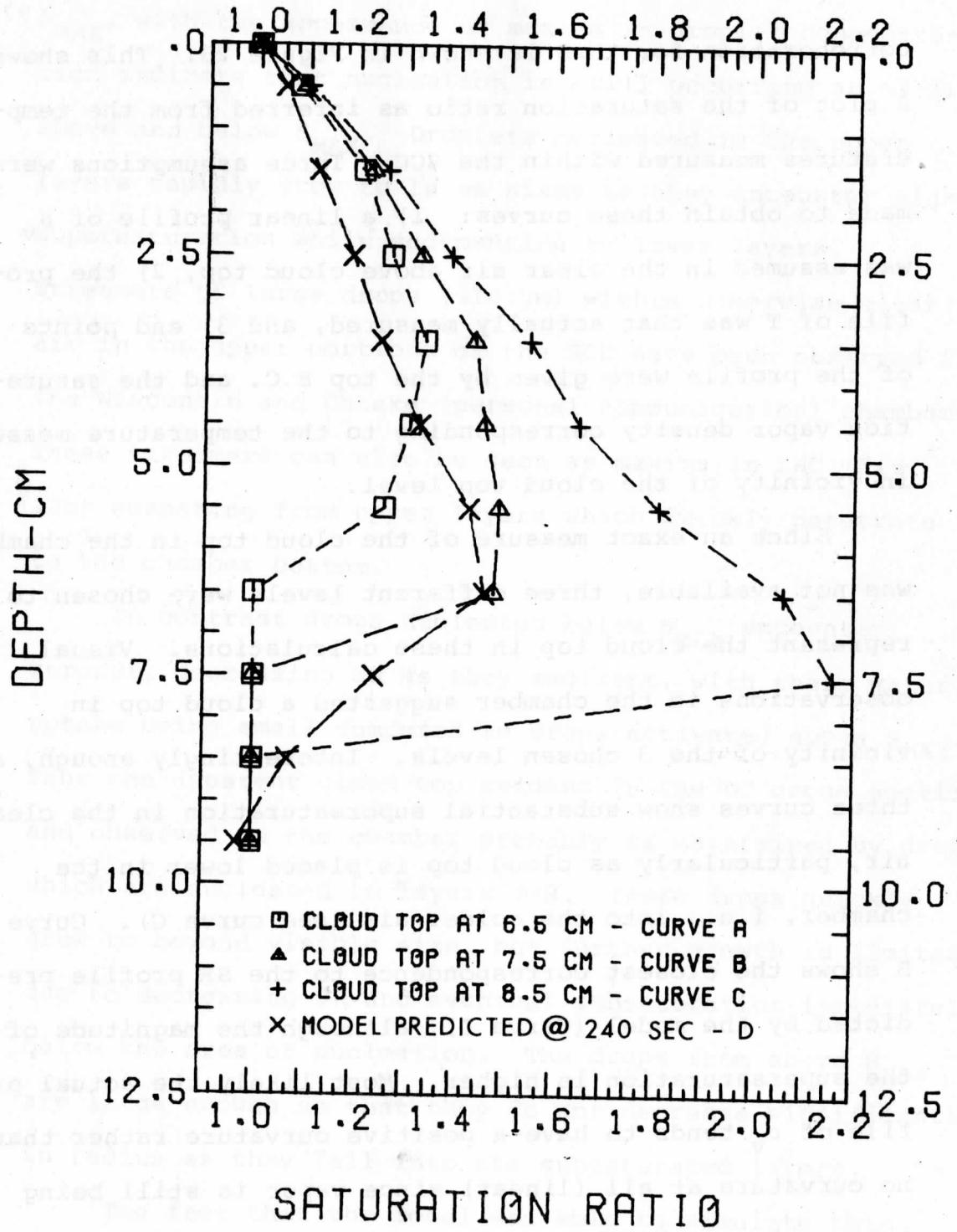


Figure 23. Profile of the saturation ratio inferred from the measured temperature distribution for different cloud top heights. Model predicted profile also included.

V. Implications for Use of SCC as Ice Nucleus Counter

Perhaps of primary interest in the model results are the high values of supersaturation reached in the upper portions of the chamber. As noted by Gagin (1972) and Ohtake (1976) the presence of high supersaturations in the chamber could result in incorrect nucleus counts for the air sample being processed. Condensation followed by freezing (as the resultant drop sediments) may occur on mixed particles which would never be activated in the real atmosphere. At the supersaturations in question even insoluble particles such as AgI may nucleate water drops and thus give erroneous counts as the drops freeze in the colder portions of the chamber.

Ohtake recognized this criticism and formulated an experiment to test its validity. He purged his chamber with the air sample to be tested (containing AgI) and then placed an extension on the normal chamber which he called the second upper chamber. The moisture and heat then diffused downward from the top of the extension and due to the stable temperature profile few of the AgI particles should have been subjected to high supersaturation. Comparison of the counts showed slightly higher values with

the 2nd upper chamber, which is the reverse of what would be expected if the criticism were valid (assuming other factors such as nucleus distribution and resultant drop concentration were equal).

Several implications can be drawn from the experiment:

1) high supersaturations do not occur in the upper portions of the SCC, 2) high supersaturations occur but the S^* for nucleation by the AgI particles in question is even higher, 3) high supersaturation occur in the chamber but condensation-freezing is not an important mode of ice nucleation for AgI at the ambient temperature (-15°C), i.e., contact nucleation dominates. Based on the model results, the likely explanations seem to be 2 or 3.

Fletcher (1959) calculated while Mossop (1968) measured the S^* required for condensation ^{on} of AgI particles of various sizes. Their results, shown in Figure 24 and 25 respectively, indicate that condensation should have occurred on at least a portion of the aerosol particles. Use of the full nucleus distribution in the model could delay the rise in supersaturation but substantial values should still be expected with eventual drop initiation by the AgI. One possible explanation for Ohtake's experimental results is that after condensation on the AgI nuclei subsequent freezing would occur with the nuclei immersed in the drop. Since the threshold temperatures for immersion freezing are probably considerably lower than

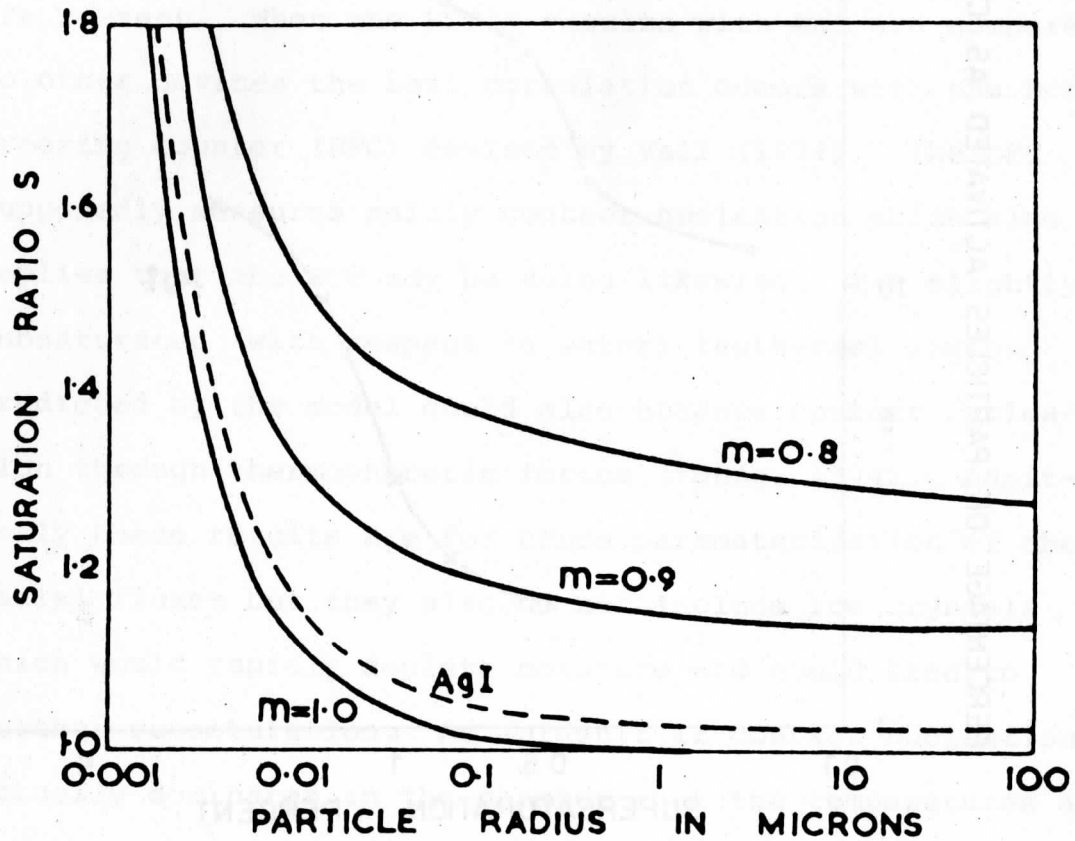


Figure 24. Saturation ratio $S = p/p_{\infty}$ necessary to produce droplets on spherical nuclei of radius R at 0°C . The parameter m is the cosine of the angle of contact of water on the nucleus material. Approximate curve for silver iodide is shown (from Fletcher, 1959).

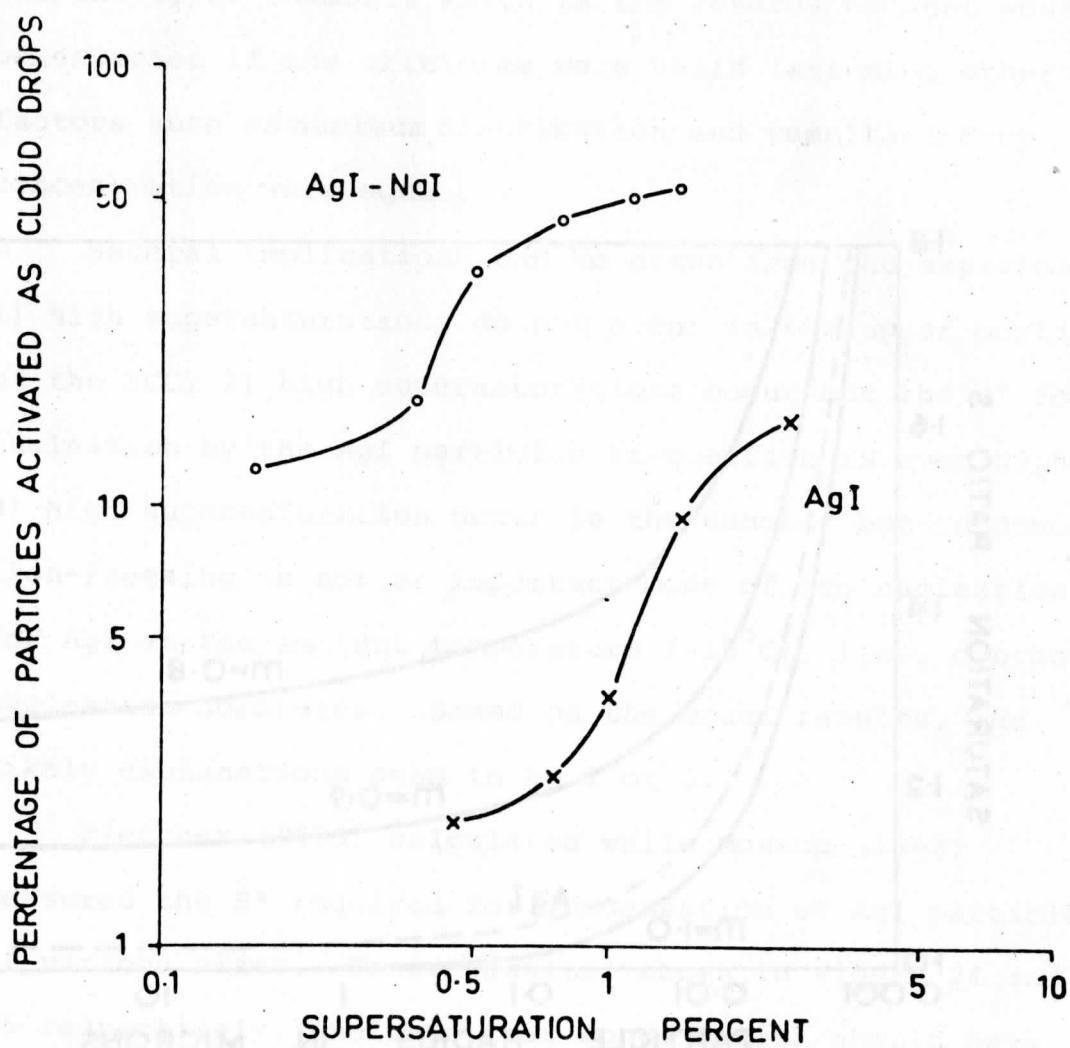


Figure 25. Measured percentage of AgI and AgI-NaI particles which grow into water drops at various supersaturations (from Mossop, 1968).

for contact nucleation (Fletcher, 1970), contact may be the dominant mode of ice nucleation within the relatively warm isothermal region even when high supersaturations are present. When the SCC's results with AgI are compared to other devices the best correlation occurs with the Drop Freezing Counter (DFC) devised by Vali (1974). The DFC supposedly measures mainly contact nucleation which also implies that the SCC may be doing likewise. The slightly subsaturated (with respect to water) isothermal region predicted by the model could also enhance contact nucleation through thermophoretic forces (Young, 1974). Admittedly these results are for crude parameterization of the radial fluxes but they also do not include ice crystals which would rapidly deplete moisture and could lead to further subsaturation. As a result if contact nucleation actually dominates in the chamber - at the temperatures and AgI sizes used - then the results of Ohtake's experiment would make sense and still not conflict with the model results. Nevertheless there is still some question as to whether contact nucleation can be effective within the 2-3 minute time span used by Ohtake for a measurement (Lala, 1976). Additionally the role of deposition or sorption nucleation within the isothermal region (15% supersaturated with respect to ice) must also be considered. The importance of this nucleation mechanism may be a function of droplet concentration as well as degree of supersaturation

(Parungo et al., 1976), e.g., at high droplet concentrations nuclei are more likely to act by contact whereas at lower concentrations deposition may be favored.

Similar arguments to those above can be forwarded to explain the SCC's results with natural nuclei. Ohtake (1976) states that "Measurements of natural ice nuclei made with SCC, MF, DFC and centrifugal deposition techniques finally came into good agreement". Yet if high supersaturations are present in the chamber, the SCC might be expected to give somewhat higher counts if condensation freezing plays an important role. Again, the lower temperature thresholds for immersion freezing may be a particularly relevant factor, especially if condensation occurs on a mixed nuclei which would lower the drop freezing point due to the presence of a dissolved salt (Reischel and Vali, 1975). Other reasons for the "close agreement" may be the relatively small volume within which the high supersaturations occur, the uncertainty of conditions within the other devices and use of nuclei replenishment within the SCC (Ohtake, personal communication) which would keep the supersaturation down.

That contact nucleation is an important mode of action for natural ice nuclei at warm temperatures is still unresolved, however laboratory measurements with relatively large supercooled drops (Gokhale and Goold, 1968; Gokhale and Spengler, 1972) support the existence of

artificial and natural contact nuclei. The possible role of contact nucleation in explaining anomalously high ice crystal concentrations in natural clouds (at -4°C) has been suggested (Young, 1974; Hobbs and Atkinson, 1976) with some agreement between a crude estimate of ice crystal concentrations due to contact nucleation and actual observations. The sudden transformation of a supercooled fog (-10°C) into an ice fog just prior to or during dissipation has also been observed (H. Weickmann personal communication) and suggests that thermophoretic forces may have been active in initiating contact of natural ice nuclei with the fog droplets. In summary, the saturation ratio predicted by the model, while probably somewhat high considering the initial nuclei spectra, i.e., $r_s < 0.01 \mu\text{m}$, nevertheless is not in conflict with the SCC results in measuring natural and artificial ice nuclei, particularly if contact nucleation is a primary mode of ice nucleation in the SCC.

The other parameters shown in Figure 22 suggest that conditions in the isothermal region of the SCC remain relatively uniform for at least 2-3 minutes after cloud initiation. With a dry nuclei input having $r \leq 0.03 \mu\text{m}$ and distributed as shown in Figure 2, the droplet concentration stays at $\sim 2500 \text{ cm}^{-3}$ while liquid water remains between $1-1.5 \text{ gm/m}^3$. Thus the 2-3 minute period used by Ohtake to make a measurement seems reasonable in terms of

cloud uniformity although inclusion of the ice phase may rapidly deplete drops in this region. Beyond 3 minutes the chamber starts drying out as the drops being nucleated and falling into the isothermal region decrease and the vapor sink at the walls dominates. An important point to emphasize is that these results are for the condition of no CN replenishment during the measurement. Ohtake (1976) has found it necessary to add more nuclei when measuring large concentrations of AgI particles since water drops rapidly are lost and must be resupplied. When this procedure is followed the supersaturations produced by the model with the initial conditions as described are most likely too high.

VI. Suggestions for Future Work

The model as formulated has given considerable insight into the conditions and processes occurring within the SCC. Because the physics are fairly straightforward - without the added complication of airflow - the SCC is particularly adaptable to study with a numerical model - a big advantage over other more complicated devices. Several improvements could be incorporated to make the model more accurate, e.g., better parameterization of nucleation, a more quantitative assessment of the difference in results when using vapor density versus vapor pressure and elimination of spurious nucleation caused by redistributing nuclei over an entire bin after initial nucleation.

The next logical step after these changes is to perform extensive sensitivity studies with the model, investigating parameters such as variations in the temperature of the moist top plate, different initial nucleus distributions, different depths of the chamber above the brass cylinder (Ohtake's second upper chamber), etc. and their influence on SR, DC, LWC and the quasi-steady cloud top. In conjunction with these sensitivity studies more

measurements of chamber conditions should be attempted to further confirm the model results, e.g., documentation of the high supersaturations may be possible.

Since the ultimate use of the SCC is as an ice nucleus counter, eventual addition of the ice phase to the model is required. The suggestion made earlier that contact may be the dominant nucleation process in the chamber (within the time period generally used for sample development) could be studied by including a contact nucleation model such as Young (1974) or Alkezweeny (1971). The relationship between mean droplet size and concentration and ice nucleation activity could be investigated by using as input to the chamber (and model) a certain nucleus spectra and comparing model results with observed ice crystals. Further experiments similar to Ohtake's should be performed in conjunction with the model to draw inferences concerning the importance of supersaturations in the chamber top. A more extensive study of ice crystal counts as a function of chamber temperature and supersaturation to ascertain the possible role of immersion freezing at lower temperatures may also be feasible.

In general, the advantage of having some quantitative information on sequence of events and subsequent conditions within a device used for ice nuclei measurements is significant. Introducing the ice phase makes matters somewhat more uncertain again (e.g., what does one use for

ice nucleus concentrations) but the model could be "tuned" through feedback between observations and model results and thereby lead to further knowledge concerning ice nuclei and how they act.

Bibliography

- Alkezweeny, A. J., 1971: A Contact Nucleation Model for Seeded Clouds. *J. Appl. Meteor.*, 10, 732-738.
- Alofs, D. J., and J. C. Carstens, 1976: Numerical Simulation of a Widely Used Cloud Nucleus Counter. *J. Appl. Meteor.*, 15, 350-354.
- Arnason, G., and P. S. Brown, Jr., 1971: Growth of Cloud Droplets by Condensation: A Problem in Computational Stability. *J. Atmos. Sci.*, 28, 72-77.
- Arnason, G., and R. S. Greenfield, 1972: Micro- and Macro-Structures of Numerically Simulated Convective Clouds. *J. Atmos. Sci.*, 29, 342-367.
- Barchet, W. R., 1971: The Interaction between Water Vapor and Pure Silver Iodide in the Vicinity of Saturation. Colorado State University, Atmospheric Science Paper No. 168, 103 pp.
- Barchet, W. R., 1974: A Study of Precipitation Process Modification through Ice Nucleus Deactivation. Final Report NSF Grant ESR72-03349 A02, 51 pp.
- Berry, E. X., 1967: Cloud Droplet Growth by Collection. *J. Atmos. Sci.*, 24, 688-701.
- Berry, E. X., and R. L. Rheinhardt, 1973: Modeling of Condensation and Collection within Clouds. Final Report NSF Grant GA-21350, 96 pp.
- Bigg, E. K., 1971: Report on the Ice Nucleus Workshop, Fort Collins, August 1970. The Second International Workshop on Condensation and Ice Nuclei, L. O. Grant, Ed., 97-105.
- Clark, T. L., 1973: Numerical Modeling of the Dynamics and Microphysics of Warm Cumulus Convection. *J. Atmos. Sci.*, 30, 857-878.

- Cole, J. E., R. A. Dobbins, and H. Semerjian, 1970: Time-Resolved Measurement of Droplet Size and Concentration in Cloud Chambers. *J. Appl. Meteor.*, 9, 684-689.
- Egan, B. A., and J. R. Mahoney, 1972: Numerical Modeling of Advection and Diffusion of Urban Area Source Pollutants. *J. Appl. Meteor.*, 11, 312-322.
- Elliot, W. P., 1971: Dimensions of Thermal Diffusion Chambers. *J. Atmos. Sci.*, 28, 810-811.
- Fitzgerald, J. W., 1970: Non-steady-state Supersaturations in Thermal Diffusion Chambers. *J. Atmos. Sci.*, 27, 70-72.
- Fitzgerald, J. W., 1972: A Study of the Initial Phase of Cloud Droplet Growth by Condensation: Comparison between Theory and Observation. Chicago University Cloud Physics Laboratory, Technical Note, 44. 144 pp.
- Fletcher, N. H., 1959: On Ice-Crystal Production by Aerosol Particles. *J. Meteor.*, 16, 173-180.
- Fletcher, N. H., 1970: On Contact Nucleation. *J. Atmos. Sci.*, 27, 1098-1099.
- Fuchs, N. A., 1959: Evaporation and Droplet Growth in Gaseous Media. New York, Pergamon, 87 pp.
- Gagin, A., 1972: The Effect of Supersaturation on the Ice Crystal Production by Natural Aerosols. *J. Rech. Atmos.*, VI, 175-185.
- Gokhale, N. R., and J. Goold, Jr., 1968: Droplet Freezing by Surface Nucleation. *J. Appl. Meteor.*, 7, 870-874.
- Gokhale, N. R., and J. D. Spengler, 1972: Freezing of Freely Suspended, Supercooled Water Drops by Contact Nucleation. *J. Appl. Meteor.*, 11, 157-160.
- Hobbs, P. V., and D. G. Atkinson, 1976: The Concentrations of Ice Particles in Orographic Clouds and Cyclonic Storms over the Cascade Mountains. *J. Atmos. Sci.*, 33, 1362-1374.
- Howell, W. E., 1949: The Growth of Cloud Droplets in Uniformly Cooled Air. *J. Meteor.*, 6, 134-149.

- Huffman, P. J., 1973: Supersaturation Spectra of AgI and Natural Ice Nuclei. *J. Appl. Meteor.*, 12, 1080-1082.
- Huffman, P. J., and G. Vali, 1973: The Effect of Vapor Depletion on Ice Nucleus Measurements with Membrane Filters. *J. Appl. Meteor.*, 12, 1025-1034.
- Juisto, J. E., and R. L. Lavoie, 1975: AMS Symposium on the Prediction and Measurements of Ice Crystal Concentrations in Clouds, Laramie, Wyoming, June 1975. *Bull. Amer. Meteor. Soc.*, 56, 1175-1179.
- Katz, J. L., and P. Mirabel, 1975: Calculation of Supersaturation Profiles in Thermal Diffusion Cloud Chambers. *J. Atmos. Sci.*, 32, 646-648.
- Koenig, L. R., 1968: Numerical Modeling of Condensation. Final Report Contract No. NSF-C 415, 43 pp.
- Kovetz, A., and B. Olund, 1969: The Effect of Coalescence and Condensation on Rain Formation in a Cloud of Finite Vertical Extent. *J. Atmos. Sci.*, 26, 1060-1065.
- Lala, G. G., and J. E. Juisto, 1972: Numerical Estimates of Humidity in a Membrane-Filter Ice Nucleus Counter. *J. Appl. Meteor.*, 11, 674-683.
- Lala, G. G., 1976: Instrumentation for the Detection of Ice Nuclei. *Atmospheric Technology* #8 - Spring 1976, 50-55.
- Mordy, W., 1959: Computations of the Growth by Condensation of a Population of Cloud Droplets. *Tellus*, 11, 16-43.
- Mossop, S. C., 1968: Silver Iodide as Nucleus for Water Condensation and Crystallization. *J. Rech. Atmos.*, III, 185-190.
- Neiburger, M., and C. W. Chien, 1960: Computations of the Growth of Cloud Drops by Condensation Using an Electronic Digital Computer. *Physics of Precipitation*. Amer. Geophys. Union, Geophysical Monograph #5, H. Weickmann, Ed., 191-210.
- Ogura, Y., and T. Takahashi, 1973: The Development of Warm Rain in a Cumulus Model. *J. Atmos. Sci.* 30, 262-277.

- Ohtake, T., and H. Isaka, 1961: Measurement of Effective Ice Nuclei for Weather Modification, Report on Artificial Stimulation of Rain, 16, 53-78, May 1961, Tohoken Electric Power Company.
- Ohtake, T., 1971: Cloud Settling Chamber for Ice Nuclei Count. The Second International Workshop on Condensation and Ice Nuclei, L. O. Grant, Ed., 58-60.
- Ohtake, T., 1976: Settling Cloud Chamber for Ice Nucleus Counting. The Third International Workshop on Ice Nucleus Measurements, G. Vali, Ed., 151-158.
- Ohtake, T., (personal communication).
- Parungo, P., E. Ackerman, and H. Proulx, 1976: Natural Ice Nuclei. J. Rech. Atmos., X, 45-60.
- Reischel, M. T. and G. Vali, 1975: Freezing Nucleation in Aqueous Electrolytes. Tellus, 27, 414-427.
- Rooth, C., 1960: A Statistical Study of Cloud Droplet Growth by Condensation, Physics of Precipitation. Amer. Geophys. Union, Geophysical Monograph #5, H. Weickmann, Ed., 220-225.
- Ruskin, R. E., and W. C. Kocmond, 1971: Summary of Condensation Nucleus Investigations at the 1970 International Workshop on Condensation and Ice Nuclei. The Second International Workshop on Condensation and Ice Nuclei, L. O. Grant, Ed., 92-96.
- Saxena, V. K., J. N. Burford and J. L. Kassner, Jr., 1970: Operation of a Thermal Diffusion Chamber for Measurements on Cloud Condensation Nuclei. J. Atmos. Sci., 27, 73-80.
- Sinnarwalla, A. M., D. J. Alofs and J. C. Carstens, 1975: Measurement of Growth Rate to Determine Condensation Coefficient of Water Drops Grown on Natural Cloud Nuclei. J. Atmos. Sci., 32, 592-599.
- Squires, P. and S. Twomey, 1961: The Relation between Cloud Drop Numbers and the Spectrum of Cloud Nuclei. Physics of Precipitation. Amer. Geophys. Union. Geophysical Monograph #5, H. Weickmann, Ed., 211-219.
- Squires, P., 1972: Diffusion Chambers for the Measurement of Cloud Nuclei. J. Rech. Atmos., VI, 565-572.



- Takahashi, T., 1976: Warm Rain, Giant Nuclei and Chemical Balance - A Numerical Model. *J. Atmos. Sci.*, 33, 269-286.
- Twomey, S., 1959a: The Nuclei of Natural Cloud Formation. Part I: The Chemical Diffusion Method and its Application to Atmospheric Nuclei. *Geofis. Pura. Appl.*, 43, 227-242.
- Twomey, S., 1963: Measurements of Natural Cloud Nuclei. *J. Rech. Atmos.*, I, 101-105.
- Vali, G., 1974: Contact Ice Nucleation by Natural and Artificial Aerosols. In Preprint Vol., Conference on Cloud Physics, 21-25 October, Tucson, Ariz., American Meteorological Society, Boston, Mass., 34-37.
- Vali, G., 1975: Ice Nucleation Workshop, 1975, Laramie, Wyoming, May-June 1975. *Bull. Amer. Meteor. Soc.*, 56, 1180-1184.
- Weickmann, K. M., and W. R. Barchet, 1976: Supersaturation Regime within a Settling Cloud Chamber: Preliminary Results. Preprint International Conference on Cloud Physics, July 26-30, Boulder, Colo., American Meteorological Society, Boston, Mass., 602-606.
- Weickmann, H. K., (personal communication).
- Wieland, W., 1956: Die Wasserdampfkondensation an Natürlichen Aerosol bei geringen Übersättigungen. *Z. Angew. Math. Phys.*, 7, 428-460.
- Winkler, P., and C. Junge, 1972: The growth of Atmospheric Aerosol Particles as a Function of Relative Humidity - Part I: Method and Measurements at Different Locations. *J. Rech. Atmos*, VI, 617-638.
- Young, K. C., 1974: The role of contact nucleation in ice phase initiation. *J. Atmos. Sci.*, 31, 768-776.
- Young, K. C., 1974: A Numerical Simulation of Wintertime, Orographic Precipitation: Part I. Description of Model Microphysics and Numerical Techniques. *J. Atmos. Sci.*, 31, 1735-1748.